Simulation of Vapour-Liquid Condensation in Dipolar Fluids and Uniform Sampling Monte Carlo Algorithms

Georg Clemens Ganzenmüller

Doctor of Philosophy

The University of Edinburgh

2009

"All good computer simulations only take 10 minutes."

Abstract

This works examines the question whether a vapour-liquid phase transition exists in systems of particles with purely dipolar interactions, a topic which has been the subject of a longstanding debate. Monte Carlo simulation results for two *modi operandi* to tackle this issue are presented. One approach examines the phase behaviour of fluids of charged hard dumbbells (CHD), each made up of two oppositely charged hard spheres with diameters σ and separation d. In the limit $d/\sigma \to 0$, and with the temperature scaled accordingly, the system corresponds to dipolar hard spheres (DHS) while for larger values of d ionic interactions are dominant. The crossover between ionic and dipolar regimes is examined and a linear variation of the critical temperature T_c^* in dipolar reduced units as a function of d is observed, giving rise to an extrapolated $T_{c,DHS}^* \approx 0.15$. The second approach focuses on the dipolar Yukawa hard sphere (DYHS) fluid, which is given by a dipolar hard sphere and an attractive isotropic interaction ϵ_Y of the Yukawa tail form. In this case, the DHS limit is obtained for $\epsilon_Y \to 0$. It is found that T_c^* depends linearly on the isotropic interaction strength ϵ_Y over a wide range, coinciding with the results for the CHD model and extrapolating to a similar value of $T_{c,DHS}^*$. However, with the use of specially adapted biased Monte Carlo techniques which are highly efficient, it is shown that the linear variation of T_c^* is violated for very small values of the Yukawa interaction strength, almost two orders of magnitude smaller than the characteristic dipolar interaction energy. It is found that phase separation is not observable beyond a critical value of the Yukawa energy parameter, even though in thermodynamic and structural terms, the DYHS and DHS systems are very similar. It is suggested that either some very subtle physics distinguishes the DYHS and DHS systems, or the observation of a phase transition in DHSs is precluded by finite-size effects. In the context of phase separation in highly correlated fluids, new flat-histogram Monte Carlo simulation techniques based on the Wang-Landau algorithm are evaluated and shown to be useful tools. This work presents a general and unifying framework for deriving Monte Carlo acceptance rules which facilitate flat histogram sampling. The framework yields uniform sampling rules for thermodynamic states given either by the mechanically extensive variables appearing in the Hamiltonian or, equivalently, uniformly sample the thermodynamic fields which are conjugate to these mechanical variables.

Declaration of Authorship

I hereby declare that this thesis is of my own composition, and that it contains no material previously submitted for the award of other degrees. The work reported in this thesis has been executed by myself, except where due acknowledgement is made in the text.

Georg Clemens Ganzenmüller

Acknowledgements

It is a pleasure to thank my supervisor, Dr Philip J. Camp, for making available his support continously and in a number of ways. It is a great honor for me to know him and working with him could not have been a better experience. For financial support, I gratefully acknowledge the the UK Engineering and Physical Sciences Research Council.

Contents

Für meine Eltern,

Barbara and Klaus Ganzenmüller,
die mich immer unterstützt haben.

Outline

The aim of this thesis is to shed light on the question of whether a vapour-liquid phase transition exists in systems of particles with purely dipolar interactions, a topic which has been the subject of a longstanding debate [1–5]. Dipolar fluids have numerous scientific and industrial applications, mostly related to the strong field-responsive properties of colloidal ferrofluids [6] or electrorheological fluids [7]. For these applications, it is crucial to know whether the system exists in a single homogeneous phase. Dipolar fluids also have theoretical significance as a fundamental model of statistical mechanics; they are perhaps the simplest example of an anisotropic fluid, which may provide physical insight into polar fluids such as hydrogen fluoride or even water [8]. In order to investigate these questions, use is made of computer simulations using the Monte Carlo method. The organisation of this work is as follows:

- In the Introduction, the theoretical challenges associated with the subtle physics of the underlying mechanism which drives phase separation in such fluids are examined and the Monte Carlo method is briefly described.
- Part I is devoted to a detailed discussion of Monte Carlo simulation techniques in the context of phase separation, with particular attention to flat-histogram sampling algorithms which can overcome some of the problems from which normal Monte Carlo methods suffer. These methods are illustrated and validated using a variety of both continuous and lattice models featuring first-order phase transitions.
- In Part II, phase separation of dipolar particles is investigated. Two models of particular relevance to this topic are studied. Firstly, the phase behaviour of fluids of charged hard dumbbells (CHD), each made up of two oppositely charged hard spheres with diameters σ and separation d. In the limit $d/\sigma \to 0$, and with the temperature scaled accordingly, the system corresponds to dipolar hard spheres (DHS) while for larger values of d ionic interactions are dominant. This model thus facilitates the crossover from the ionic regime where phase separation is known to occur to the dipolar regime where the answer to this question is unclear.

The second approach focuses on the dipolar Yukawa hard sphere (DYHS) fluid, in which the particles are given by dipolar hard spheres with attractive isotropic interactions of the Yukawa form and strength ϵ_Y. In this case, the DHS limit is obtained for $\epsilon_Y \to 0$. By starting from a high value of ϵ_Y where phase separation is driven by the isotropic interaction and then reducing ϵ_Y, this model also allows to track the critical parameters as dipolar interactions become important.

Chapter 1

Introduction

1.1 Vapour-liquid phase separation

Condensation of a simple fluid from a dilute gas to a dense liquid is well understood since van der Waals' (vdW) seminal work [9] well over a century ago. He realised that a qualitative description of phase separation could be obtained by modifying the ideal-gas equation of state, $pV = Nk_BT$, which links pressure p and volume V to the number of particles N and temperature T using Boltzmann's constant k_B. His modification was to account for a reduced pressure $p_{\text{eff}} = p - \Delta p$ which is due to the presence of attractive intermolecular forces, and, a reduced effective volume $V_{\text{eff}} = V - bN$ where b is the excluded volume, i.e. that region of space which two particles cannot simultaneously occupy due to their repulsive character at short distances. The famous vdW equation of state (EOS) thus reads

$$p + \frac{a}{v} = \frac{k_BT}{v - b} \tag{1.1}$$

where the parameter a describes the attractive intermolecular forces and v is the volume per particle. This picture, entirely motivated by physical insight, is intrinsically a *mean field* description of the microscopic particle-particle correlations as it incorporates only an approximate description of the inter-particle forces. A complete microscopic description would, for example, predict an enhanced probability of finding two particles as close together as possible without overlapping, due to the hard core repulsion and short-ranged attraction. However, such detailed correlations are completely absent in the vdW EOS. Yet, phase separation emerges naturally as a violation of the thermodynamically required inequality $\frac{\partial p}{\partial v} \leq 0$ which implies that the free energy as a function of density is not a convex function. Whenever convexity is violated, the system can attain a lower free energy by separating into two phases, see Fig. 1.1. vdW theory predicts that the shape of the coexistence envelope close to the critical point (located at a critical

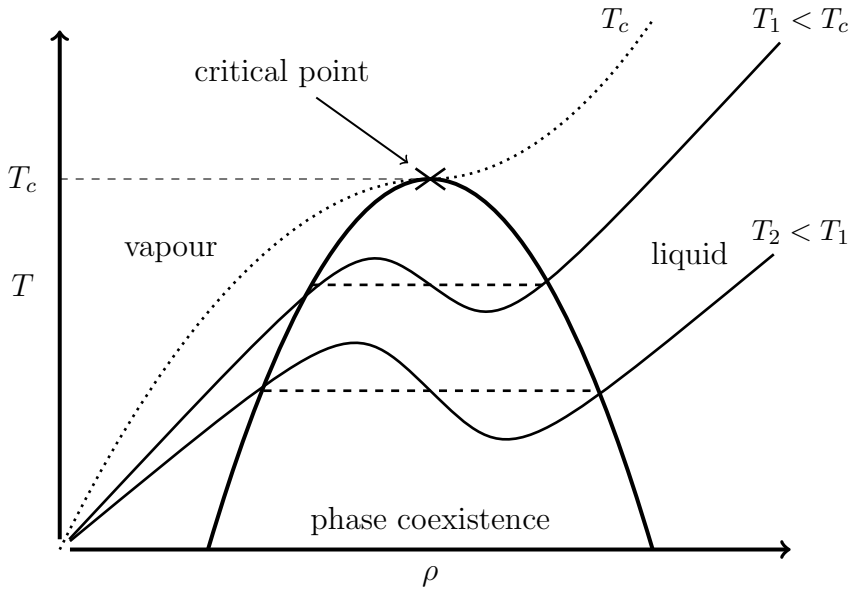

Figure 1.1: Projection of Van der Waals isotherms onto the liquid-vapour coexistence envelope in the number density–temperature plane. Below the critical temperature T_c, the vdW isotherms loop around a point of inflection, violating the thermodynamic requirement $\frac{\partial p}{\partial \rho} \geq 0$. The occurrence of these loops is associated with phase separation into a dilute vapour and a dense liquid.

temperature T_c and critical density ρ_c) follows a power law: coexisting vapour ($-$) and liquid ($+$) densities scale like $\rho_\pm = \rho_c \pm a|t|^\beta$, where $t = (T - T_c)/T$ and $\beta = 1/2$. Such a scaling behaviour with this specific value of β is a generic feature shared by all mean-field theories. At low densities, low free energy is realised via high translational entropy while the dense liquid phase is stabilised by attractive forces. But why is it not possible to go continuously from low to high densities? It is the presence of a mechanical instability at intermediate densities, caused by the competition between the excluded volume effects and the attractive intermolecular forces which drives abrupt phase separation in this model. In general, this mechanism is associated with a high critical temperature comparable to the well-depth of the interaction potential (expressed in units of $k_B T$) in order to sufficiently stabilise the entropic contribution to the free energy of the dilute phase.

As the vdW model employs only a mean-field picture of the physical interactions, it is obvious that vapour-liquid phase separation can be phenomenologically described without referring to the correlations between the particles. But what happens if these correlations are taken into account? The answer to this question is in general very difficult to obtain, as a closed form expression for the free energy of a correlated system involves solving an interacting many-body problem. However, in a mathematical *tour de force*, Onsager succeeded in doing so for the Ising model in two dimensions, a model system for magnetic short-range interactions [10] which can also be mapped on to the problem

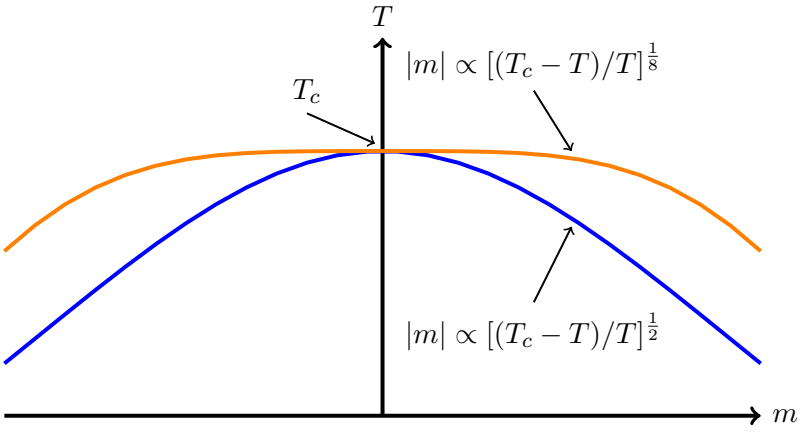

Figure 1.2: Order-disorder transition in the two-dimensional Ising model: Above the critical temperature T_c, the system is in a completely disordered paramagnetic state with zero magnetisation m. At T_c phase separation into an ordered phase with finite magnetisation $|m| > 0$ and a disordered phase occurs with the value of m governed by a power law. Mean-field descriptions of this phenomenon yield an exponent $\beta = 1/2$ while the exact value for the Ising model in two dimensions is $\beta = 1/8$.

of vapour-liquid phase separation[1]. It turned out that his exact solution resulted in different behaviour near the critical point to what mean-field theory predicted. Specifically, the exponents of the power laws which describe the scaling behaviour of various macroscopic observables such as the susceptibility, or the increase of magnetisation below the critical temperature, were found to deviate from their corresponding mean-field values. Fig.1.2 compares Onsager's solution to the scaling behaviour of the magnetisation with the prediction made by mean-field theory. Using renormalisation group theory [11, 12], the difference between mean-field and exact behaviour could be traced back to density fluctuations which become important at the critical point. Indeed, the correlation length, which characterises the spatial extent of density fluctuations, diverges at the critical point, a fact completely absent in mean-field theory. Experimental evidence for the diverging correlation length is given by the phenomenon of *critical opalescence*, where an otherwise clear and transparent fluid becomes opaque at the critical point. The physical reason for this is the formation of fluctuating vapour and liquid domains covering all lengthscales, including the wavelength of visible light, causing scattering. Phase diagrams of simple liquids which show this phenomenon are reported in Chapter 4.

[1]This is the so-called lattice-gas model in which lattice sites are either fully occupied or not. In this model, phase coexistence emerges between low and high occupation fractions of the lattice, corresponding to the vapour and liquid phases of a real fluid.

1.1.1 Vapour-liquid condensation in highly correlated fluids

It is remarkable that the critical behaviour of all physical models interacting via short-ranged forces can be described by a universal set of exponents [2], depending only on the number of dimensions. Owing to its historical importance, this set is usually referred to as the *Ising universality class*. It is even more surprising that systems of charged particles interacting via long-range coulombic forces (such as the model of charged soft spheres, for which the phase diagram is reported in Chapter 4) have also been shown to belong to this universality class [13]. This can only be understood if one considers the effective interaction potential which suffers from electrostatic screening due to charge ordering, attenuating the interaction exponentially over distance. However, the mechanism by which phase transition is driven in a coulombic fluid is very different from a vdW fluid. In the latter case, it is the competition between hard-core repulsion and attractive interaction which leads to a mechanical instability. Because both effects become important only at high concentrations, the critical density of a simple fluid is relatively high. In contrast, coulombic fluids have a much lower critical density such that the effects of hard-core repulsion cannot be important. Additionally, due to the isotropic distribution of charges, the mean electrostatic potential is zero throughout space, implying that the vdW mean-field pressure correction to the ideal-gas equation of state is zero [14]. The fact that systems of charged hard particles do have a vapour-liquid phase transition must be attributed to details completely absent at the vdW mean-field level and therefore be related to strong correlation effects. Correlation becomes important only at low temperatures which rationalises the unusually low critical temperature of coulombic fluids.

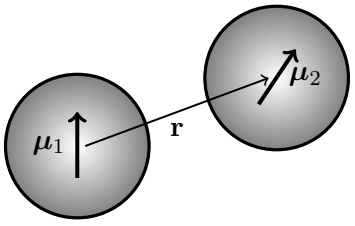

Figure 1.3: Dipolar hard spheres: Spheres of diameter σ with a point dipole at the centre. The interaction potential $u_{DHS}(\mathbf{r}, \boldsymbol{\mu}_1, \boldsymbol{\mu}_2)$ is $+\infty$ for $|\boldsymbol{r}| < \sigma$ and $\frac{\boldsymbol{\mu}_1 \cdot \boldsymbol{\mu}_2}{r^3} - \frac{3(\boldsymbol{\mu}_1 \cdot \mathbf{r})(\boldsymbol{\mu}_2 \cdot \mathbf{r})}{r^5}$ otherwise.

[2] This is strictly only true in the absence of particular symmetries. Depending on the dimensionality of space and the order parameter, different sets of exponents are obtained.

1.1.2 Vapour-liquid condensation caused by dipolar forces?

Particles interacting via dipolar forces represent another class of strongly correlated fluids. The simplest model for such a fluid is one comprised of dipolar hard spheres (DHS), each possessing a spherical hard core with a point dipole at its centre (see Fig. 1.3). In 1970, de Gennes and Pincus argued that, because the Boltzmann-weighted, angle average of the dipole-dipole potential has a leading order, attractive contribution proportional to $-r^{-6}$, "on the whole, we expect in 0 field a mechanical phase diagram somewhat similar to that of a conventional Van der Waals [sic] fluid, with a gas phase, a liquid phase and a solid phase." However, up to date no experimental results, *in silico* or otherwise, are available which have proved the existence of vapour-liquid phase separation in DHSs. It is obvious that, as in the case of charged hard spheres, the vdW mean-field pressure correction is again zero as the average electric field within an isotropic phase of a dipolar fluid vanishes. The hard core/low enthalpy competition picture which gives rise to high temperature phase separation thus cannot apply but we might expect a correlation-driven mechanism to occur at low temperatures. It is precisely the low temperatures at which phase separation is expected that makes theoretical treatment of DHSs so difficult. At low temperatures, DHS align in strong spaghetti-like chains, being highly correlated over many particle diameters both with respect to their orientation and position (see Fig. 1.4). Additionally, the absence of electrostatic screening for point dipoles means no damping of the long-ranged dipolar interactions, which implies that the hypothetical phase transition of DHS must belong to a different universality class different from the Ising model [15]. In 2000, Tlusty and Safran presented a mechanism which accommodates phase separation in strongly clustered dipolar fluids [8]; in essence, the transition is driven by the free energies of defects, these being particles at the ends of chains ('end' defects) and particles having three nearest neighbours ('Y' defects). In their picture, the phase separation occurs as a demixing transition of the different defect types. Fig. 1.5 illustrates these defect types.

Capturing these effects is difficult at any level of liquid state theory, and so the problem calls for computer simulations. Part II of this work presents an attempt to unravel the mystery whether or not there exists vapour-liquid phase separation in DHSs using state-of-the-art Monte Carlo simulation methods. The other focal point of this thesis, Part I, lies in devising new Monte Carlo simulation methods which are tested on both simple and complicated models of fluids, and are ultimately applied to DHSs.

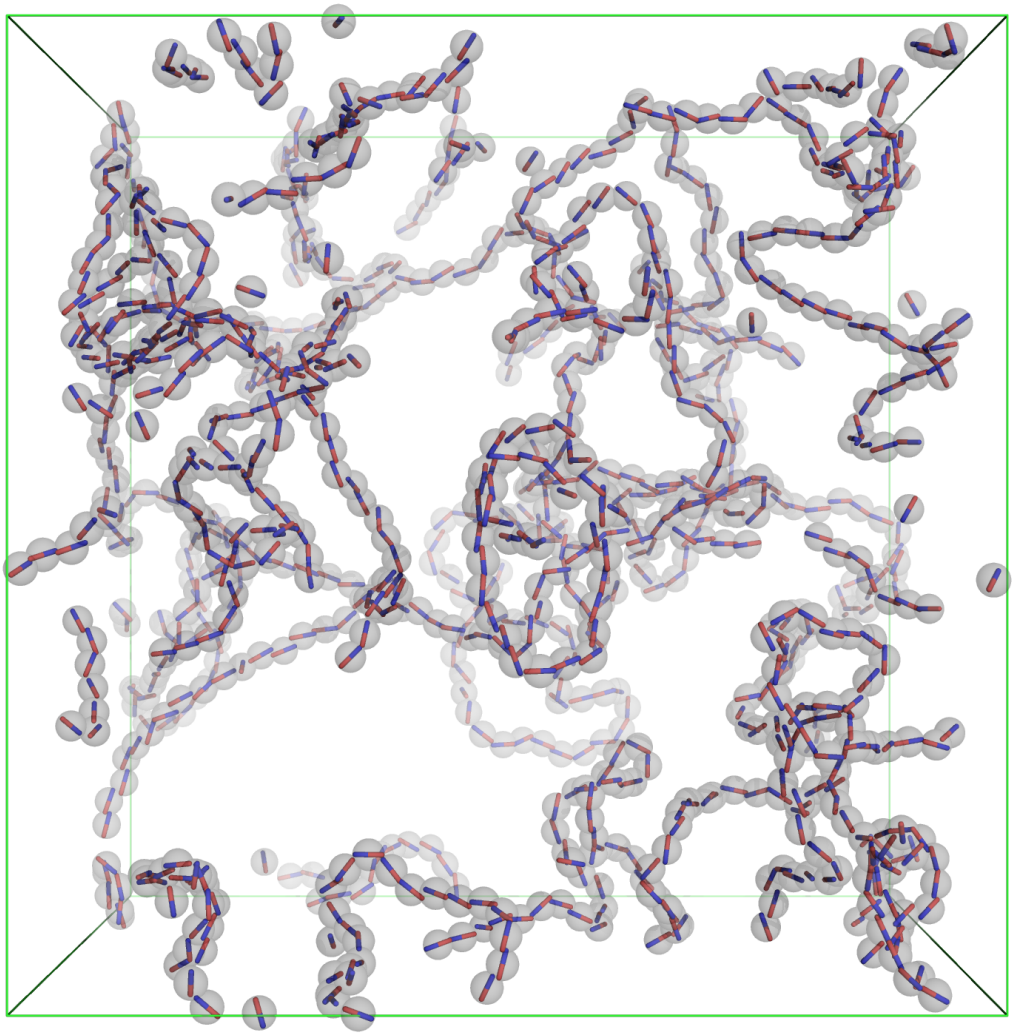

Figure 1.4: Example configuration of DHS at $T^* = 0.15$, $\rho^* = 0.025$ (dipolar reduced units, see text for definition).

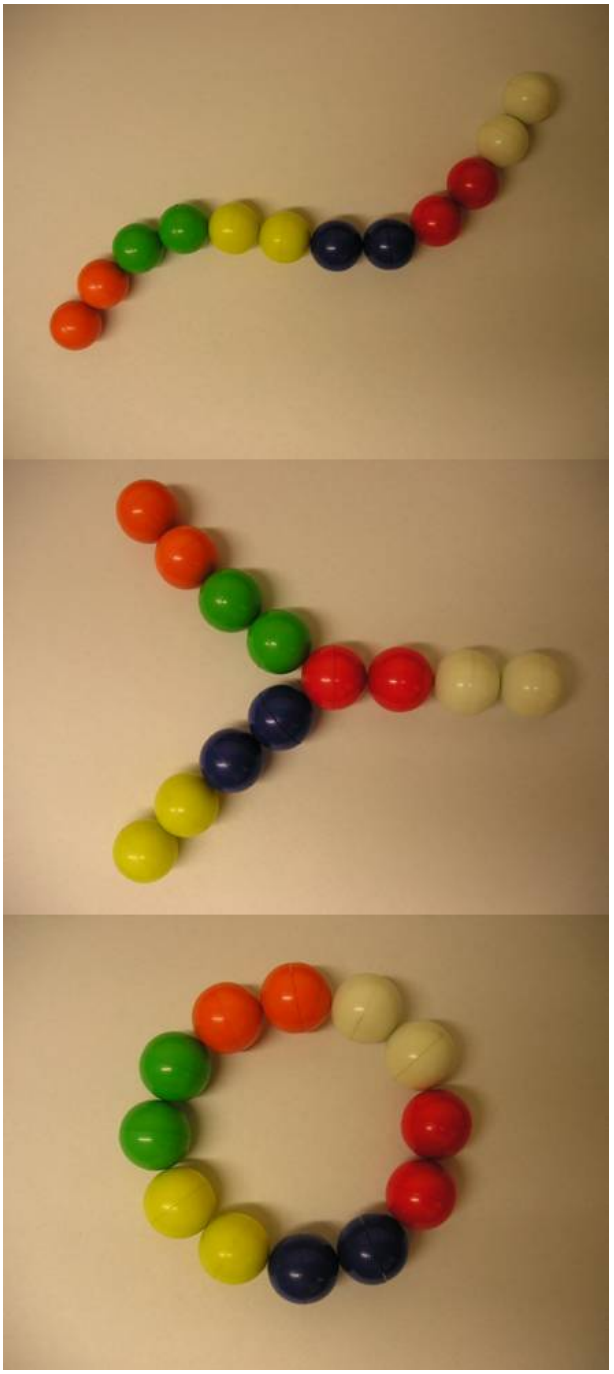

Figure 1.5: Illustration of defect types and ground state in strongly dipolar fluids. (top) free chain ends with high translational entropy, (middle) branching point with configurational entropy, energetic ground state (bottom)

1.2 Computer simulations of many-body systems

It is a most challenging mathematical task to study directly the behaviour of three interacting particles and no analytical closed-form solutions exist for four or more particles. Statistical mechanics significantly simplifies this problem because, rather than focussing on the complete behaviour of a particular particle, the average behaviour of a large collection of interacting particles is studied. Still, even the stochastic analysis of statistical expectation values is a daunting task as averages, e.g. those computed in the canonical ensemble at fixed temperature T, volume V, and number of identical particles N take on the following form:

$$\langle A \rangle = \frac{\int\limits_{(\hat{\mathcal{P}},\hat{\mathcal{Q}})} A(\boldsymbol{p}^N, \boldsymbol{q}^N) \exp\left[-\beta \mathcal{H}(\boldsymbol{p}^N, \boldsymbol{q}^N)\right] \mathrm{d}\boldsymbol{p}^N \mathrm{d}\boldsymbol{q}^N}{\int\limits_{(\hat{\mathcal{P}},\hat{\mathcal{Q}})} \exp\left[-\beta \mathcal{H}(\boldsymbol{p}^N, \boldsymbol{q}^N)\right] \mathrm{d}\boldsymbol{p}^N \mathrm{d}\boldsymbol{q}^N} \tag{1.2}$$

The integration domain $(\hat{\mathcal{P}}, \hat{\mathcal{Q}})$ is the quantum-mechanical phase space of all allowable combinations of momenta $\boldsymbol{p}$ and positions $\boldsymbol{q}$ of all N particles; instantaneous values of $A(\boldsymbol{p}^N, \boldsymbol{q}^N)$ are weighted by their corresponding Boltzmann factor $\exp\left[-\beta \mathcal{H}(\boldsymbol{p}^N, \boldsymbol{q}^N)\right]$ where $\beta = 1/k_B T$ and $\mathcal{H}(\boldsymbol{p}^N, \boldsymbol{q}^N)$ is the Hamiltonian of the system. If quantum-mechanical effects are neglected, a classical expectation value can be formed by absorbing the quantum degrees of freedom into an effective constant h^{DN}, where D is the dimensionality of the system, and accounting for the indistinguishability of identical particles with a factor of $N!$:

$$\langle A \rangle = \frac{\frac{1}{h^{DN} N!} \int\limits_{(\mathcal{P},\mathcal{Q})} A(\boldsymbol{p}^N, \boldsymbol{q}^N) \exp\left[-\beta \mathcal{H}(\boldsymbol{p}^N, \boldsymbol{q}^N)\right] \mathrm{d}\boldsymbol{p}^N \mathrm{d}\boldsymbol{q}^N}{\frac{1}{h^{DN} N!} \int\limits_{(\mathcal{P},\mathcal{Q})} \exp\left[-\beta \mathcal{H}(\boldsymbol{p}^N, \boldsymbol{q}^N)\right] \mathrm{d}\boldsymbol{p}^N \mathrm{d}\boldsymbol{q}^N} \tag{1.3}$$

The integration domain $(\mathcal{P}, \mathcal{Q})$ now only includes classical values for momenta and positions. The Hamiltonian can then be written as a sum of potential energy E and kinetic energy K,

$$\mathcal{H}(\boldsymbol{p}^N, \boldsymbol{q}^N) = E(\boldsymbol{q}^N) + \sum_{i=1}^{N} \frac{|\boldsymbol{p}_i|^2}{2m} \tag{1.4}$$

where m is the mass of a particle. The simultaneous dependence of $\mathcal{H}$ on all positions and momenta is precisely what confounds exact analytical solutions as it prohibits factorisation of the integral. However, in the case of time-independent properties $A(\boldsymbol{q}^N)$,

the integration domain can be significantly reduced within the so-called *classical approximation* [16], by integrating out the kinetic energy dependence analytically:

$$\frac{1}{h^{DN}} \int_{\mathcal{P}} \exp\left(-\beta \sum_{i=1}^{N} \frac{|\boldsymbol{p}_i|^2}{2m}\right) \mathrm{d}\boldsymbol{p}^N = \left(\frac{2\pi m}{\beta h^2}\right)^{ND/2} \tag{1.5}$$

It is common practice to absorb the right-hand side of the above equation into the so-called thermal de Broglie wavelength, $\lambda = \sqrt{\beta h^2 / 2\pi m}$. The classical expectation value thus takes on the following form:

$$\langle A \rangle = \frac{\frac{1}{\lambda^{DN} N!} \int A(\boldsymbol{q}^N) \exp\left[-\beta E(\boldsymbol{q}^N)\right] \mathrm{d}\boldsymbol{q}^N}{\frac{1}{\lambda^{DN} N!} \int \exp\left[-\beta E(\boldsymbol{q}^N)\right] \mathrm{d}\boldsymbol{q}^N} \tag{1.6}$$

The above equation makes it clear that classical, time-independent averages do not depend on a specific value of the quantum-mechanical fudge factor h as the Broglie wavelength vanishes by cancellation. In the following, the convention $\lambda = 1$ is therefore adopted. Still, even this simplified problem is not analytically tractable and quasi-exact numerical integration methods (e.g. Gaussian quadrature) also fail to work due to the high dimensionality of the integration domain: for a small system of only 10 particles in $D = 3$ spatial dimensions, the integrand already lives in 30 dimensions, rendering the numerical summation over a grid impossible.

The denominator appearing in the above equation is the partition function of the system and acts as a normalisation constant. In the context of a computer experiment where particles are usually confined to a cubic simulation volume V of lateral length L, it is convenient to define the partition function of a system of N identical particles in D dimensions as follows, making use of a set of scaled coordinates $\boldsymbol{r} = \boldsymbol{q}/L$:

$$\begin{aligned} Q(N,V,T) &= \frac{1}{\lambda^{DN} N!} \int \exp\left[-\beta E(\boldsymbol{q}^N)\right] \mathrm{d}\boldsymbol{q}^N \\ &= \frac{V^N}{\lambda^{DN} N!} \int \exp\left[-\beta E(\boldsymbol{r}^N; L)\right] \mathrm{d}\boldsymbol{r}^N \\ &= \frac{V^N}{\lambda^{DN} N!} \int \exp\left[-\beta E(\boldsymbol{\Gamma})\right] \mathrm{d}\boldsymbol{\Gamma} \end{aligned} \tag{1.7}$$

In the last line the short-hand notation $\boldsymbol{\Gamma} = \boldsymbol{r}^N$ is introduced and it is understood that the configurational energy E is evaluated using the original, unscaled set of coordinates. The above form allows the partition function to be decomposed into an ideal-gas contribution, $Q_{\mathrm{id}}(N,V)$ and a non-ideal term arising from the particle interactions,

$Q_{\mathrm{conf}}(N,V,T)$:

$$\begin{aligned} Q(N,V,T) &= \frac{V^N}{\lambda^{DN}N!} \times \int \exp\left[-\beta E(\mathbf{\Gamma})\right] \mathrm{d}\mathbf{\Gamma} \\ &= Q_{\mathrm{id}} \times Q_{\mathrm{conf}} \end{aligned} \tag{1.8}$$

It is only stochastic sampling methods which can save us from a life dominated by the approximations required to make a mathematical treatment of averages like Eq. (1.3) possible. This is due to the fortunate fact that only a vanishingly small proportion of phase space contributes significantly, so that only these configurations need to be sampled in order to estimate averages with sufficient accuracy. The methods which sample only important regions of phase space can be broadly divided into two classes:

1. *Importance sampling Monte Carlo* – This method generates individual phase space configurations with a probability proportional to the Boltzmann weight. Only average static properties can be probed as time does not occur as a natural variable. These properties are directly obtained by simple averaging over the generated configurations as they are sampled according to the correct probability distribution.

2. *Molecular Dynamics* – The dynamical behaviour of the model system under study is discretised into finite time steps thus allowing a numerical integration of the equations of motion to propagate the system forward in time. This method traverses phase space with an average sampling frequency exactly proportional to the Boltzmann weight, however as simulation time is always finite in practice, it remains a stochastic sampling method.

If dynamical behaviour is of interest, one necessarily has to use the Molecular Dynamics method. However, if only thermodynamic properties like the phase diagram of a system are required, the choice is between both methods and one has to consider potential advantages and disadvantages associated with each method. This work deals only with phase separation and it is here where the alleged disadvantage of Monte Carlo, namely the absence of dynamical information, can be turned into a powerful tool, as it permits faster changes from one sampled configuration to another than what is thermally realisable on the physical timescale of the system. Therefore, only Monte Carlo sampling has been used for the simulations described here.

1.2.1 The importance sampling Monte Carlo method

The problem at hand is to compute an average in phase space according to the Boltzmann probability distribution,

$$P(\mathbf{\Gamma}) = \frac{Q_{\mathrm{id}}(N,V)\exp\left[-\beta E(\mathbf{\Gamma})\right]}{Q(N,V,T)} \tag{1.9}$$

Via a transformation of the integration variable as shown in Appendix A, it is possible to recast the computation of the average into a simple arithmetic mean,

$$\langle A\rangle \approx \frac{1}{K}\sum_{i=1}^{K} A(\mathbf{\Gamma}_i) \tag{1.10}$$

if only K discrete samples $\mathbf{\Gamma}_i$ are drawn from the probability distribution Eq. (1.9). The problem therefore is transferred to the generation of samples according to $P(\mathbf{\Gamma})$, which is not trivial as a direct transformation necessitates the partition function which is so difficult to compute due to its high dimensionality. This is where the celebrated solution of Metropolis *et al.* [17] comes into play as it allows for sampling $\mathbf{\Gamma}$ according to $P(\mathbf{\Gamma})$ without requiring the normalisation of $P(\mathbf{\Gamma})$.

The idea behind Metropolis' sampling algorithm is that, starting from an arbitrary sample point in phase space, new sampling points are generated which ultimately converge towards the limiting distribution $P(\mathbf{\Gamma})$. Central to this idea is an expression for how the

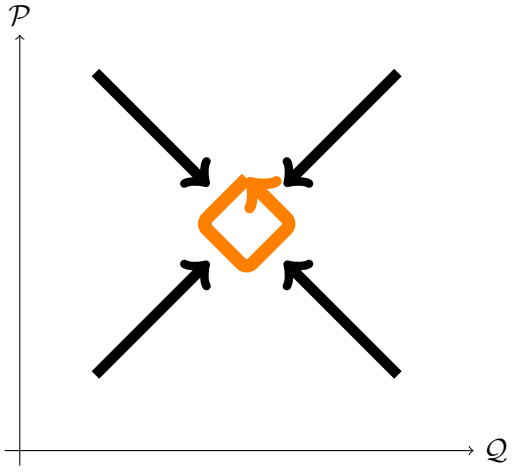

Figure 1.6: Visualisation of the Metropolis algorithm. Starting from arbitrary initial conditions, samples in phase space are successively generated such that regions of high Boltzmann probability are reached.

system is propagated through phase space,

$$\boldsymbol{q}(t+1) = \boldsymbol{q}(t)\underline{\mathbf{\Pi}} \tag{1.11}$$

where the *transition matrix* $\underline{\mathbf{\Pi}}$ is a square matrix operating to the left on the probability vector $\boldsymbol{q}(t)$ whose elements $q_n(t)$ describe the probability for the system of being in state n at step t. Because the propagation to the next state only requires information about the current state, this constitutes a *Markov Chain*. The required convergence towards the limiting distribution $\boldsymbol{P}$, now expressed as a vector with elements drawn from the distribution $P(\mathbf{\Gamma})$, is stated by:

$$\boldsymbol{q}(t) = \boldsymbol{q}(0)\overbrace{\underline{\mathbf{\Pi}}\ldots\underline{\mathbf{\Pi}}}^{t\ times} \tag{1.12}$$

$$\boldsymbol{P} = \lim_{t\to\infty} \mathbf{q}(0)\underline{\mathbf{\Pi}}^{(t)} \tag{1.13}$$

Once the algorithm is converged, the *steady state* condition is reached

$$\boldsymbol{P} = \boldsymbol{P}\underline{\mathbf{\Pi}} \tag{1.14}$$

which is an eigenvalue equation with eigenvalue one. This property translates into a sum rule for the matrix rows,

$$\sum_n \Pi_{on} = 1 \tag{1.15}$$

which can be understood in physical terms as conservation of probability. Note now that the elements of $\underline{\mathbf{\Pi}}$ are labelled '*on*', describing the transition probability from old state o to new state n. Decomposing the matrix product Eq. (1.14) into sums for each row, the following equation is obtained

$$P_n = \sum_o P_o \Pi_{on} \tag{1.16}$$

which is generally impossible to solve for $\underline{\mathbf{\Pi}}$. However, Metropolis introduced the *detailed balance condition* to significantly restrict solution space,

$$P_o \Pi_{on} = P_n \Pi_{no} \tag{1.17}$$

and gave one possible solution[3] as:

$$\Pi_{on} = \min\left[1, \frac{P_n}{P_o}\right] \tag{1.18}$$

The correctness of the Metropolis solution is verified by substituting it into Eq. (1.15). Using the above results, the acceptance probability of moving from an old state in phase space, $\mathbf{\Gamma}_o$, to a new state $\mathbf{\Gamma}_n$ can be explicitly expressed as follows:

[3] Another solution to Eq. (1.17) is $\Pi_{on} = P_n/(P_o + P_n)$. This is often referred to as Barker sampling and appears to have lower statistical efficiency than the Metropolis solution Eq. (1.18) [18].

- In the case of the canonical ensemble (fixed N, V, T), the phase space probability is given by Eq. (1.9) and the Monte Carlo transition probability reads:

$$acc(o \to n) = \min\left\{1, \mathrm{e}^{-\beta[E(\mathbf{\Gamma}_n)-E(\mathbf{\Gamma}_o)]}\right\} \tag{1.19}$$

- The isothermal-isobaric ensemble (fixed N, pressure p, T) extends the canonical ensemble by allowing the simulation volume to fluctuate, while the average volume is controlled by p. The partition function is given by

$$\Delta(N, p, T) = \int Q_{\mathrm{id}}(N, V)\mathrm{e}^{-\beta pV} Q_{\mathrm{conf}}(N, V, T)\mathrm{d}V \tag{1.20}$$

  and the phase space probability is

$$P_{NpT}(\mathbf{\Gamma}) = \frac{Q_{\mathrm{id}}[N, V(\mathbf{\Gamma})]\mathrm{e}^{-\beta[E(\mathbf{\Gamma})+pV(\mathbf{\Gamma})]}}{\Delta(N, p, T)} \tag{1.21}$$

  leading to the Monte Carlo transition rule:

$$acc(o \to n) = \min\left\{1, \mathrm{e}^{-\beta[E(\mathbf{\Gamma}_n)-E(\mathbf{\Gamma}_o)]-\beta p[V(\mathbf{\Gamma}_n)-V(\mathbf{\Gamma}_o)]-N\ln[V(\mathbf{\Gamma}_n)/V(\mathbf{\Gamma}_o)]}\right\} \tag{1.22}$$

- For the grand-canonical ensemble (fixed chemical potential μ, V, T), particle numbers are allowed to fluctuate and the average number density N/V is controlled by μ. The partition function is given by

$$\Xi(\mu, V, T) = \sum_{N=0}^{\infty} Q_{\mathrm{id}}(N, V)\mathrm{e}^{\beta\mu N} Q_{\mathrm{conf}}(N, V, T) \tag{1.23}$$

  and the phase space probability is

$$P_{\mu VT}(\mathbf{\Gamma}) = \frac{Q_{\mathrm{id}}[N(\mathbf{\Gamma}), V]\mathrm{e}^{-\beta[E(\mathbf{\Gamma})-\mu N(\mathbf{\Gamma})]}}{\Xi(\mu, V, T)} \tag{1.24}$$

  resulting in the grand-canonical acceptance rule for particle additions and deletions:

$$acc(o \to n) = \min\left\{1, \frac{V^{N(\mathbf{\Gamma}_n)}\lambda^{DN(\mathbf{\Gamma}_o)}N(\mathbf{\Gamma}_o)!}{V^{N(\mathbf{\Gamma}_o)}\lambda^{DN(\mathbf{\Gamma}_n)}N(\mathbf{\Gamma}_n)!}\mathrm{e}^{-\beta[E(\mathbf{\Gamma}_n)-E(\mathbf{\Gamma}_o)]+\beta\mu[N(\mathbf{\Gamma}_n)-N(\mathbf{\Gamma}_o)]}\right\} \tag{1.25}$$

All of these Monte Carlo acceptance rules are independent of the partition function which is relevant for the ensemble as this normalisation constant vanishes by cancellation when the ratio defined in Eq. (1.18) is formed. It is thus possible to sample equilibrium configurations for a statistical ensemble without needing to know the partition function

itself! In practice, the algorithm is implemented by generating a random number R uniformly on the interval $[0, 1]$ and accepting the move if $R \leq P_n/P_o$.

1.2.2 Practical implementation

In order to use the Monte Carlo method on a computer, a suitable representation of the interacting particles needs to be devised. The most widely used method is to employ a real-space representation[4] using position and orientation coordinates for each particle. Energies are often evaluated using approximate[5] pair-decomposable potentials, i.e. the interaction between two particles depends only their distance and relative orientation,

$$E = \sum_{i>j} u(i, j) \tag{1.26}$$

where the summation includes all distinct pairs $\langle ij \rangle$. A typical functional form representing classical interactions between two atoms separated by a distance $r = |\boldsymbol{r}_i - \boldsymbol{r}_j|$ is the Lennard-Jones potential,

$$u(i, j) \mapsto u\left(r\right) = 4\epsilon \left[\left(\frac{\sigma}{r}\right)^{12} - \left(\frac{\sigma}{r}\right)^{6} \right] \tag{1.27}$$

which is plotted in Fig. 1.7. The parameters σ and ϵ set the diameter and potential well depth, respectively. It is convenient to define all physical quantities in units of σ and ϵ; this defines a set of so-called reduced units characteristic of the length- and energy scales of the simulated model. Some often used quantities are collected in Table 1.1. The advantage of using reduced units is that, if the potential takes the form $u(r) = \epsilon f(r/\sigma)$, there is a principle of corresponding states for all thermodynamic, structural and dynamic properties [18]. This enables one to compare characteristic parameters like the location of a critical point between different models.

Particle-based computer simulations are typically restricted to relatively small system sizes with 10^3–10^4 particles. A naïve approach to compute the bulk properties of such a system with no special treatment of the boundary conditions of the simulation box would suffer severely from the fact that a large number of particles are located at the surface. Such a simulation would thus not be representative of the behaviour of a bulk system where only a minute fraction of particles is located at the surface of a macroscopic volume. One solution is to introduce *periodic boundary conditions*, where the system

[4] It is also possible to use a many-body field-theoretical description where the interactions between all particles are represented using functional integrals over fields associated with the Fourier transform of the number density, $\rho(\boldsymbol{q})$. The mapping into field-space is performed via the Hubbard-Stratonovich transformation, see Ref. [19] for a recent review in the context of complex fluids.

[5] Realistic potentials incorporate induced electric multipole moments which depend on interactions with all particles and are therefore not pair-decomposable.

Table 1.1: Typical reduced units.

quantity	reduced units
number density N/V	$\rho^* = \rho\sigma^3$
temperature	$T^* = k_B T/\epsilon$
energy	$E^* = E/\epsilon$
pressure	$p^* = p\sigma^3/\epsilon$
time	$t^* = t\sqrt{\epsilon/m\sigma^2}$
force	$f^* = f\sigma/\epsilon$

is surrounded by replicas of itself. However, this method allows for the possibility that a particle can interact with multiple copies of another particle, or itself, which is clearly nonphysical. This problem is circumvented by introducing the *minimum image convention* which ensures that only interactions between distinct copies are allowed, namely those which are closest by distance. See Fig. 1.8 for a graphical representation of periodic boundary conditions and the minimum image convention.

1.2.3 Measurements

With the basic Monte Carlo samplings schemes defined in Eqns. (1.19–1.25), and a suitably defined particle interaction potential, measurable quantities of interest can be accumulated during the course of a simulation. Because Monte Carlo simulations do

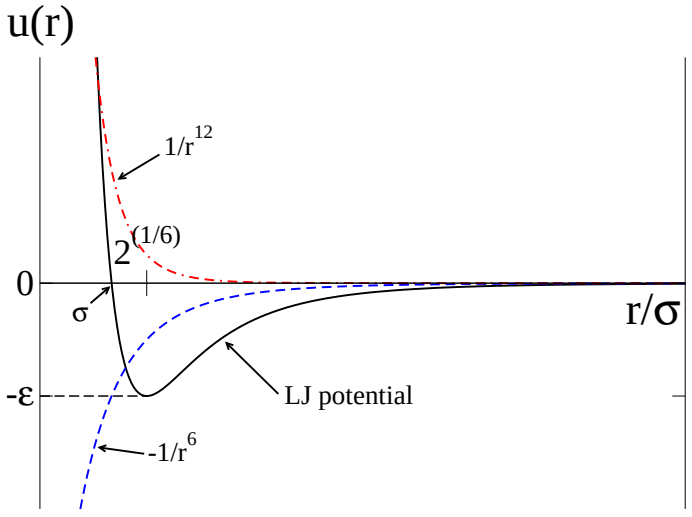

Figure 1.7: The Lennard-Jones potential. Crossing of the abscissa at $r = \sigma$ defines the particle diameter. The potential well depth is found at $r = 2^{\frac{1}{6}}\sigma$.

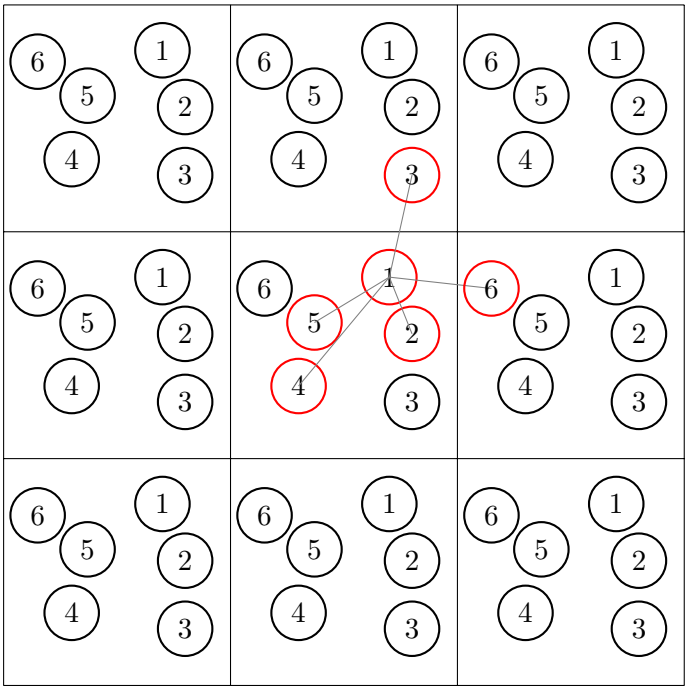

Figure 1.8: Periodic boundary conditions and minimum image convention in two dimensions. The central box is surrounded by replicas, particle '1' in the central box interacts across replica boundaries with closest neighbouring particles.

not yield physically correct dynamics, only structural, time-independent quantities can be measured. For example, we have the average of the instantaneous configurational energy $E_i = \sum_{j>k}^{N} u(j,k)$,

$$\langle E \rangle = \frac{1}{K} \sum_{i}^{K} E_i. \tag{1.28}$$

In the following, $\langle \cdots \rangle$ will be used as a short-hand notation for a simulation average like the above equation. Fluctuations in the observed E_i are also of interest. In the NVT-ensemble, the canonical heat capacity is given by

$$c_V = \frac{\langle E^2 \rangle - \langle E \rangle^2}{k_B T^2 N}. \tag{1.29}$$

Similarly, the variance of the distribution of observed particle numbers in the μVT-ensemble is related to the isothermal compressibility.

$$\kappa_T = \frac{\beta}{\rho} \frac{\langle N^2 \rangle - \langle N \rangle^2}{\langle N \rangle} \tag{1.30}$$

It is of particular interest to describe the complicated structure of the entire system in terms of reduced, easily accessible relations. This means in most cases that these relations contain only a limited subset of the entire information encoded in the complete

configuration of the system, however, thermodynamic quantities can indeed be described without referring to the particles' coordinates. The *two-particle distribution function* $\rho^{(2)}(\boldsymbol{r}, \boldsymbol{r}')$ defines the probability of finding one particle at position $\boldsymbol{r}$ and the other particle at $\boldsymbol{r}'$, irrespective of the positions of all other particles.

$$\rho^{(2)}(\boldsymbol{r}, \boldsymbol{r}') = \left\langle \sum_{i=1}^{N} \sum_{j \neq i}^{N} \delta(\boldsymbol{r} - \boldsymbol{r}_i) \delta(\boldsymbol{r}' - \boldsymbol{r}_j) \right\rangle \tag{1.31}$$

If the system is isotropic and homogeneous, $\rho^{(2)}(\boldsymbol{r}, \boldsymbol{r}')$ is only a function of the separation $r = |\boldsymbol{r}' - \boldsymbol{r}|$. An explicit transformation of Eq. (1.31) to depend only on r is achieved by substituting $\boldsymbol{r} = \boldsymbol{r} + \boldsymbol{r}'$, choosing $\boldsymbol{r}'$ as the origin from which r is measured and integrating over all $\boldsymbol{r}'$:

$$\begin{aligned}
\rho^{(2)}(\boldsymbol{r} + \boldsymbol{r}', \boldsymbol{r}') &= \left\langle \sum_{i=1}^{N} \sum_{j \neq i}^{N} \delta(\boldsymbol{r} + \boldsymbol{r}' - \boldsymbol{r}_i) \delta(\boldsymbol{r}' - \boldsymbol{r}_j) \right\rangle \\
\int_V \rho^{(2)}(\boldsymbol{r} + \boldsymbol{r}', \boldsymbol{r}') \mathrm{d}\boldsymbol{r}' &= \left\langle \sum_{i=1}^{N} \sum_{j \neq i}^{N} \delta(\boldsymbol{r} + \boldsymbol{r}_j - \boldsymbol{r}_i) \right\rangle \\
\int_V \rho^{(2)}(|\boldsymbol{r} - \boldsymbol{r}'|) \mathrm{d}\boldsymbol{r}' &= \left\langle \sum_{i=1}^{N} \sum_{j \neq i}^{N} \delta(\boldsymbol{r} + \boldsymbol{r}_j - \boldsymbol{r}_i) \right\rangle \\
4\pi r^2 V \rho^{(2)}(r) &= \left\langle \sum_{i=1}^{N} \sum_{j \neq i}^{N} \delta(\boldsymbol{r} + \boldsymbol{r}_j - \boldsymbol{r}_i) \right\rangle
\end{aligned} \tag{1.32}$$

The *radial distribution function* $g_{000}(r) = \rho^{(2)}(r)/\rho^2$ relates the interacting two particle distribution function to that of an ideal gas of the same number density. It is thus a measure for the density correlations introduced by the particle interactions. We have, in final form

$$g_{000}(r) = \frac{1}{4\pi N \rho r^2} \left\langle \sum_{i} \sum_{j \neq i} \delta(r - r_{ij}) \right\rangle. \tag{1.33}$$

$g_{000}(r)$ provides all pair expectation values which depend only on distance. For example, if the interaction potential is isotropic and pairwise additive, the expectation value for the energy becomes

$$\langle E \rangle = 2\pi N \rho \int_0^\infty r^2 u(r) g_{000}(r) \mathrm{d}r. \tag{1.34}$$

Similarly, the compressibility can be related to an integral over $g_{000}(r)$:

$$\kappa_T = \frac{\beta}{\rho} + 4\beta\pi \int_0^\infty r^2 \left[g_{000}(r) - 1 \right] \mathrm{d}r. \tag{1.35}$$

The *total correlation function* is defined as $h_{000}(r) = g_{000}(r) - 1$. Its Fourier transform is known as the *structure factor* $S(q)$. It is the response function of the number density to a weak external perturbation of wavelength $2\pi/q$, and is experimentally accessible to neutron and X-ray scattering experiments.

$$\begin{aligned} S(q) &= 1 + \rho \int_V h_{000}(\mathbf{r}) \mathbf{e}^{-\mathbf{iqr}} \mathrm{d}\mathbf{r} \\ &= 1 + 4\pi\rho \int_0^\infty h_{000}(r) r^2 \frac{\sin(qr)}{qr} \mathrm{d}r \end{aligned} \tag{1.36}$$

In principle, the structure factor contains exactly the same information as $g_{000}(r)$ because they are related via the Fourier transform. It is however useful to examine the structure using both the real-space and reciprocal space description in order to gain understanding about the system. Additionally, the structure factor is related to many thermodynamic properties in a more direct fashion than $g_{000}(r)$.

If systems with anisotropic particles are studied, as in the case of e.g. dipolar hard spheres, the distance dependence of angular correlations between particles can be defined by the projections of pair distribution functions on rotational invariants [20]:

$$h_{110}(r) = \frac{\left\langle \sum_i \sum_{j \neq i} \delta(r - r_{ij}) \boldsymbol{e}_i \cdot \boldsymbol{e}_j \right\rangle}{4\pi N \rho r^2} \tag{1.37}$$

$$h_{112}(r) = \frac{3}{2} \frac{\left\langle \sum_i \sum_{j \neq i} \delta(r - r_{ij}) [3(\boldsymbol{e}_i \cdot \hat{\boldsymbol{r}}_{ij})(\boldsymbol{e}_j \cdot \hat{\boldsymbol{r}}_{ij}) - \boldsymbol{e}_i \cdot \boldsymbol{e}_j] \right\rangle}{4\pi N \rho r^2} \tag{1.38}$$

$$h_{220}(r) = \frac{5}{2} \frac{\left\langle \sum_i \sum_{j \neq i} \delta(r - r_{ij}) [3(\boldsymbol{e}_i \cdot \boldsymbol{e}_j)^2 - 1] \right\rangle}{4\pi N \rho r^2}, \tag{1.39}$$

where $\hat{\boldsymbol{r}}_{ij} = \boldsymbol{r}_{ij}/|\boldsymbol{r}_{ij}|$ and $\boldsymbol{e}_i$ is the orientation of the ith particle. In the case of dipoles, the total energy of the system can be expressed as an integral over $h_{112}(r)$,

$$\langle E \rangle_{dipolar} = 2\pi\rho N \int_0^\infty -\frac{2}{3} \mu^2 r^{-3} h_{112}(r) \mathrm{d}r, \tag{1.40}$$

and the dielectric constant is related to an integral over $h_{110}(r)$ [21].

The remainder of this work is structured as follows: In Chapter 2, advanced Monte Carlo sampling methods addressing some of the problems associated with the simulation of phase transitions in general are developed. Applications of these methods are presented in Chapters 3 and 4. Vapour-liquid criticality and the crossover behaviour between ionic

and dipolar interactions are then addressed in Chapter 6 using a model of charged hard dumbbells. Finally, the issue of a vapour-liquid phase transition in dipolar hard spheres is investigated in Chapter 7.

Part I – Advanced Monte Carlo methods

Chapter 2

Flat histogram Monte Carlo sampling

The results obtained from computer simulations of many-body systems rely on averaging a large number of observable properties over statistically independent configurations. However, in practice the generation of statistically uncorrelated states is complicated by the existence of free energy barriers between regions of phase space with high Boltzmann probabilities. This point is illustrated in Fig. 2.1. These probability bottlenecks play no role for macroscopic system sizes and timescales, but the accuracy of computer simulations may be severely decreased if important regions of phase space are not accessed in finite simulation time. In the context of the vapour-liquid phase transition, the free energy barrier is due to the formation of an interface which separates the dilute gas from the dense liquid. This interface poses formidable problems to computer simulations of phase coexistence at subcritical temperatures: if the temperature is cooled from supercritical to subcritical temperatures along the coexistence isochore, a thermal fluctuation suffices to carry the system in one of its two phases and the low probability of crossing between two phases then leads to an apparent broken symmetry. This potential pitfall is illustrated in Fig. 2.2 where the grand-canonical number density probability distribution for a typical vapour-liquid transition is shown. It can be seen that the transition probability to switch between two phases can attain very low values at subcritical temperatures.

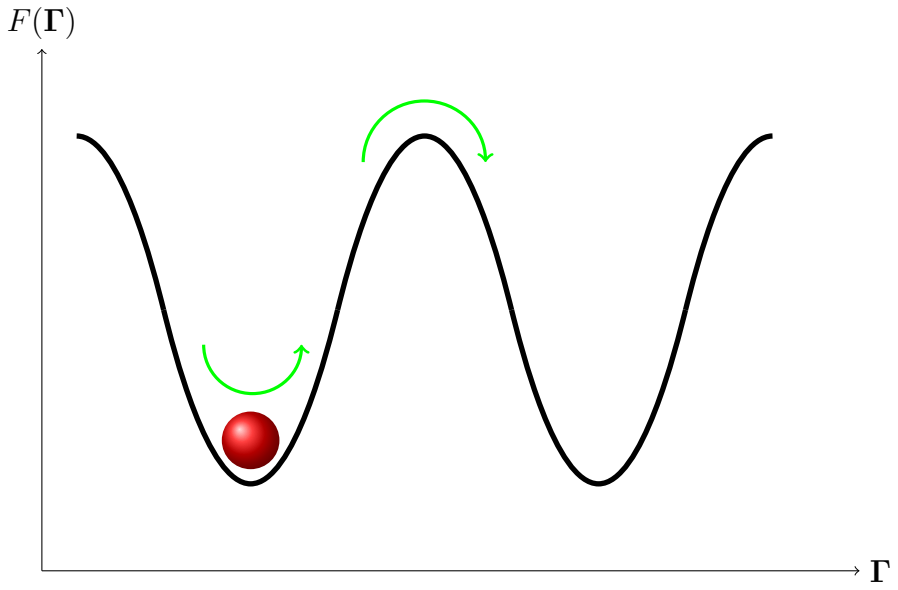

Figure 2.1: Free energy F as a function of phase space coordinate $\mathbf{\Gamma}$. The maxima in F suppress fluctuations between minima which correspond to regions with high Boltzmann probabilities. Imperfect statistical sampling arises when the system becomes trapped in in one minimum, leading to the wrong ensemble average.

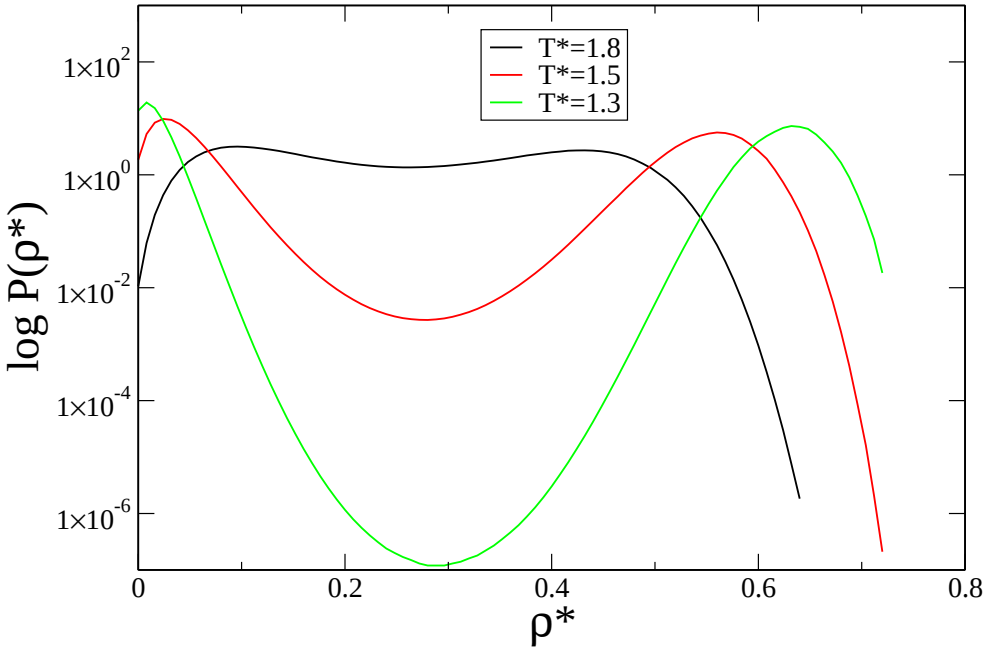

Figure 2.2: Number density probability distributions from *GCMC* simulations for a square-well fluid with $T_c^* = 1.8$ at different temperatures.

2.1 Overcoming free energy barriers: Umbrella sampling

Special techniques have been invented to overcome the sampling problems associated with free energy barriers. Historically the most important method is the *umbrella sampling method* due to Torrie and Valleau [22], where the simulation trajectory is obtained using a modified, non-Boltzmann probability $\tilde{P}(\mathbf{\Gamma}) \propto P_0(\mathbf{\Gamma}) \exp[W(\mathbf{\Gamma})]$, where $P_0(\mathbf{\Gamma})$ is the proper Boltzmann probability and $W(\mathbf{\Gamma})$ is an arbitrary perturbation in units of k_BT. This new probability can be chosen such that its corresponding free energy landscape is flat and the simulation does not suffer from sampling problems. The true partition function $Q_0 = \int \exp[-\beta E(\mathbf{\Gamma})] \mathrm{d}\mathbf{\Gamma}$ is related to the biased partition function $\tilde{Q}$ in the following way,

$$\begin{aligned} \tilde{Q}/Q_0 &= \int \exp[-\beta E(\mathbf{\Gamma})] \exp[W(\mathbf{\Gamma})] \mathrm{d}\mathbf{\Gamma}/Q_0 \\ &\therefore \\ Q_0 &= \frac{\tilde{Q}}{\langle \exp[W(\mathbf{\Gamma})] \rangle_0} \end{aligned} \tag{2.1}$$

where the notation $\langle \cdots \rangle_0$ refers to an ensemble average accumulated with the unbiased probability $P_0(\mathbf{\Gamma})$. Simulation averages for the unbiased case with $W(\mathbf{\Gamma}) = 0$ can be recovered from the biased simulation exactly through the following relationship,

$$\begin{aligned} \langle A(\mathbf{\Gamma}) \exp[-W(\mathbf{\Gamma})] \rangle_\sim / Q_0 &= \int A(\mathbf{\Gamma}) \exp[-W(\mathbf{\Gamma})] \tilde{P}(\mathbf{\Gamma}) \mathrm{d}\mathbf{\Gamma}/\tilde{Q}Q_0 \\ &= \int A(\mathbf{\Gamma}) \exp[-\beta E(\mathbf{\Gamma})] \mathrm{d}\mathbf{\Gamma}/\tilde{Q}Q_0 \\ &\therefore \\ \langle A(\mathbf{\Gamma}) \rangle_0 &= \frac{\tilde{Q}}{Q_0} \langle A(\mathbf{\Gamma}) \exp[-W(\mathbf{\Gamma})] \rangle_\sim \end{aligned} \tag{2.2}$$

where the notation $\langle \cdots \rangle_\sim$ refers to an ensemble average accumulated with the biased probability $\tilde{P}(\mathbf{\Gamma})$. Ideally, one would like the non-Boltzmann probability to be a constant as the biased simulation would then perform a random walk in phase space. However, this is wishful thinking as the requirement for this, $\exp[W(\mathbf{\Gamma})] \propto 1/P_0(\mathbf{\Gamma})$, implies that we know the absolute Boltzmann probabilities *a priori* which is not possible. Nevertheless, the biasing distribution $W(\mathbf{\Gamma})$ can be obtained iteratively if one starts an unbiased simulation at a thermodynamic state point which does not suffer from free energy barriers. Berg and Neuhaus [23] have given a formulation for such an iterative scheme in the canonical ensemble, which is referred to as *multi-canonical sampling*. As the focus of this work is mainly on the study of phase transitions in the grand-canonical ensemble, the iterative scheme which is employed in Chapter 6 to obtain the phase diagram of charged hard dumbbells is outlined below.

1. Obtain the number probability distribution $P(N)$ at a temperature and chemical potential close to criticality.

2. Obtain an estimate for the new $P(N)_{\text{est.}}$ at a slightly lower temperature T_{new} with the chemical potential μ_{new} chosen such that $P(N)_{\text{est.}}$ is bimodal with equal areas under each peak using the histogram reweighting technique [24]. Form the biasing distribution $W(N) = 1/P(N)$.

3. Perform a new simulation at T_{new} using the non-Boltzmann probability $\tilde{P}(\mathbf{\Gamma}) = P_0(\mathbf{\Gamma})/P(N)$.

4. The observed number probability distribution $\tilde{P}(N)$ in the biased simulation will be approximately flat, depending on the statistical precision of $P(N)$. Recover the true Boltzmann probability $P_0(N)$ at $T_{\text{new}}, \mu_{\text{new}}$ from $P_0(N) = \tilde{P}(N)/W(N)$.

5. If a simulation at yet another subcritical temperature is desired, go to step 2.

While this scheme works reliably in practice, it is somewhat cumbersome to use it because it requires to step down a temperature range in small intervals with manual interaction involved after each step. This inconvenience leads to the question if it is not possible to directly determine the biasing distribution W. This will necessarily be an iterative process as these weights are related to partition functions – in the last case, $W(N) = 1/P(N)_{\text{est.}} \propto 1/Q(N, V, T)\exp(\beta\mu N)$, for example. The next section presents a general procedure for obtaining these weights from a single simulation.

2.2 Flat histogram sampling of mechanical variables

As exemplified above, Monte Carlo importance sampling may in some cases suffer from free energy barriers which render the simulation essentially non-ergodic in finite simulation time. Ideally, we would like to carry out a simulation in a biased ensemble where the distribution of the relevant fluctuating mechanical variables is uniform. In the following, biased Monte Carlo acceptance rules which facilitate uniform sampling of these variables are derived.

2.2.1 Canonical Ensemble

In the canonical ensemble we usually observe a sharply peaked distribution around some energy. The aim is now to derive *microstate* probabilities corresponding to an ensemble where this distribution is uniform. Once the microstate probabilities are expressed in closed form, they can be utilised in a Metropolis scheme to yield a valid Monte Carlo

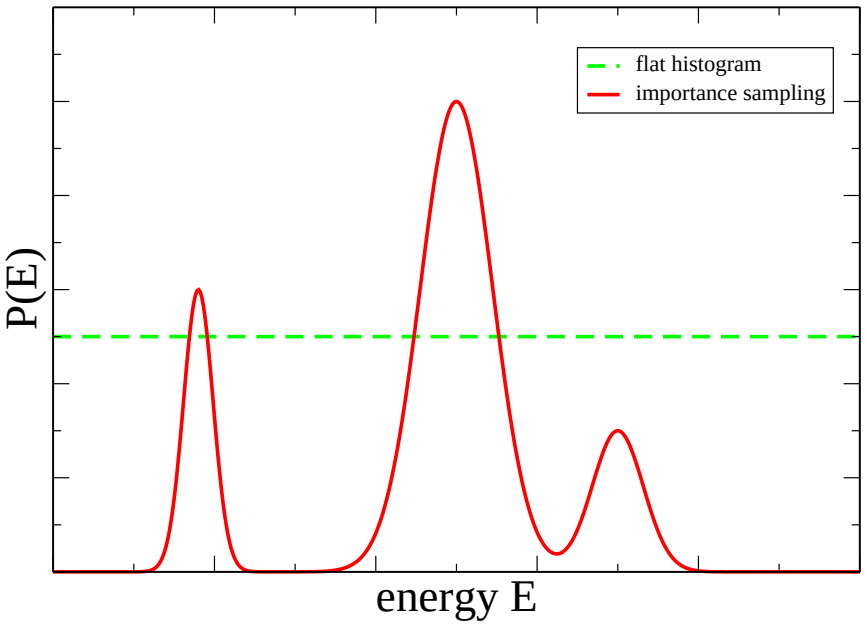

Figure 2.3: Energy distribution in the canonical ensemble obtained using unbiased Metropolis sampling and biased flat-histogram sampling.

simulation which obeys detailed balance ultimately. The expected outcome is illustrated in Fig. 2.3.

The unbiased microstate probability with an associated energy $E(\mathbf{\Gamma})$ in the canonical ensemble reads:

$$P(\mathbf{\Gamma}) = \frac{Q_{\mathrm{id}}(N,V)}{Q(N,V,T)} \exp[-\beta E(\mathbf{\Gamma})] \tag{2.3}$$

Correspondingly, a *macrostate* probability is defined which expresses the probability of observing some energy E irrespective of the microscopic details,

$$\begin{aligned} P(E) &= \int P(\mathbf{\Gamma})\delta[E - E(\mathbf{\Gamma})]\mathrm{d}\mathbf{\Gamma} \\ &= \frac{Q_{\mathrm{id}}(N,V)}{Q(N,V,T)} \Omega(E) \exp(-\beta E) \end{aligned} \tag{2.4}$$

where $\Omega(E) = \int \delta[E - E(\mathbf{\Gamma})]\mathrm{d}\mathbf{\Gamma}$ is a measure for the degeneracy of the energy level E. $\Omega(E)$ is usually referred to as the microcanonical partition function, or the density of

states (DOS). $P(E)$ is now used to define a *biased* microstate probability:

$$\begin{aligned} \tilde{P}(\mathbf{\Gamma}) &= \frac{P(\mathbf{\Gamma})}{P[E(\mathbf{\Gamma})]} \\ &= \frac{1}{\Omega[E(\mathbf{\Gamma})]} \end{aligned} \tag{2.5}$$

Note that this new microstate probability is unaffected by the *thermal field* β which weighed the energy distribution in the original canonical ensemble. The corresponding *biased* macrostate probability for any energy is now a constant as all degrees of freedom are integrated out,

$$\begin{aligned} \tilde{P}(E) &= \int \tilde{P}(\mathbf{\Gamma})\delta[E - E(\mathbf{\Gamma})]\mathrm{d}\mathbf{\Gamma} \\ &= \frac{1}{\Omega[E]} \int \delta[E - E(\mathbf{\Gamma})]\mathrm{d}\mathbf{\Gamma} \\ &\therefore \\ \tilde{P}(E) &= 1 \end{aligned} \tag{2.6}$$

and the Monte Carlo acceptance rules which satisfy detailed balance are readily obtained by inserting Eq. (2.5) into Eq. (1.18):

$$\begin{aligned} acc(o \to n) &= \min\left[1, \frac{\tilde{P}(\mathbf{\Gamma}_n)}{\tilde{P}(\mathbf{\Gamma}_o)}\right] \\ &= \min\left\{1, \frac{\Omega[E(\mathbf{\Gamma}_o)]}{\Omega[E(\mathbf{\Gamma}_n)]}\right\}. \end{aligned} \tag{2.7}$$

However, it is not possible to employ the above sampling scheme directly as the weights $\Omega[E(\mathbf{\Gamma})]$ are an unknown quantity at the start of the simulation. An effective algorithm to solve for the density of states in a self-consistent fashion was introduced by Wang and Landau [25] in 2001 (abbreviated in the following as the WL-algorithm) and is stated below.

1. At the beginning of the simulation, the energy range $[E_{min}, E_{max}]$ to be sampled must be decided upon. For lattice systems it can be a trivial task to determine the lowest and highest energies attainable by the model, but for off-lattice systems this will usually require some trial and error. In any case, the energy limits must bracket the thermally accessible energies for the range of temperatures one is interested in. For the density of states an initial guess is made, e.g. $\Omega(E) = \text{constant} \forall E$.

2. Define a histogram $H(E)$ of visited energy states (or discretised energy bins for continuous models) and set it to zero.

3. Propose moves from $\mathbf{\Gamma}_o$ to $\mathbf{\Gamma}_n$ and accept using Eq. (2.7). After each move, successful or not, update the current estimate of the density of states via $\Omega(E) \rightarrow f \times \Omega(E)$, where f is an arbitrary convergence factor greater than unity. Similarly, update the visited energy histogram via $H(E) \rightarrow H(E) + 1$.

4. Due to the dynamic updating of $\Omega(E)$, the simulation is always pushed away from the current energy state in the next Monte Carlo move and $H(E)$ will eventually become flat. When this is the case reduce f, e.g., via $f \rightarrow \sqrt{f}$.

5. Check if f is smaller than a required convergence criterion. In practice this means that f is so close to unity that future updates of $\Omega(E)$ are negligible. If this is the case, terminate the simulation. Otherwise continue with step 2.

It is apparent that there is substantial freedom in the parameters of this recipe, such as the initial value of the convergence factor f or the criterion when $H(E)$ is termed 'flat'. Nevertheless the convergence of the WL-algorithm has been formally proved [26], but the optimal choice for these parameters will depend on the actual system studied. The speed of convergence and residual error are sensitive to these parameters and care must be taken in order not to reduce f too quickly [27]. The general idea to determine $\Omega(E)$ iteratively is not altogether new, as this was realised before in Lee's 1993 *entropic sampling* [28] and by Berg and Neuhaus in 1992 with their *multi-canonical sampling* methods [23]. However, the newer WL algorithm differs from both these schemes in that the update is performed via a multiplication operation as opposed to an addition.

At the end of a converged flat histogram simulation in the canonical ensemble, one does not directly have statistical expectation values for some temperature but rather an accurate estimate for the density of states. This enables the calculation of expectation values at arbitrary values of the temperature via a Laplace transform:

$$\langle A \rangle_\beta = \frac{\int_{E_{\min}}^{E_{\max}} A(E)\Omega(E)\exp(-\beta E)\mathrm{d}E}{\int_{E_{\min}}^{E_{\max}} \Omega(E)\exp(-\beta E)\mathrm{d}E}. \tag{2.8}$$

Thus, all the usual observables such as $\langle E \rangle$ and $C_V = (\langle E^2 \rangle - \langle E \rangle^2)/k_B T^2$ are available over a continuous range of temperatures using the output from a single simulation. Similarly, the Helmholtz free energy is obtained from:

$$\langle F \rangle_\beta = -k_B T \ln \int_{E_{\min}}^{E_{\max}} \Omega(E)\exp(-\beta E)\mathrm{d}E \tag{2.9}$$

Because $\Omega(E)$ can, in general, only be determined up to a multiplicative constant, $\langle F \rangle_\beta$ is only known up to an additive constant with the exception of some lattice systems where the energetic ground state is accessible and its degeneracy is known.

2.2.2 Generalisation to mechanically coupled ensembles

The above derivation can be readily applied to an ensemble where, besides the coupling of the energy to a heatbath, a mechanically extensive variable X is coupled to the surroundings via an additional field ξ. The partition function is thus defined by

$$\Xi(\beta, \xi, V) = \int Q_{\mathrm{id}}(N, V) \exp\left[-\beta E(\mathbf{\Gamma}) - \beta \xi X(\mathbf{\Gamma})\right] \mathrm{d}\mathbf{\Gamma} \tag{2.10}$$

and the unbiased microstate probability for any element of configuration space reads:

$$P(\mathbf{\Gamma}) = \frac{Q_{\mathrm{id}}(N, V)}{\Xi(\beta, \xi, V)} \exp[-\beta E(\mathbf{\Gamma}) - \beta \xi X(\mathbf{\Gamma})] \tag{2.11}$$

The field ξ could be an external magnetic field and X the magnetisation in which case we would recover the partition function for a magnetic system. Similarly the grand-canonical or isothermal-isobaric ensembles are obtained if ξ represents the chemical potential or the external pressure, in which case X would correspond to the number of particles N or the volume V, respectively. The aim is now to obtain microstate probability expressions which sample all E and X with equal probability. The unbiased joint macrostate probability for any E, X reads

$$\begin{aligned} P(E, X) &= \int P(\mathbf{\Gamma}) \delta[E - E(\mathbf{\Gamma})] \delta[X - X(\mathbf{\Gamma})] \mathrm{d}\mathbf{\Gamma} \\ &= \frac{Q_{\mathrm{id}}(N, V)}{\Xi(\beta, \xi, V)} \Omega(E, X) \exp(-\beta E - \beta \xi X) \end{aligned} \tag{2.12}$$

where $\Omega(E, X) = \int \delta[E - E(\mathbf{\Gamma})] \delta[X - X(\mathbf{\Gamma})] \mathrm{d}\mathbf{\Gamma}$ is the density of states for the combined occurrence of E and X. This expression is used to define a *biased* microstate probability,

$$\begin{aligned} \tilde{P}(\mathbf{\Gamma}) &= \frac{P(\mathbf{\Gamma})}{P[E(\mathbf{\Gamma}), X(\mathbf{\Gamma})]} \\ &= \frac{1}{\Omega[E(\mathbf{\Gamma}), X(\mathbf{\Gamma})]} \end{aligned} \tag{2.13}$$

which corresponds again to a constant biased macrostate probability for observing any E, X:

$$\begin{aligned}
\tilde{P}(E,X) &= \int \tilde{P}(\mathbf{\Gamma})\delta[E - E(\mathbf{\Gamma})]\delta[X - X(\mathbf{\Gamma})]\mathrm{d}\mathbf{\Gamma} \\
&= \frac{1}{\Omega[E,X]} \int \delta[E - E(\mathbf{\Gamma})]\delta[X - X(\mathbf{\Gamma})]\mathrm{d}\mathbf{\Gamma} \\
&\therefore \\
\tilde{P}(E,X) &= 1
\end{aligned} \tag{2.14}$$

As the above derivation has been completely general, consider now the Ising model as an example to implement uniform sampling of energy E and magnetisation M (corresponding to the mechanical variable X above). Additionally, let us denote the external magnetic field by h (corresponding to ξ above). The unbiased Boltzmann phase space probability then reads:

$$P(\mathbf{\Gamma}) = \exp\left[-\beta E(\mathbf{\Gamma}) - \beta h M(\mathbf{\Gamma})\right] / \Xi(\beta, h, V) \tag{2.15}$$

Note that, for the Ising model, $Q_{\mathrm{id}}(N,V) = 1$, because (i) lattice sites are distinguishable, (ii) there are strictly only classical degrees of freedom, and (iii) there is no kinetic energy term. Applying the above formalism yields:

1. Define the unbiased microstate probability $P(\mathbf{\Gamma})$.
2. Define the unbiased macrostate probability $P(E,M) = \int P(\mathbf{\Gamma})\delta[E - E(\mathbf{\Gamma})]\delta[M - M(\mathbf{\Gamma})]\mathrm{d}\mathbf{\Gamma}$.
3. Define the biased microstate probability $\tilde{P}(\mathbf{\Gamma}) = P(\mathbf{\Gamma})/P[E(\mathbf{\Gamma}), X(\mathbf{\Gamma})]$
4. Obtain the uniform sampling Monte Carlo rules by inserting the biased microstate probability expression into the detailed balance condition:

$$\mathrm{acc}(o \to n) = \min\left\{1, \frac{\Omega[E(\mathbf{\Gamma}_o), M(\mathbf{\Gamma}_o)]}{\Omega[E(\mathbf{\Gamma}_n), M(\mathbf{\Gamma}_n)]}\right\} \tag{2.16}$$

As with the uniform sampling of all energies in the canonical case above, all reference to the coupling thermodynamic fields vanishes. In order to solve for the unknown $\Omega[E,M]$, the WL algorithm can be employed. Once converged, the joint density of states enables the calculation of expectation values over wide ranges of temperature and external magnetic field, all from a single simulation. However, in this case a two-dimensional surface has to be iteratively determined which, in practice is only possible for small systems. An example of such a simulation can be found in Ref. [29], and similar applications to systems with continuous degrees of freedom in Refs. [30, 31]. A certain improvement in

convergence speed can be realised by partitioning the sampling range into smaller windows or stripes, which can be understood in terms of a random walker which traverses the sampling surface. The WL algorithm relies on local updates of the density of states and $\Omega(E, X)$ has to be updated for all values of E and X before one convergence cycle can be completed. The dynamics of the local walker can be approximated by an ideal random walk, describing a diffusion process, with a round trip time proportional to the square of the system size, $\tau \propto L^2$ [32]. Splitting the total system into k equally sized partitions, the required time to converge all of these simulations scales as $k\tau_k \propto L^2/k^2$ which result in a speedup $\tau_k/\tau \propto 1/k$. Nevertheless it remains impossible to obtain a well converged joint density of states for any off-lattice model with a system size of a few hundred particles which can be considered the absolute minimum by today's standards.

2.2.3 Hybrid flat histogram sampling

In order to alleviate the huge sampling problem associated with a two-dimensional joint density of states and be able to apply flat-histogram sampling to interesting model systems of acceptable system sizes, a Monte Carlo scheme which maintains a Boltzmann distribution for the energy but otherwise samples a mechanical variable uniformly was investigated by the author in Ref. [33]. The starting point for the derivation of such a scheme is the ensemble defined in Eq. (2.11) but now the macrostate probability for a value of X irrespective of E is required:

$$\begin{aligned} P(X) &= \int P(\mathbf{\Gamma})\delta[X - X(\mathbf{\Gamma})]\mathrm{d}\mathbf{\Gamma} \\ &= \int Q_{\mathrm{id}}(N,V)\exp[-\beta E(\mathbf{\Gamma}) - \beta\xi X(\mathbf{\Gamma})]\delta[X - X(\mathbf{\Gamma})]\mathrm{d}\mathbf{\Gamma} \\ &= \exp(-\beta\xi X)Q_{\mathrm{id}}(N,V)\int \exp[-\beta E(\mathbf{\Gamma})]\delta[X - X(\mathbf{\Gamma})]\mathrm{d}\mathbf{\Gamma} \\ &= \exp(-\beta\xi X)Q(X,N,V,T) \end{aligned} \tag{2.17}$$

$Q(X,N,V,T) = Q_{\mathrm{id}}(N,V)\int \exp[-\beta E(\mathbf{\Gamma})]\delta[X - X(\mathbf{\Gamma})]\mathrm{d}\mathbf{\Gamma}$ is the canonical partition function corresponding to the Boltzmann weighted subset of phase space sporting a given value of the mechanical variable X, at fixed N, T, and V. The biased microstate probability is then defined through

$$\begin{aligned} \tilde{P}(\mathbf{\Gamma}) &= \frac{P(\mathbf{\Gamma})}{P[X(\mathbf{\Gamma})]} \\ &= \frac{Q_{\mathrm{id}}(N,V)\exp[-\beta E(\mathbf{\Gamma}) - \beta\xi X(\mathbf{\Gamma})]}{\exp[-\beta\xi X(\mathbf{\Gamma})]Q[X(\mathbf{\Gamma}),N,V,T]} \\ &= \frac{Q_{\mathrm{id}}(N,V)\exp\left[-\beta E(\mathbf{\Gamma})\right]}{Q\left[X(\mathbf{\Gamma}),N,V,T\right]}. \end{aligned} \tag{2.18}$$

It is straightforward to show that X is sampled uniformly using this microstate probability:

$$\begin{aligned}
\tilde{P}(X) &= \int \tilde{P}(\mathbf{\Gamma})\delta[X - X(\mathbf{\Gamma})]\mathrm{d}\mathbf{\Gamma} \\
&= \int \frac{Q_{\mathrm{id}}(N,V)\exp\left[-\beta E(\mathbf{\Gamma})\right]}{Q\left[X(\mathbf{\Gamma}),N,V,T\right]}\delta[X - X(\mathbf{\Gamma})]\mathrm{d}\mathbf{\Gamma} \\
&= \frac{1}{Q(X,N,V,T)}\int Q_{\mathrm{id}}(N,V)\exp\left[-\beta E(\mathbf{\Gamma})\right]\delta[X - X(\mathbf{\Gamma})]\mathrm{d}\mathbf{\Gamma} \\
&\therefore \\
\tilde{P}(X) &= 1
\end{aligned} \tag{2.19}$$

Fruitful application of the above result can be made in the grand-canonical and isobaric-isothermal ensembles where it is of interest to sample a wide range of number densities at fixed temperature. If this temperature is subcritical, prohibitively large free energy barriers prevent standard importance sampling algorithms to work as illustrated in Fig. 2.2. However, the flat-histogram sampling scheme will not suffer from this problem by definition. It should be noted that the constrained canonical partition function $Q(X,N,V,T)$ defined above is parameterised by four variables which represents the most general case. For the specific application of uniform number density sampling where X is given by either the volume V or the number of particles N, the number of parameters reduces to three.

- In the case of the grand-canonical ensemble, we obtain the biased microstate expression
$$\tilde{P}(\mathbf{\Gamma}) = \frac{Q_{\mathrm{id}}[N(\mathbf{\Gamma}),V]\exp\left[-\beta E(\mathbf{\Gamma})\right]}{Q\left[N(\mathbf{\Gamma}),V,T\right]}, \tag{2.20}$$
leading to the explicit uniform sampling Monte Carlo rule:
$$\mathrm{acc}(o\to n) = \min\left[1, \frac{Q(N_o,V,T)}{Q(N_n,V,T)}\frac{V^{N_n}N_o!\Lambda^{3N_o}\exp\left[-\beta E(\mathbf{\Gamma}_n)\right]}{V^{N_o}N_n!\Lambda^{3N_n}\exp\left[-\beta E(\mathbf{\Gamma}_o)\right]}\right] \tag{2.21}$$

- For the isothermal-isobaric ensemble, the biased microstate probability is given by
$$\tilde{P}(\mathbf{\Gamma}) = \frac{Q_{\mathrm{id}}(N,V)\exp\left[-\beta E(\mathbf{\Gamma})\right]}{Q\left[N,V(\mathbf{\Gamma}),T\right]}, \tag{2.22}$$
resulting in the uniform volume sampling Monte Carlo rule:
$$\mathrm{acc}(o\to n) = \min\left[1, \frac{Q(N,V_o,T)}{Q(N,V_n,T)}\frac{V_n^N\exp\left[-\beta E(\mathbf{\Gamma}_n)\right]}{V_o^N\exp\left[-\beta E(\mathbf{\Gamma}_o)\right]}\right] \tag{2.23}$$

The weights $Q(N,V,T)$ appearing in the above equations are unknown *a priori* and need to be determined iteratively by the WL algorithm. In the grand-canonical case

this involves deciding upon a range of particle numbers $\{N_{\min}..N_{\max}\}$ to be sampled, while the isothermal-isobaric simulation requires lower and upper bounds for the volume and a suitable discretisation thereof. Once converged results have been obtained, expectation values e.g. the average number of particles for a given chemical potential can be calculated:

$$\langle N \rangle_\mu = \frac{\sum_{N=N_{\min}}^{N_{\max}} N \exp(\beta\mu N) Q(N,V,T)}{\sum_{N=N_{\min}}^{N_{\max}} \exp(\beta\mu N) Q(N,V,T)} \tag{2.24}$$

The advantages of these sampling schemes are manifold for the study of phase coexistence. First of all, neither the chemical potential nor the pressure for coexistence have to be specified *a priori*, which usually requires many trial-and-error attempts in traditional Monte Carlo methods. The sampling algorithm can thus be used in a black-box manner without user intervention. Further, it is only a one dimensional sampling problem which permits application to interesting system sizes. The usability of this scheme is demonstrated in Chapter 4 where results for complex fluids with very rough free-energy landscapes and entropic bottlenecks are presented. Flat histogram sampling of extensive mechanical variables shall henceforth be abbreviated as WLEXT for 'Wang-Landau sampling of extensive mechanical variables'.

2.3 Flat histogram sampling of thermodynamic fields

While the preceding sampling schemes have focused on sampling mechanical extensive variables, it is also possible to sample the conjugate thermodynamic fields appearing in the partition function with uniform probability. As a thermodynamic field is coupled to a macroscopic observable (e.g., E is coupled to T by a Boltzmann distribution), a broad range of this observable can be visited by sampling a broad range of values for the field. This approach is somewhat similar to the expanded ensemble and replica exchange techniques [34–37] but here a simple and systematic derivation for such a MC sampling scheme is presented which does not need multiple copies of the same system to be propagated through phase space. However, the advantage of parallel tempering which allows the system to get around (rather than over, as in umbrella sampling) free energy barriers is preserved. To derive such probabilities, the starting point is the Boltzmann probability of a mechanically coupled ensemble, Eq. (2.11), incorporated into the following *über* partition function

$$\Psi = \int_{\beta_{min}}^{\beta_{\max}} \int_{\xi_{\min}}^{\xi_{\max}} \int \frac{Q_{\mathrm{id}}(N,V)}{\Xi(\beta,\xi,V)} \exp[-\beta E(\mathbf{\Gamma}) - \beta\xi X(\mathbf{\Gamma})] \mathrm{d}\beta \mathrm{d}\xi \mathrm{d}\mathbf{\Gamma}, \tag{2.25}$$

where the ensemble definition incorporates not only the mechanical configurations that the system can attain but also a range of the thermodynamic fields β and ξ. By exact analogy to the above derivation the unbiased microstate probability for any microscopic configuration is now defined

$$P(\mathbf{\Gamma},\beta,\xi) = \frac{Q_{\mathrm{id}}(N,V)}{\Psi}\exp[-\beta E(\mathbf{\Gamma}) - \beta\xi X(\mathbf{\Gamma})] \tag{2.26}$$

and the corresponding unbiased joint macrostate probability for observing a particular combination of (β,ξ) reads

$$\begin{aligned} P(\beta,\xi) &= \int_{\beta_{\min}}^{\beta_{\max}}\int_{\xi_{\min}}^{\xi_{\max}}\int P(\mathbf{\Gamma},\beta',\xi')\delta(\beta'-\beta)\delta(\xi'-\xi)\mathrm{d}\beta'\mathrm{d}\xi'\mathrm{d}\mathbf{\Gamma} \\ &= \frac{1}{\Psi}\int Q_{\mathrm{id}}(N,V)\exp[-\beta E(\mathbf{\Gamma}) - \beta\xi X(\mathbf{\Gamma})]\mathrm{d}\mathbf{\Gamma} \\ &= \frac{\Xi(\beta,\xi,V)}{\Psi} \end{aligned} \tag{2.27}$$

Continuing along the usual path, the biased microstate probability is again obtained by dividing the unbiased microstate probability by the unbiased macrostate probability:

$$\begin{aligned} \tilde{P}(\mathbf{\Gamma},\beta,\xi) &= \frac{P(\mathbf{\Gamma},\beta,\xi)}{P(\beta,\xi)} \\ &= \frac{Q_{\mathrm{id}}(N,V)}{\Xi(\beta,\xi,V)}\exp[-\beta E(\mathbf{\Gamma}) - \beta\xi X(\mathbf{\Gamma})] \end{aligned} \tag{2.28}$$

The above expression is of course just the Boltzmann probability in the general ensemble defined in Eq. (2.11). One might therefore argue that this derivation has turned itself in a circle, however, the corresponding biased macrostate probability shows that $\tilde{P}(\mathbf{\Gamma},\beta,\xi)$ indeed defines an ensemble with uniform probability of observing a particular combination of (β,ξ).

$$\begin{aligned} \tilde{P}(\beta,\xi) &= \int_{\beta_{\min}}^{\beta_{\max}}\int_{\xi_{\min}}^{\xi_{\max}}\int \tilde{P}(\mathbf{\Gamma},\beta',\xi')\delta(\beta'-\beta)\delta(\xi'-\xi)\mathrm{d}\beta'\mathrm{d}\xi'\mathrm{d}\mathbf{\Gamma} \\ &= \int \tilde{P}(\mathbf{\Gamma},\beta,\xi)\mathrm{d}\mathbf{\Gamma} \\ &= \frac{1}{\Xi(\beta,\xi,V)}\int Q_{\mathrm{id}}(N,V)\exp[-\beta E(\mathbf{\Gamma}) - \beta\xi X(\mathbf{\Gamma})]\mathrm{d}\mathbf{\Gamma} \\ &\therefore \\ \tilde{P}(\beta,\xi) &= 1 \end{aligned} \tag{2.29}$$

MC transition probabilities for changing the thermodynamic fields from (β_o, ξ_o) to (β_n, ξ_n) while maintaining the current phase space configuration $\mathbf{\Gamma}$ are obtained by inserting Eq. (2.28) into the Metropolis solution to the detailed balance condition, Eq. (1.18).

$$\begin{aligned} acc(o \to n) &= \min\left[1, \frac{\tilde{P}(\mathbf{\Gamma}, \beta_n, \xi_n)}{\tilde{P}(\mathbf{\Gamma}, \beta_o, \xi_o)}\right] \\ &= \min\left\{1, \frac{\Xi(\xi_o, \beta_o, V)}{\Xi(\xi_n, \beta_n, V)} \frac{\exp\left[-\beta_n E(\mathbf{\Gamma}) + \beta_n \xi_n X(\mathbf{\Gamma})\right]}{\exp\left[-\beta_o E(\mathbf{\Gamma}) + \beta_o \xi_o X(\mathbf{\Gamma})\right]}\right\} \end{aligned} \tag{2.30}$$

The weights $\Xi(\xi, \beta, V)$ which appear in this sampling scheme are unknown *a priori* and can be determined self-consistently during the course of the simulation with the WL algorithm. To do this, we choose discrete values of ξ and β which we wish to sample and start out with a uniform guess for all $\Xi(\beta, \xi, V)$. We let the system evolve in the current state (β, ξ) via a normal Boltzmann-weighted MC scheme and attempt changes in ξ or β at fixed intervals. After such a change – irrespective of whether it has been accepted or not – the current value of $\Xi(\beta, \xi, V)$ is modified by letting $\Xi(\beta, \xi, V) \to f\Xi(\beta, \xi, V)$ where f is greater than unity. Also a histogram $H(\beta, \xi)$ is kept which serves as an indicator for when to reduce the value of f. Once we deem $H(\beta, \xi)$ to be sufficiently flat, f is reduced and the histogram reset to zero. This process is iterated until f is arbitrarily close to unity. When this is the case, we stop updating $\Xi(\beta, \mu)$ so that detailed balance is recovered. The simulation will now perform a random walk in ξ and β and we can accumulate unbiased averages of quantities such as E and X for all states (β, ξ) by means of Boltzmann MC sampling. The entire simulation is thus a combination of a thermodynamic field random walk and importance sampling Monte Carlo. In the following, this scheme will be abbreviated as CFRW for "conjugate field random walk". In contrast to the WLEXT scheme which does not directly yield statistical expectation values but rather sets of partition functions which can be reweighted to expectation values, CFRW directly determines Boltzmann-weighted averages.

After this general introduction to different kinds of flat-histogram Monte Carlo schemes, the next two chapters will show applications of these sampling methods. Chapter 3 deals with a two-dimensional decorated lattice gas model – the Hubbard model in the atomic limit – which is an ideal candidate to compare and assess different Monte Carlo schemes, because it is computationally cheap to simulate and features a rich phase diagram. Chapter 4 then applies flat-histogram sampling to the computationally more challenging task of computing phase diagrams for off-lattice fluids.

Chapter 3

Application of flat histogram sampling to the Hubbard model in the atomic limit

3.1 Introduction

The two dimensional extended Hubbard model in the atomic limit (AL-EHM) on a square lattice is an interesting candidate to study as the wealth of features present in the phase behaviour of this model system – first and second order transition lines as well as tricriticality – render it an ideal test case for investigating the usefulness of flat-histogram methods over traditional Boltzmann MC. The results presented here have been published [38] and I gratefully acknowledge Dr G. Pawlowski's contribution to this work. The AL-EHM derives from the more general extended Hubbard Hamiltonian,

$$\mathcal{H}_{EHM} = \sum_{ij\sigma} t_{ij} c^{\dagger}_{i\sigma} c_{j\sigma} + U \sum_{i} n_{i\uparrow} n_{i\downarrow} + W \sum_{ij} n_i n_j - \mu \sum_{i} n_i, \tag{3.1}$$

where t_{ij} is the hopping integral between sites i and j, $c^{\dagger}_{i\sigma}(c_{i\sigma})$ is the creation (annihilation) operator for an electron with spin $\sigma = \uparrow, \downarrow$, $n_i = n_{i\uparrow} + n_{i\downarrow}$ is the total number of electrons $\{0, \uparrow, \downarrow, \uparrow\downarrow\}$ on the i^{th} site , U represents the on-site and W the inter-site Coulomb interactions (here restricted to nearest-neighbours) and μ is the chemical potential. This Hamiltonian represents an effective model for the description of phenomena such as superconductivity, magnetism or charge density waves [39, 40].

The atomic limit is obtained by setting all $t_{ij} = 0$, which is a good approximation if the kinetic energy of the electrons is small compared to the Coulomb interaction parameters

U and W. In this limit, the electrons can be treated as classical particles as they are strongly localised at the lattice sites. This classical Hamiltonian reads

$$\mathcal{H}_{AL-EHM} = U \sum_i n_{Di} + W \sum_{ij} n_i n_j - \mu \sum_i n_i, \tag{3.2}$$

where $n_i = \{0, 1, 2\}$ and we have introduced the symbol $n_{Di} = n_{i\uparrow} n_{i\downarrow}$ to denote whether lattice site i is occupied with two electrons or not.

The AL-EHM is an adequate model for describing charge-ordering (CO) effects of electrons in strongly correlated systems [41–43]. Despite its formal simplicity, the AL-EHM shows highly nontrivial phase behaviour, including a tricritical point. Depending on the electron concentration $n = \sum_i n_i / L^2$, where L is the lateral size of the square lattice, and the Coulomb repulsions U and W, different spatial distributions of electrons on the lattice are obtained. These are described in terms of a charge-order parameter ϕ which is defined by

$$\phi = \frac{1}{2} \left| n_A - n_B \right|, \tag{3.3}$$

where n_A and n_B are the electron concentrations on sub-lattices A and B, given by a checkerboard decomposition of the bipartite lattice (as shown in the bottom right picture in Fig. 3.1). ϕ varies between zero and unity, with the latter describing the fully charge-ordered (HCO) state and the former the non-ordered (NO) state. Low-charge order (LCO) is given by $\phi = 0.5$. The relative stability of different charge-ordered states strongly depends on temperature and the ratio of on-site repulsion U and inter-site interaction zW with z being the number of nearest neighbours. Examples of different charge-ordered states are shown in Fig. 3.1. At low temperatures, quarter-filling ($n = 0.5$) gives LCO and half-filling of the lattice ($n = 1$) results in HCO, both as lattice-spanning ordered domains. Filling fractions which are not integer multiples of $1/4$ can result in striped phases containing LCO and HCO domains. Other configurations with domains that only persist over a few lattice sites are interpreted as NO states. It should be noted that, when $n \approx 1$, the charge order parameter ϕ roughly coincides with the concentration of doubly occupied lattice sites, i.e. $\phi \approx 2 \sum_i n_{Di} / L^2$. Therefore, ϕ is coupled in this regime to the Hamiltonian which implies that transitions between states of different charge-order will be accompanied by the usual signs indicating a thermodynamic phase transition, such as a peak in the heat capacity or some other response function.

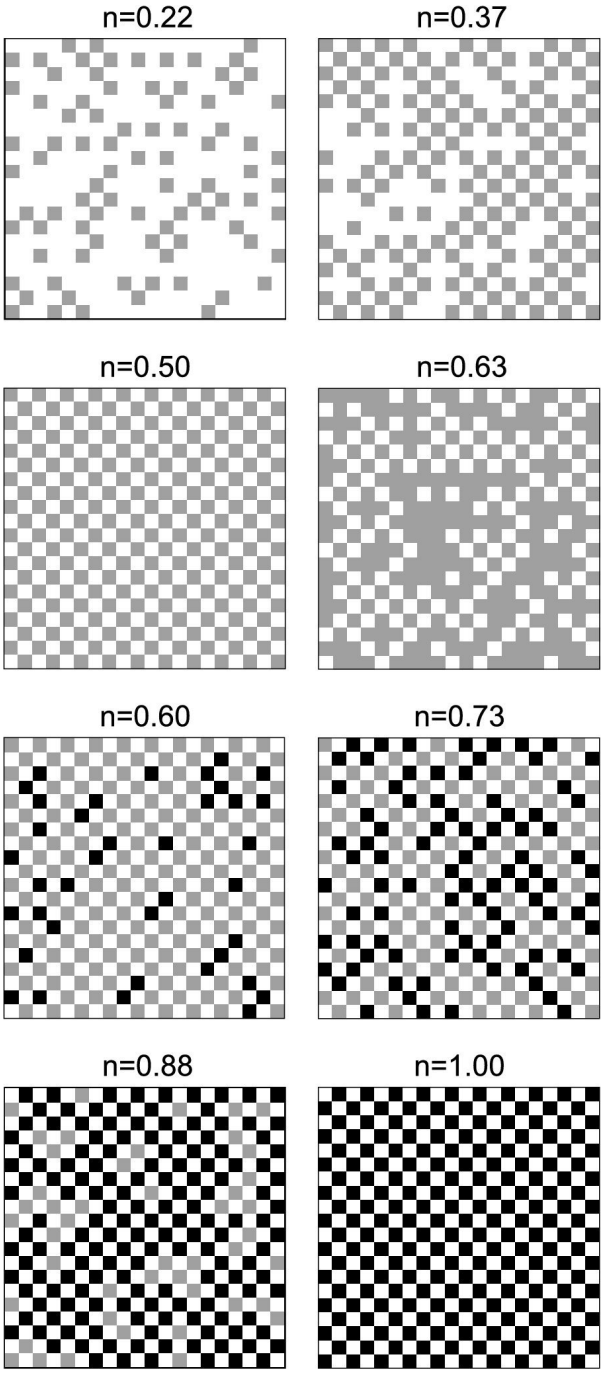

Figure 3.1: Example projections of the checkerboard states at low temperature and different values of the on-site repulsion parameter $U^* < 1$. Legend: grey squares – one electron per site, black – two electrons per site and white – empty site.

3.2 Results

For notational convenience, reduced units are employed throughout. The inter-site interaction parameter W is set to unity, the on-site Hubbard repulsion is expressed as $U^* = U/4W$, temperature is defined as $T^* = k_B T/W$ with $k_B = 1$ and all energies are

given in units of W. Unless otherwise stated, square lattices of lateral length $L = 40$ were studied. One Monte Carlo cycle (MCS) consists of L^2 MC moves.

3.2.1 Tricritical behaviour at half-filling

It has been observed before [44] that the high-temperature charge-disordered state turns into a charge ordered state as temperature is lowered. Depending on the value of U this transition is either discontinuous (first-order) or continuous (second-order). In general, the crossover between a first- and second-order phase transition regime implies the existence of a multicritical point [45] which, in this case, is a tricritical point (TCP). At temperatures below the TCP, the system shows phase coexistence between a disordered state and an ordered state which itself is split up into two symmetric phases. The disordered state is characterised by low concentration of doubly occupied sites $m = N_D/L^2$, where $N_D = \sum_i n_{D_i}$, and a low value of the charge-order parameter ϕ. The ordered state features a high concentration of doublets and a high value of ϕ and its two symmetric phases are given by the two checkerboard sublattices on either of which the doublet density is located. A quantitative order parameter which identifies the sublattice is obtained from Eq. (3.3) by removing the modulus operator: $M = (n_A - n_B)/2$; the two coexisting ordered states have $\pm M$.

As the TCP marks the crossover from a line of first-order transitions to a line of (critical) second order transitions it is possible to obtain its precise location in the following way [46]: one starts out at a sub-tricritical temperature and finds phase coexistence between the ordered and disordered states by tuning U such that the probability distribution $p(m)$ is bimodal with equal areas under both peaks. The Binder cumulant ratio [47],

$$U_L = 1 - \frac{\left\langle (m - \langle m \rangle)^4 \right\rangle}{3 \left\langle (m - \langle m \rangle)^2 \right\rangle^2} \tag{3.4}$$

is then calculated and this procedure is repeated for a range of different temperatures and system sizes L. Due to the scale invariance of U_L at criticality, all curves of U_L when plotted against the temperature will intersect at a single temperature which is then taken as the estimate of the tricritical temperature. However, the specific value of U_L is *not* a universal quantity as the model studied is constrained to a fixed number of lattice vacancies, which influences the boundary conditions. A detailed discussion of this point can be found in Ref. [48].

In order to begin the above procedure it is first necessary to obtain a rough estimate for the parameter range of U and T in which the probability distribution $p(m)$ starts to

appear bimodal. We obtained $p(m)$ through WLEXT simulations which sample all possible numbers of doublets N_D at constant temperature and fixed electron concentration (c.f. Section 2.2.3). The MC acceptance rule for this sampling scheme reads

$$acc(N_{Do} \to N_{Dn}) = \min\left\{1, \frac{\exp[-\beta E(N_{Dn})]}{\exp[-\beta E(N_{Do})]} \frac{Q(N_{Do})}{Q(N_{Dn})}\right\} \tag{3.5}$$

and the converged simulation provides the canonical partition functions $Q(N_D)$. As the conjugate thermodynamic field for the number of doublets is the Hubbard on-site repulsion U, the probability distribution for the order parameter m is directly given by $p(m) \propto Q(N_D)\exp(-\beta U N_D)$.

These simulations were run with convergence parameters $f_{\text{initial}} = \exp(1)$, $\ln(f_{\text{final}}) = 10^{-8}$ and f was reduced as soon as every possible number of doublets that the system can attain had been visited at least 1000 times. After the onset of bimodality in $p(m)$ had been conveniently located this way we performed a single long Metropolis MC simulation at this state point for system sizes $L = \{24, 32, 48, 64\}$ and used the histogram reweighting technique [49] to calculate U_L for different temperatures with U chosen subject to the constraint that $p(m)$ satisfies the equal-area rule. The resulting plot of U_L against temperature is shown in Fig. 3.2: all four curves for different system sizes intersect to within numerical uncertainty at $T^*_{\text{TCP}} = 0.6080(4)$ with the uncertainty in the last decimal place given by the uncertainty in the average of the crossing points.

In order to further verify the TCP in this system we invoke the universality of the ordering parameter distribution $p(M)$. Because microscopic details are irrelevant at criticality, the measured form of $p(M)$ will coincide with other model systems featuring a TCP, provided that the distributions are scaled to unit norm and variance. To this end we employ a measured $p(M)$ for the two-dimensional Blume-Capel model as a reference (courtesy of N. B. Wilding [46]) and adjust T and U for each system size L such that $p(M)$ collapses on the reference distribution. Results are shown in Fig. 3.3 where the agreement is clearly excellent. This procedure yields the apparent, system-size dependent values of T_{TCP} and U_{TCP} for each value of L, which is to be contrasted with the Binder cumulant intersection method that yields an estimate for the bulk tricritical temperature. An estimate for the $L = \infty$ TCP based on the apparent finite-size values is obtained from the finite-size scaling relation [49] $T_{\text{TCP}}(L) = T_{\text{TCP}}(L = \infty) + \lambda L^{-1/\nu_t}$ where λ is a model dependent constant and ν_t is the tricritical scaling exponent, which is a universal quantity. To this end, we use $\nu_t = 0.56$ from Ref. [50]. Plots of $T_{\text{TCP}}(L)$ and $U_{\text{TCP}}(L)$ against L^{-1/ν_t} are shown in Fig. 3.4. Extrapolation of these data points to $L = \infty$ yields $T^*_{\text{TCP}} = 0.6082(3)$ which agrees with the Binder cumulant estimate to within error, and $U^*_{\text{TCP}} = 0.7720(2)$.

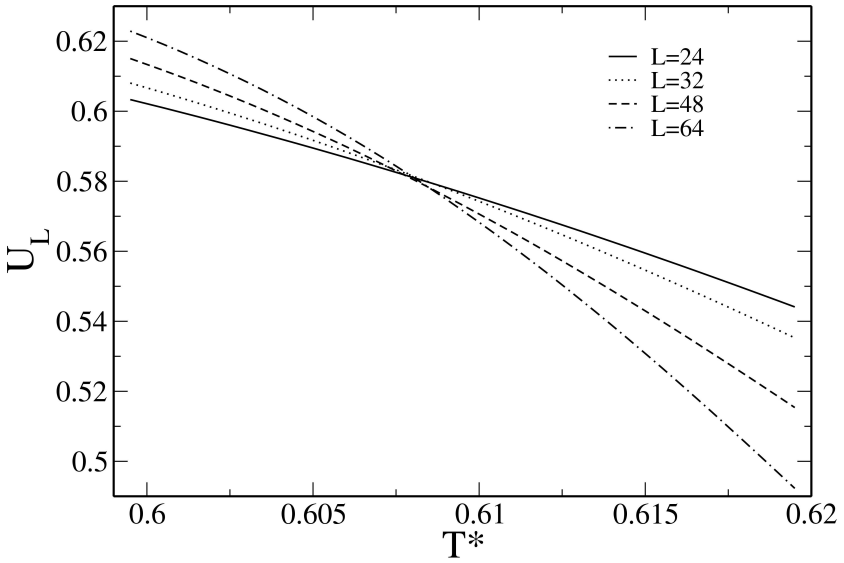

Figure 3.2: Binder cumulant ratio U_L in the vicinity of the tricritical point at half-filling for different lattice sizes L.

It is interesting to ask what happens to the lines of phase transitions and the TCP at electron concentrations different from half-filling. We found that a perfect match of $p(M)$ onto the tricritical reference distribution is only possible at half-filling and the deviation between the measured distribution and the reference becomes larger the further the density deviates from half filling. This indicates that a TCP exists only at half-filling but does not rule out the existence of a different type of multicritical point such as a critical end point at other electron concentrations. While it was not possible to identify the exact nature of these multicritical points using our methodological apparatus, we note that the onset of a bimodal distribution in $p(m)$ shifts to lower temperatures as the density is reduced and no bimodal distribution could be observed for $n < 0.8$, which can be explained in terms of a vanishing interfacial tension between the two phases of different charge order: a first-order transition can only occur if the coexisting phases are separated by an interface which constitutes a free energy barrier that stabilises the phases against mixing with each other. By changing the electron concentration to values beyond $n = 1$ one introduces single occupied sites or holes in the lattice which hinder the formation of an interface and thus promote mixing, resulting in a continuous transition between states of different charge order as U is varied. We conclude this analysis by noting that a line of multicritical points exists in the n–T plane which extends from an upper tricritical temperature at $n = 1$ to a vanishing multicritical temperature at $n \approx 0.8$. Therefore, first-order phase transitions between states of different charge order can only be observed at temperatures and densities below this line [*cf.* the global phase diagram Fig. (3.11)].

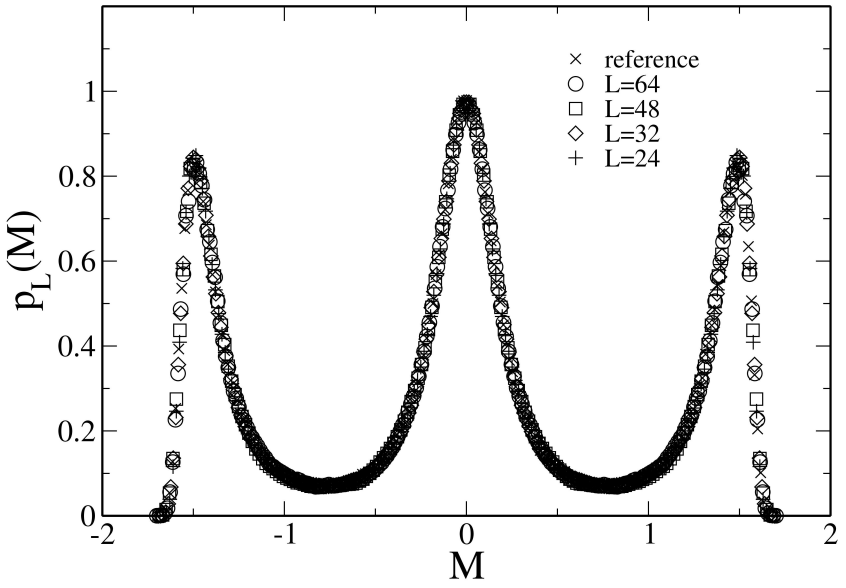

Figure 3.3: Tricritical ordering parameter distribution $p(M)$ at half-filling for different lattice sizes and the reference distribution for the 2D Blume-Capel model. All distributions are scaled to unit norm and variance.

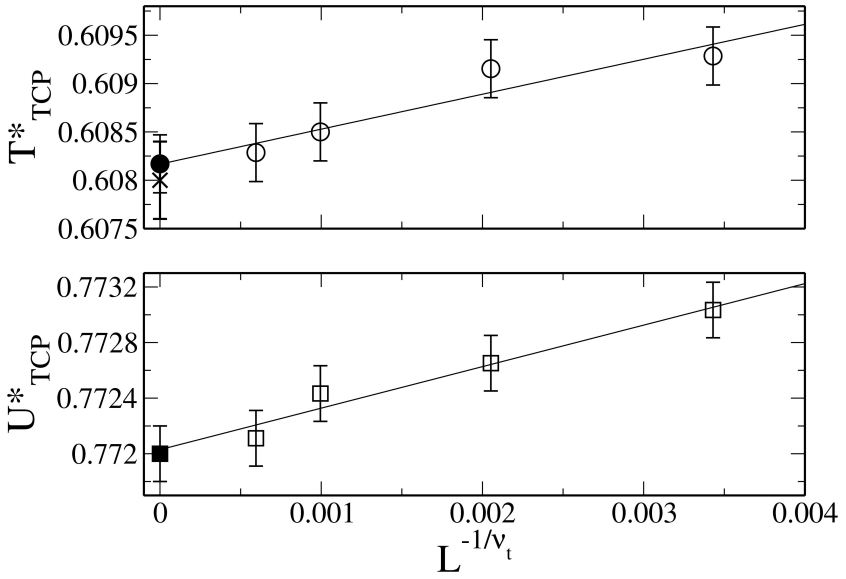

Figure 3.4: Upper plot: Finite size scaling plot of the apparent tricritical temperature at half-filling for different lattice sizes L. Open circles denote simulation results and the straight line represents a least-squares fit to these data points which is used to extrapolate to $L = \infty$ yielding $T^*_{\mathrm{TCP}} = 0.6082(3)$. The cross marks the estimate for $T^*_{\mathrm{TCP}} = 0.6080(4)$ obtained from the Binder cumulant intersection method (see text). Lower plot: Open squares denote the apparent value of U^*_{TCP} at tricriticality for different system sizes. Extrapolation to $L = \infty$ using a linear least-squares fit yields $U^*_{\mathrm{TCP}} = 0.7720(2)$, shown as a solid square. Errorbars show the estimated uncertainty in the data points as obtained from the standard deviation of the average from four independent runs.

3.2.2 Global order parameter distribution

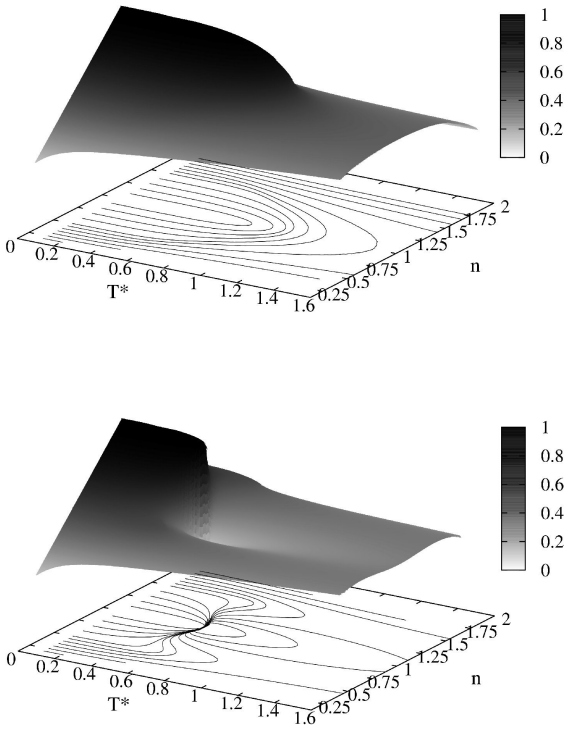

Figure 3.5: Charge-order parameter ϕ as a function of density and temperature for $U^* = 0.5$ (top) and $U^* = 0.8$ (bottom). Projected solid lines indicate lines of constant charge-order parameter.

The charge order parameter as function of temperature and density has been obtained using the CFRW sampling scheme [Eq. (2.30)] for the range $\mu^* = [-1.0..12.0]$, $T^* = [0.1..1.6]$ with discretisation $\Delta\mu^* = 0.1$ and $\Delta T^* = 0.01$. Attempts to change either μ or T were performed once every 2 MCS. The WL convergence procedure of the weights $\Xi(\mu, \beta)$ was initiated with $f_{\text{initial}} = \exp(10)$ and f was reduced according to $f = \sqrt{f}$ once every state (μ, β) had been visited a minimum of 100 times. The weights were converged down to $\ln(f_{\text{final}}) = 10^{-6}$ before a histogram of ϕ was accumulated for each thermodynamic state point (μ, β) during a production run of length 10^9 MCS. Results for the charge-order parameter in the T–n plane are shown in Fig. 3.5 for $U^* = 0.5$ and 0.8. These selected cases of the on-site Hubbard repulsion behave quite differently: For $U^* = 0.5$ no abrupt transitions between different charge orders can be seen, while for $U^* = 0.8$ a step-like change of ϕ along the half-filling line can be observed. As discussed above, this agrees with the value of the critical on-site repulsion $U^*_{\text{TCP}} = 0.7720(2)$ below which the transition occurs continuously for all densities.

3.2.3 The density of states and thermodynamic quantities

The full DOS for $U^* = 0.8$ and $U^* = 0.5$ has been obtained for a lattice size $L = 20$. While this approach allows the calculation of thermodynamic quantities at arbitrary state points, it was only possible to converge the WLEXT algorithm for this two-dimensional sampling problem [*cf.* Eq. (2.16)] for small systems. We note that, compared to existing WLEXT simulations of both E and the magnetisation M for the Ising model [51] on square lattices, the accessible configuration space of our Hamiltonian is much larger. For a given lattice size L, one has 2^L more states in the present model with four lattice-site states than for the Ising model. In order to obtain the DOS with high accuracy we resorted to a tighter convergence criterion compared to that employed above: the ratio of any entry in the histogram of visited states was required to be within a 15% interval of the mean value of the histogram. f_{initial} was set to exp(1) and the simulation was stopped at $\ln(f_{\text{final}}) = 10^{-8}$. The total run time required was on the order of 10^{10} MCS which translates into 10 CPU days on a 2.0GHz processor. Fig. 3.6 shows the DOS surface which is spanned over the trivial points 0, 1/4, 1/2, 3/4 and full filling of the lattice. The corresponding entropy $s = S/L^2$ in the n–T^* plane is shown in Fig. 3.7. Again, the trivial commensurate lattice fillings can be seen but also a region with a step-like drop at the half-filling line is identified. Because $\left(\frac{\partial s}{\partial T}\right)_V = c_V/T$ this is indicative of a discontinuous transition involving latent heat. As discussed above, the DOS contains all information necessary to calculate all thermodynamic potentials. For

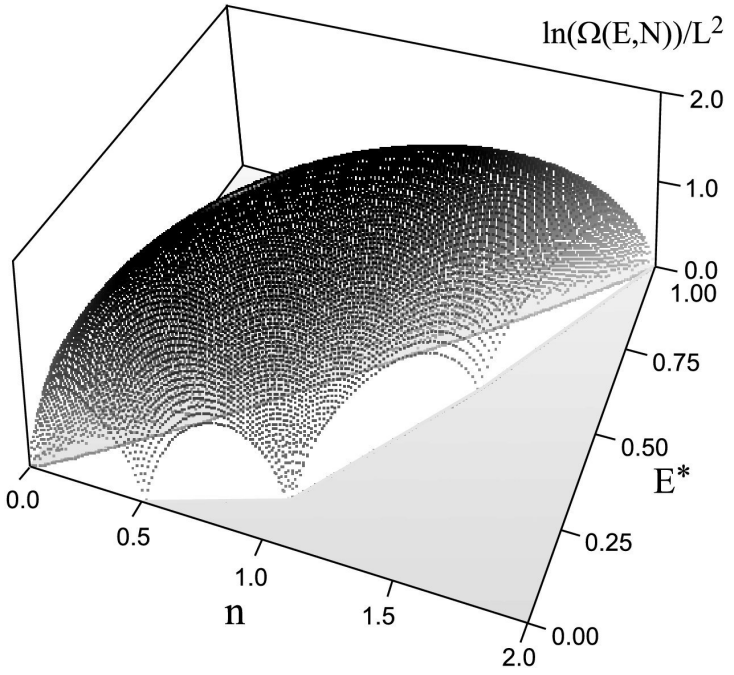

Figure 3.6: Density-of-states for $U^* = 0.8$ on a logarithmic scale. $E^* = E/E_{\max}$ denotes the fractional energy with respect to the maximum energy possible for this lattice size.

a fixed number of electrons, we have the internal energy

$$\langle E_N(T)\rangle = \frac{\sum\limits_E E\Omega(E,N)\exp(-\beta E)}{\sum\limits_E \Omega(E,N)\exp(-\beta E)}, \tag{3.6}$$

the free energy

$$\langle F_N(T)\rangle = -k_B T \ln\left[\sum_E \Omega(E,N)\exp(-\beta E)\right], \tag{3.7}$$

and the entropy

$$\langle S_N(T)\rangle = \frac{\langle E_N(T)\rangle - \langle F_N(T)\rangle}{T}. \tag{3.8}$$

Fig. 3.8 shows these thermodynamic quantities for $U^* = 0.5$ and 0.8 at $n = 0.45$ and 0.95. At the lower density considered here, $n = 0.45$, neither system attains any significant number of doubly occupied lattice sites, simply because there is enough room on the lattice to accommodate all electrons without any nearest neighbours. Therefore, their thermodynamic behaviour must be largely independent of U as the Hubbard on-site repulsion only makes a negligible contribution the to system's energy. The upper parts of Figs. 3.8 indeed confirm this reasoning with a small peak in c_V at $T^* \simeq 0.6$ for both systems. This peak indicates a temperature-driven phase transition between the LCO at low T and the completely disordered NO state at high T. In contrast to the low-density behaviour, the thermodynamic quantities at $n = 0.95$ depend strongly on U. Here, we have the situation that nearest-neighbour interactions compete with the

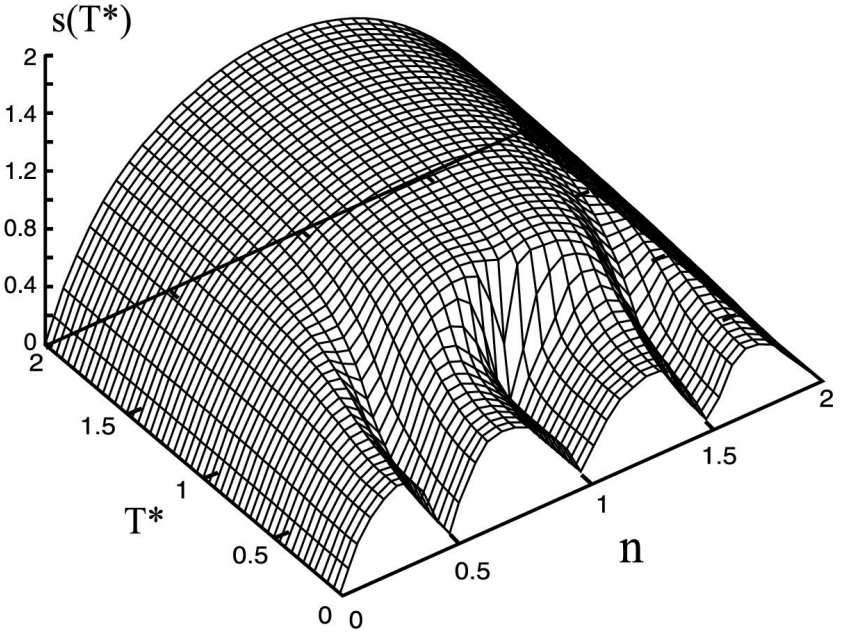

Figure 3.7: Entropy per lattice site for $U^* = 0.8$ in the n–T^* plane. The step along the $n = 1$ line indicates the region of discontinuous phase transition.

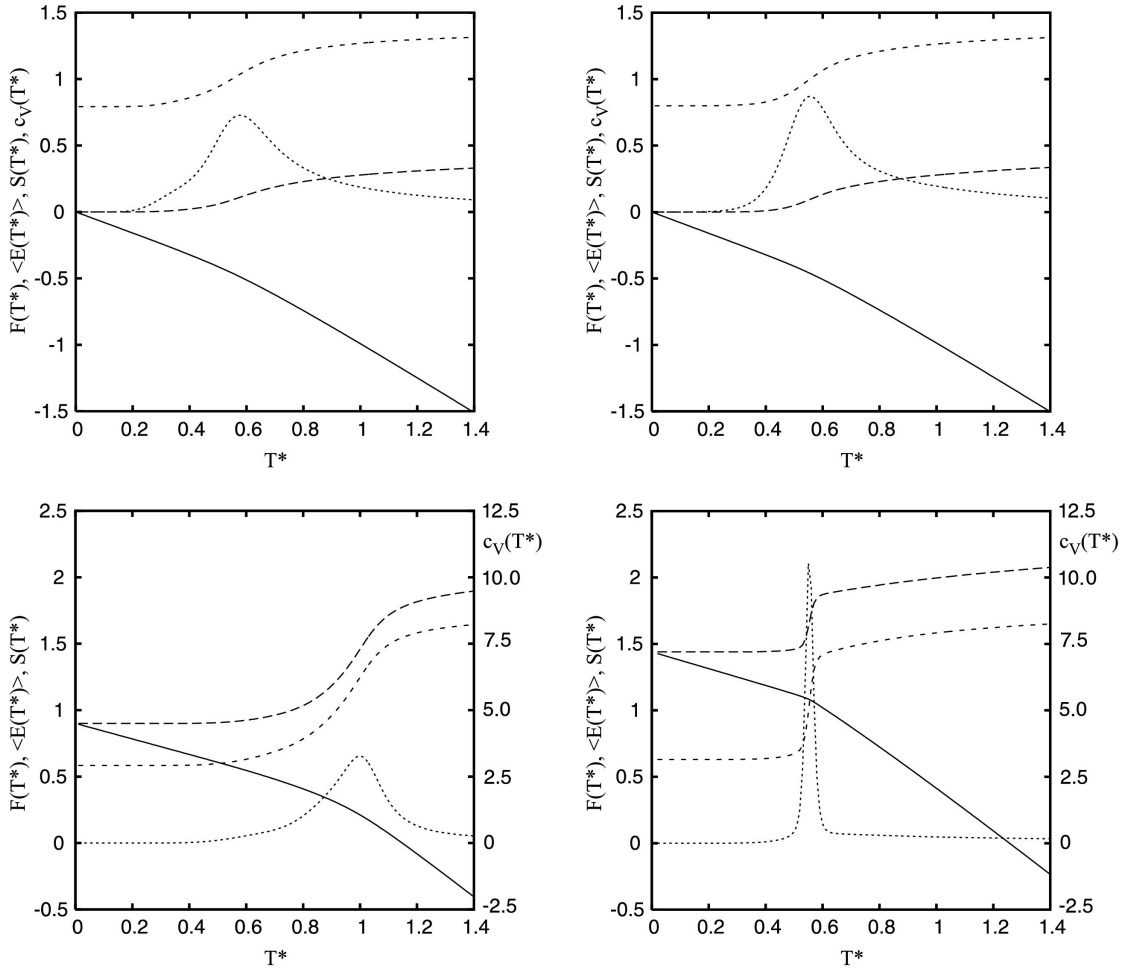

Figure 3.8: Thermodynamic quantities per lattice site for $U^* = 0.5$ (left part of the figure) and $U^* = 0.8$ (right part): Free energy F – solid line, internal energy E – long dashed line, entropy S – short dashed line and heat capacity c_V – dotted line. The upper graphs are for $n = 0.45$ and the lower for $n = 0.95$.

Hubbard on-site interaction and, in the case of $U^* = 0.8$, we find a strong first-order transition between HCO and NO states indicated by a step-like change of the entropy and a well-defined peak in the heat capacity at $T^* \simeq 0.54$. For $U^* = 0.5$ this peak is much broader and, owing to the system's dependence on U, it is also located at a different temperature $T^* \simeq 1.00$.

3.2.4 Phase diagrams

Traversal of the boundary between two phases is usually accompanied by an abrupt change of a suitably defined order parameter and a peak in the susceptibility associated with this order parameter. We have used the latter signal to plot the phase diagram in the n–T^* plane for $U^* = 0.5$ and 0.8. Phase boundaries were identified

using canonical heat capacities $c_V = \frac{\langle E^2\rangle - \langle E\rangle^2}{k_B T^2 N}$ and charge order parameter susceptibilities $\chi_V = \frac{\langle \phi^2\rangle - \langle \phi\rangle^2}{N}$ from the CFRW sampling scheme at fixed density but varying temperature [i.e., a one-dimensional version of the sampling scheme Eq. (2.30) which samples only a range of temperatures]. Discretisation of the temperature range was set to $\Delta T^* = 5 \times 10^{-3}$ and the WL convergence parameters used were $f_{\text{initial}} = \exp(1)$, and $\ln(f_{\text{final}}) = 10^{-10}$. f was reduced as above once every discrete temperature had been visited 1000 times. A production run of length 10^7 MCS was appended after the WL procedure was converged. Histograms of E and ϕ were kept for the subsequent calculation of the canonical heat capacity c_V and the susceptibility of the charge order parameter χ_V. Complementary to this the isothermal compressibility was computed at fixed temperature from a WLEXT simulation [*cf.* sampling scheme Eq. (2.21)] which samples all electron concentrations at fixed temperature in a single simulation. Convergence parameters were as above for the canonical CFRW simulations. Using the converged $Q(N)$ obtained from this simulation, the first and second moments of the electron number distribution were computed,

$$\begin{aligned} \langle N\rangle &= \frac{\sum\limits_N NQ(N)\exp(\beta\mu N)}{\sum\limits_N Q(N)\exp(\beta\mu N)} \\ \langle N^2\rangle &= \frac{\sum\limits_N N^2Q(N)\exp(\beta\mu N)}{\sum\limits_N Q(N)\exp(\beta\mu N)}, \end{aligned} \tag{3.9}$$

which then afforded the isothermal compressibility $\kappa_T = \frac{\beta}{\rho}\frac{\langle N^2\rangle - \langle N\rangle^2}{\langle N\rangle}$.

Both phase diagrams are symmetric with respect to mirroring along the half-filling line due to the particle-hole symmetry of the Hamiltonian Eq. (3.2). Fig. 3.9 shows the results for the case $U^* = 0.5$. We obtain second-order transitions between NO and CO. Within the CO phase no indication for an abrupt change of the density or the charge-order parameter was found. The situation for $U^* = 0.8$, shown in Fig.3.10 is very different: a new line of peaks in κ_T emerges in the CO phase separating it into LCO and HCO regimes. The two sampling schemes used here – CFRW at constant density and WLEXT sampling at a given temperature – constitute already a great improvement over normal Boltzmann MC sampling because they enable us to study an entire temperature or electron concentration range in a single simulation. They are well suited to determine precisely the location of phase boundaries and require only very modest CPU resources. Nevertheless, we still require several of these simulations to construct an entire phase diagram. This is inconvenient if one wishes to obtain the phase diagram not only as a function of n and T but also at different values of U. Ideally, one would perform one large simulation which samples the joint density of states $\Omega(N, E, U)$, from which the entire

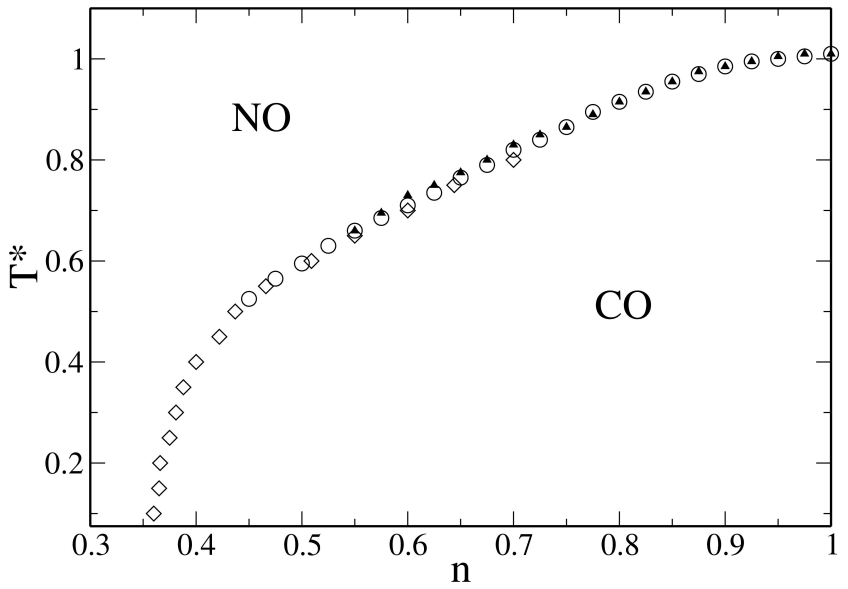

Figure 3.9: Phase diagram in the n–T^* plane for $U^* = 0.5$. Phase boundaries have been obtained from peaks in c_V (circles), χ_V (triangles) and κ_T (diamonds).

phase diagram in the space of density, temperature, and Hubbard interactions could be determined. In practice this approach is hardly feasibly due to the very long time it would require for the three-dimensional DOS to converge, even for the smallest systems. As noted above, it is already difficult to converge the two-dimensional DOS $\Omega(N, E)$ for medium sized systems. If accuracy and finite-size effects are not of great importance one can resort to the compromise of running multiple, very small WL simulations which sample the two-dimensional DOS for specified values of U. This approach is feasible in practice and substantially reduces the number of simulations required to obtain a global phase diagram. Fig. 3.11 shows such a global phase diagram obtained for very small systems and loose WL convergence parameters ($L = 8$, $\ln(f_{\text{final}}) = 10^{-5}$).

3.3 Discussion

The development of flat-histogram sampling techniques in general and especially the robust and easy to implement algorithm of Wang and Landau, which allows for the iterative determination of the biasing weights needed to accumulate a flat histogram, have greatly eased the simulation efforts needed to obtain phase diagrams. We have employed different sampling strategies which either uniformly sample mechanical variables such as energy, or which perform a random walk in the corresponding conjugate thermodynamic field, e.g., temperature. Depending on the actual system to be studied one might prefer one approach over the other. The advantage of the WLEXT scheme which samples extensive variables is that ensemble averages can be calculated at any

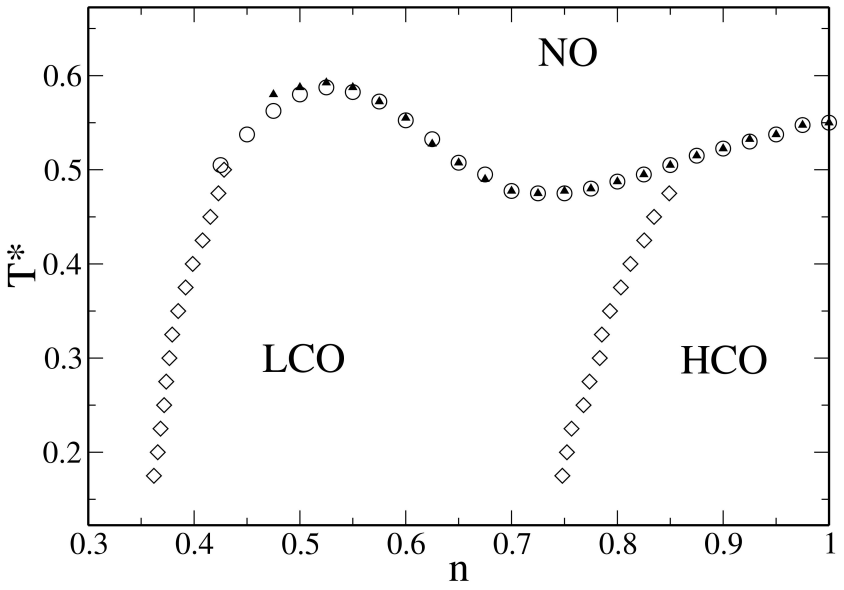

Figure 3.10: Phase diagram in the n–T^* plane for $U^* = 0.8$. Symbols are as for Fig 3.9.

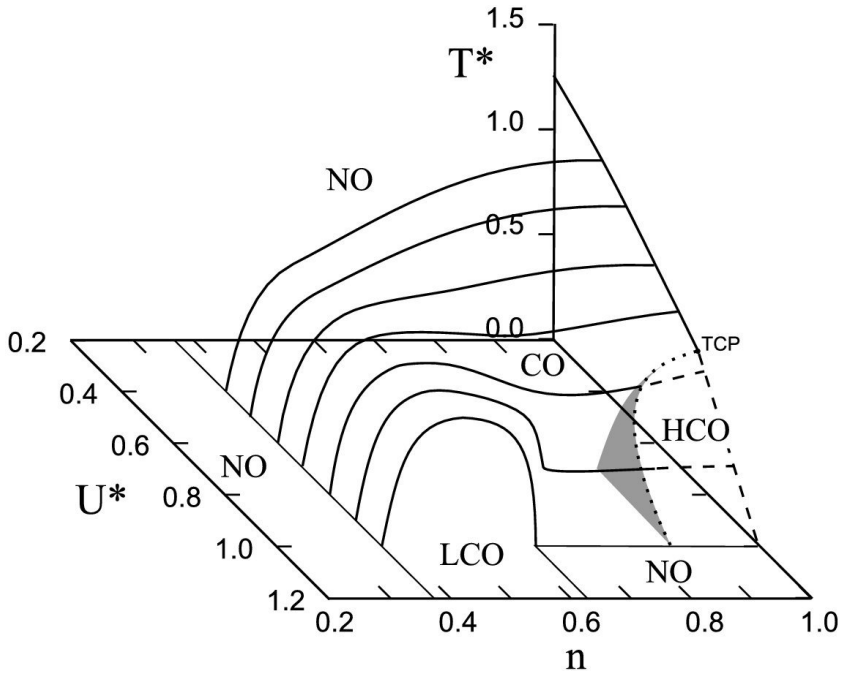

Figure 3.11: Global phase diagram. Solid- and dashed-lines indicate the second- and first-order transitions respectively, whereas the multicritical points are denoted by a dotted line. The grey area shows the transition LCO – HCO as indicated by peaks in κ_T.

thermodynamic state point by simple reweighting. The CFRW scheme on the other hand seems to converge faster but is limited in the chosen discretisation width of the thermodynamic fields to be sampled. It has been noted before [26] that the WL algorithm asymptotically reaches a level of uncertainty which does not decrease if the simulation is continued. In comparison, the CFRW scheme employs normal Boltzmann MC sampling for each state point with errors inversely proportional to the square-root of the run length. For both algorithms considered, it is possible to sample multiple variables in a single simulation. However, for the WLEXT scheme it has been found [33, 52] that in practice this is only possible for small systems and it is much more efficient to concentrate the sampling effort on a single variable to be uniformly sampled and to run multiple simulations. The CFRW scheme appears to suffer less from this drawback but, as noted beforehand, it produces less information because it is limited to a certain range of discrete values for the thermodynamic field variables. On the other hand, there are many cases where only a certain range of e.g., temperatures is of interest so that CFRW allows one to focus on the relevant range, whereas normal WL sampling will need to sample all energies the system can attain because it cannot be determined in advance which of these states will have a high Boltzmann weight. This advantage of CFRW is reflected by our simulation timings where it required only a few hours of CPU time to sample a wide range of temperatures and chemical potentials simultaneously; it required almost two orders of magnitude longer simulation times to converge the joint DOS using the WLEXT algorithm for a system of only half the size.

Chapter 4

Application of flat histogram sampling to phase transitions in fluids

4.1 Introduction

The phase behaviour of fluids is of general importance in many fields of science and engineering. Monte Carlo (MC) methods are particularly well suited for simulating phase transitions in simple models [53]. While standard simulation methods are often sufficient for sampling coexisting phases with comparable and low densities, they cannot be used to probe directly the phase coexistence region well below the critical temperature where the transition is strong, i.e., where there is a large difference in order parameter between the coexisting phases. The problem arises mainly from the large free-energy barrier separating the coexisting phases, which is associated with forming an interface within the simulation cell. Many new algorithms have been devised to overcome or circumvent this barrier. Multicanonical sampling [23] biases the simulation such that the free energy barrier is cancelled out, allowing uniform sampling of the coexisting phases and all intermediate states. In order to sample an order parameter uniformly, one needs to know the weights which yield a flat histogram. As has been shown in Chapter 2, these weights are directly related to partition functions and thus to the free energy as a function of the order parameter, which of course is unknown *a priori*. However, iterative schemes can be employed to map out the free energy profile and build up the biasing distribution during the course of a simulation. Here, the Wang-Landau (WL) algorithm [25] is employed in order to facilitate flat histogram sampling of the number density ρ, which is the appropriate order parameter for vapour-liquid phase transitions

(at least away from the critical point). This is accomplished via the WLEXT sampling scheme devised in Chapter 2 and working either in the isothermal-isobaric ensemble and performing changes in the volume V [NpT-WLEXT scheme, see Eq. (2.23)], or in the grand-canonical ensemble by changing the number of particles N [GC-WLEXT scheme, see Eq. (2.21)].

This chapter compares the accuracy of the NpT-WLEXT and GC-WLEXT schemes against high-quality data already available for the Lennard-Jones fluid. The broad applicability of these sampling schemes is then tested by attacking some 'difficult' transitions, namely the vapour-liquid transitions of charged soft spheres and of the strongly dipolar Stockmayer fluid, and the isotropic-nematic transition of Gay-Berne mesogens. Fig. 4.1 gives an overview of the models studied in this chapter. The results presented here have been published in [33] and I gratefully acknowledge Dr P. J. Camp's contribution to this work.

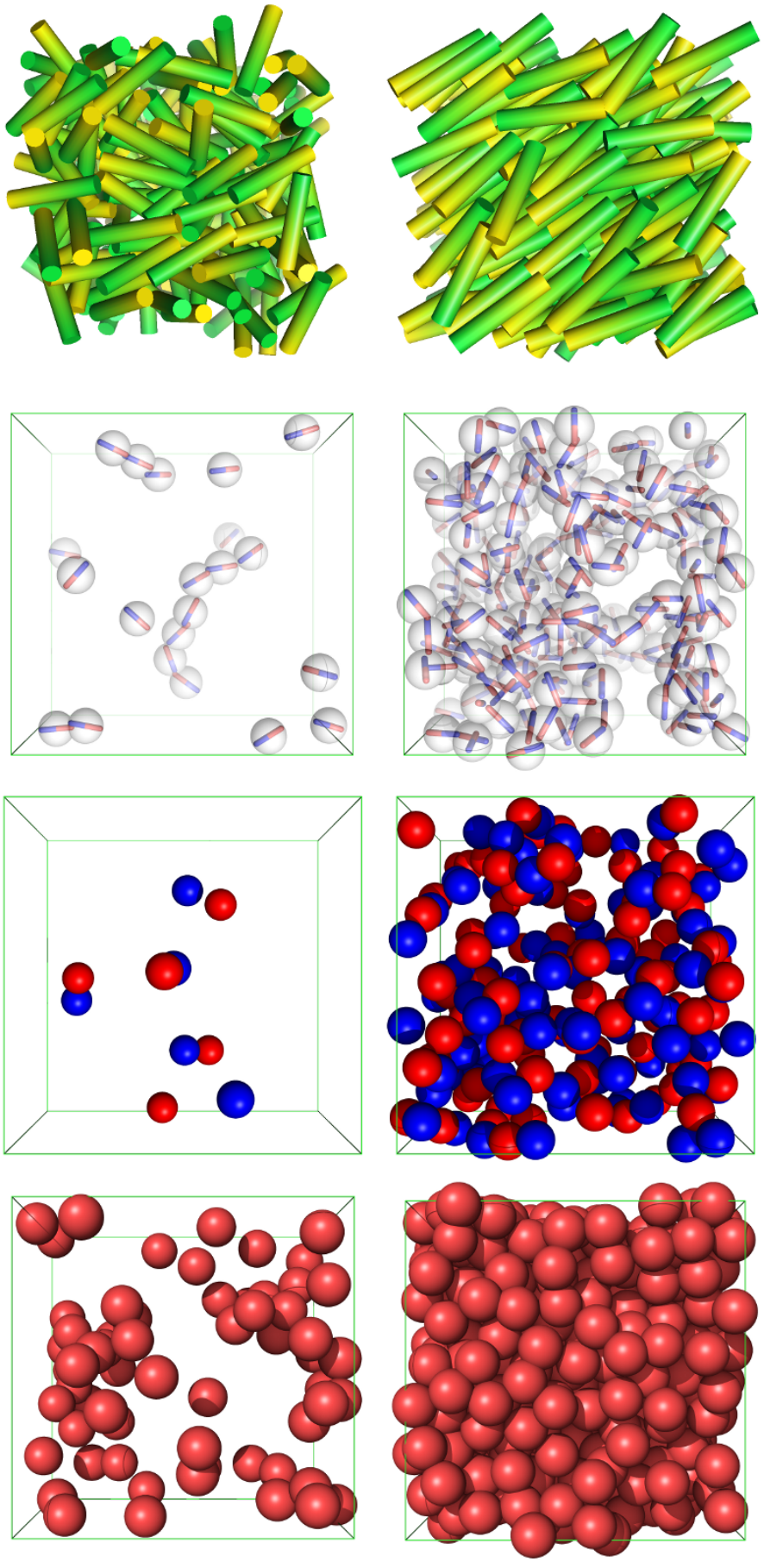

Figure 4.1: Configurations typical of coexisting phases. From left to right: Lennard-Jones particles, charged soft spheres (blue cation, red anion), and Stockmayer particles (magnetic dipole shown as a blue/red stick embedded in a partially transparent sphere indicating the LJ repulsive core) with the vapour state shown above the liquid state. On the far right: Gay-Berne mesogens in the isotropic phase shown above the coexisting nematic phase.

4.2 Results

4.2.1 Lennard-Jones fluid

This example serves to demonstrate the correctness of the hybrid schemes represented by Eq. (2.21) (GC-WLEXT) and Eq. (2.23) (NpT-WLEXT) which sample a uniform number density distribution at fixed temperature in the grand canonical and isothermal-isobaric ensemble, respectively. In order to assess the performance of the GC-WLEXT and NpT-WLEXT approaches, we compare results against existing high-quality $GCMC$ transition matrix (TM) data [54, 55] for the Lennard-Jones potential

$$u(r_{ij}) = 4\epsilon \left[\left(\frac{\sigma}{r_{ij}} \right)^{12} - \left(\frac{\sigma}{r_{ij}} \right)^{6} \right] \tag{4.1}$$

truncated at $r_{ij} = 3\sigma$. Following Refs. [54] and [55], GC-WLEXT simulations were run at exactly the same system size, i.e., $V = 512\sigma^3$, and with the usual long range corrections applied [18]. For the NpT-WLEXT calculations we chose $N = 216$. The density ranges sampled during the WL simulations were as follows: with GC-WLEXT, $0 \leq N \leq 454$ corresponding to $0 \leq \rho^* = N\sigma^3/V \leq 0.89$; with NpT-WLEXT, $10^{-3} \leq \rho^* \leq 0.9$. While there is a natural discretisation of $Q(N,V,T)$ if the particle number is varied (as in GC-WLEXT), this is not the case for the continuous variable V (as in NpT-WLEXT). Therefore an arbitrary binning scheme has to be employed which is fine enough to capture the curvature of $Q(N,V,T)$, but does not use too many bins because otherwise computational efficiency deteriorates. We decided to use 100 histogram bins with a uniform spacing in $\ln V$, and in the NpT-WLEXT update scheme we performed changes in $\ln V$ with a maximum stepsize of twice the bin width. For this model and the other simulations reported below, f started from $\ln f = 1$ and a run was considered converged when it reached $\ln f = 10^{-8}$ for GC-WLEXT and $\ln f = 10^{-5}$ for NpT-WLEXT. In order to monitor convergence for each cycle of fixed f, a histogram of visited number density bins $H(\rho)$ was maintained and f was reduced according to the rule $f = \sqrt{f}$ as soon as all entries in H had been visited at least 1000 times for GC-WLEXT and 500 times for NpT-WLEXT. Maximum displacements for single-particle moves were adjusted to give acceptance ratios of 50%. The time required to converge the simulations was 4h and 12h for GC-WLEXT and NpT-WLEXT, respectively. All simulation times reported here are for Intel Xeon processors clocked at 2.4GHz.

In the case of GC-WLEXT, coexisting vapour and liquid densities were obtained from the converged estimates of $Q(N,V,T)$ by integrating the low and high density branches in the particle number probability probability distribution $P(N)$, with the chemical potential adjusted such that both branches have equal area. If the boundary so determined is

at $N = N_b$, then the average densities in the vapour ($N < N_b$) and liquid ($N > N_b$) branches are given by,

$$\begin{aligned} \langle \rho_{\mathrm{vap}} \rangle &= \frac{\sum_{N<N_b} (N/V) Q(N,V,T) e^{\beta\mu N}}{\sum_{N<N_b} Q(N,V,T) e^{\beta\mu N}} \\ \langle \rho_{\mathrm{liq}} \rangle &= \frac{\sum_{N>N_b} (N/V) Q(N,V,T) e^{\beta\mu N}}{\sum_{N>N_b} Q(N,V,T) e^{\beta\mu N}}. \end{aligned} \tag{4.2}$$

The boundary N_b between vapour and liquid peaks was identified with the value of N where $P(N)$ is at a minimum. In the case of NpT-WLEXT, the procedure is completely analogous but with N replaced by V, and sums replaced by integrals:

$$\begin{aligned} \langle \rho_{\mathrm{vap}} \rangle &= \frac{\int_{V_b}^{\infty} (N/V) Q(N,V,T) e^{-\beta PV} \mathrm{d}V}{\int_{V_b}^{\infty} Q(N,V,T) e^{-\beta PV} \mathrm{d}V} \\ \langle \rho_{\mathrm{liq}} \rangle &= \frac{\int_{0}^{V_b} (N/V) Q(N,V,T) e^{-\beta PV} \mathrm{d}V}{\int_{0}^{V_b} Q(N,V,T) e^{-\beta PV} \mathrm{d}V}. \end{aligned} \tag{4.3}$$

Coexistence results are shown in Fig. 4.2, with a maximum deviation between WLEXT and TM data [54, 55] of 1.0% and an average deviation of 0.4%. The good agreement of the coexistence densities is also reflected in rough estimates of the critical parameters, obtained by fitting the universal equation

$$\rho_{\pm} = \rho_c + At \pm Bt^{\beta} \tag{4.4}$$

where $t = |T - T_c|/T_c$ and $\beta = 0.3265$ is the three-dimensional Ising order-parameter exponent [56]. The apparent critical temperatures and densities are $T_c^* = k_B T_c/\epsilon = 1.300(4)$ and $\rho_c^* = 0.314(1)$ from GC-WLEXT, and $T_c^* = 1.290(6)$ and $\rho_c^* = 0.313(4)$ from NpT-WLEXT. These are to be compared with fits to TM data [54, 55]; $T_c^* = 1.2950(6)$ and $\rho_c^* = 0.3125(8)$. Estimates of the uncertainties in the last decimal places are given in brackets; these were taken from the fitting errors and are therefore underestimates compared to the true statistical error.

4.2.2 Charged soft spheres

While there have been a number of publications on the WL simulation of phase coexistence in fluids, all of these have been applied to simple systems like the Lennard-Jones potential. In this study we aim to show the general applicability of WL sampling by applying the method to complex fluids. The restricted primitive model (RPM) is one such complex fluid. It consists of an equimolar mixture of hard spheres with charges $\pm q$ and equal diameters σ_{HS}. The vapour-phase structure is characterised by the strong association of oppositely charged ions to form dumbbells [57, 58]. After a significant

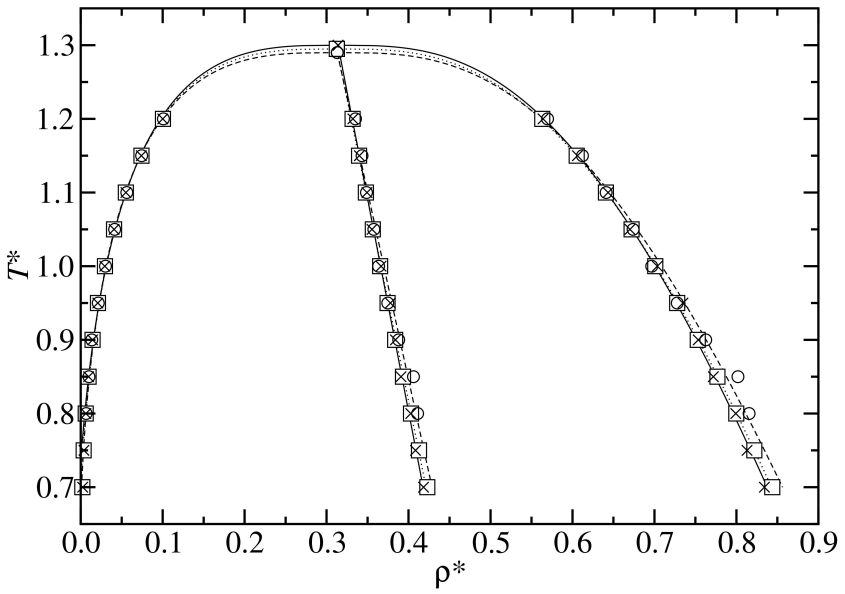

Figure 4.2: Vapour-liquid coexistence envelopes for the Lennard-Jones fluid from simulations (points) and fits to the simulation points using Eq. (4.4) (lines): transition matrix MC [54, 55] – squares and dotted lines; *GC*-WLEXT – crosses and solid lines; NpT-WLEXT – circles and dashed lines.

number of intensive simulation studies, the location of the critical point and the universality class (Ising) have been established unambiguously [13, 59]. Such systems are much harder to simulate than the Lennard-Jones fluid because insertions/and deletions have to be effected using pairs of oppositely charged particles in order to maintain charge neutrality; moreover, the favoured separation and orientation of each inserted ion pair has to be selected in a biased fashion [60]. Here we have chosen to use a soft repulsive potential as this facilitates simulations with volume scaling moves as in NpT-WLEXT: if a hard core was used, even an infinitesimal overlap after a volume contraction move would lead to rejection. The interaction potential of the 'charged soft spheres' (CSSs) is defined by

$$u(r_{ij}) = 4\epsilon \left(\frac{\sigma}{r_{ij}}\right)^{12} + \frac{q_i q_j}{D r_{ij}} \tag{4.5}$$

where $D = 4\pi\epsilon_0$. Long-range interactions were treated with the Ewald sum and conducting boundary conditions [18]. The soft repulsive potential was cut at $r = 2.5\sigma$. In order to compare our results for CSSs with the data available for the RPM, we fixed the reduced charge at $q^* = \sqrt{q^2/D\sigma\epsilon} = \sqrt{48}$, which sets the minimum in the cation-anion potential at $r = \sigma$. The characteristic cation-anion interaction energy is therefore $\epsilon_\pm = -u(\sigma) = 44\epsilon$. In order to increase the efficiency of ion-pair insertions and deletions in *GC*-WLEXT simulations, we employed a distance-biased scheme similar to that in Ref. [60], but with a Gaussian biasing function. In *GC*-WLEXT simulations, ion

numbers within the fixed volume $V = 1000\sigma^3$ varied in the range $0 \leq N/2 \leq 163$, corresponding to ion densities of $0 \leq \rho^* = N\sigma^3/V \leq 0.326$; in NpT-WLEXT simulations, $N = 128$ ions were simulated at densities in the range $10^{-4} \leq \rho^* \leq 0.4$. The WL simulation protocol was the same as that described in Sec. 4.2.1.

The coexistence envelopes are shown in Fig. 4.3. GC-WLEXT and NpT-WLEXT results do not coincide perfectly at all temperatures, but we attribute this to strong finite-size effects connected with the particle number; in GC-WLEXT, the number of ion pairs in the vapour phase is very small, whereas in NpT-WLEXT, the number of ions is fixed. There is a substantial amount of scatter in the data points, which is caused by very broad and flat number-density probability distributions, which in turn complicates the identification of a boundary between liquid and vapour peaks and the subsequent computation of $\langle\rho_{\rm vap}\rangle$ and $\langle\rho_{\rm liq}\rangle$. In order to assess the statistical errors, we performed four independent GC-WLEXT simulations at each temperature and calculated the statistical uncertainties based on one standard deviation; these are shown as horizontal errorbars in Fig. 4.3. It was not possible to improve the accuracy of the individual simulations by requiring a lower limit on f or a higher minimum count of visited states. Average simulation times for one state point were 4h with GC-WLEXT and 48h with NpT-WLEXT.

Rough estimates of the critical temperatures and densities obtained using fits of Eq. (4.4) are $T_c^* = k_B T_c/\epsilon = 2.07(1)$ and $\rho_c^* = 0.073(2)$ using GC-WLEXT, and $T_c^* = 2.059(3)$ and $\rho_c^* = 0.070(1)$ using NpT-WLEXT. Interestingly, the critical density for CSSs obtained here is quite close to the corresponding value for the RPM, $\rho_c^* = \rho\sigma_{\rm HS}^3 = 0.0790(25)$ [13]. The RPM critical temperature is $k_B T_c D\sigma_{\rm HS}/q^2 = 0.05069(2)$ [13], where $q^2/D\sigma_{\rm HS}$ is the magnitude of the minimum cation-anion energy; the corresponding parameter for CSSs is $\epsilon_\pm = 44\epsilon$, leading to an 'ionic' critical temperature of $k_B T_c/\epsilon_\pm \simeq 0.047$, which is comparable to that for the RPM. Comparison to real molten salts can be made by using an atom diameter $\sigma \simeq 2.8 \times 10^{-10} m$, which is an approximate value often used for simulations of Sodium Chloride [61], and $q = 1.602176 \times 10^{-19} C$. The thus predicted critical temperature is $T_c^{NaCl} \simeq 1.23 \times 10^5 K$, roughly one order of magnitude higher than the melting temperature for NaCl, $T_{melt}^{NaCl} \simeq 1074 K$ [61].

We note that the use of the scaling law Eq. (4.4) is questionable because corrections to scaling, and a crossover between classical and Ising regimes, are expected to occur within the range of temperatures being fitted. Nonetheless, the resulting curves look reasonable, and the apparent critical temperatures serve as useful estimates.

We also investigated the possibility of 'parallelising' GC-WLEXT simulations by splitting up the interval in N to be sampled, and running separate simulations for each

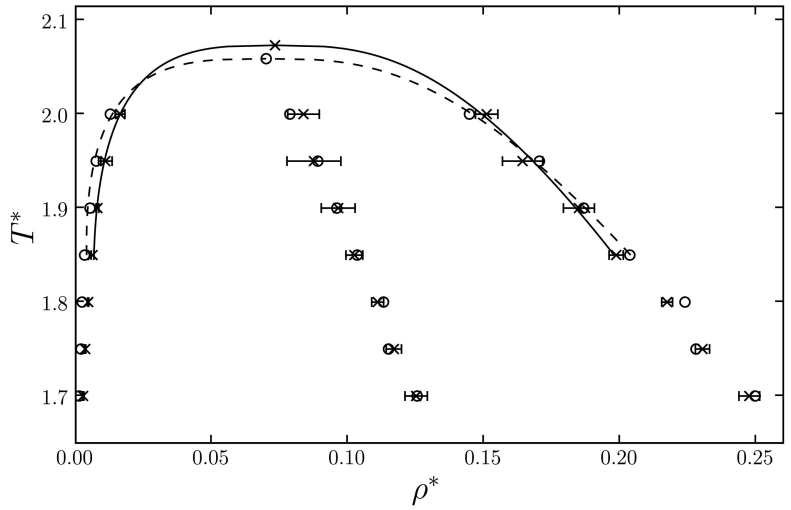

Figure 4.3: Vapour-liquid coexistence envelopes for the charged soft sphere fluid from simulations (points) and fits to the simulation points at $T^* \geq 1.85$ using Eq. (4.4) (lines): GC-WLEXT – crosses and solid lines; NpT-WLEXT – circles and dashed lines.

subinterval. This greatly reduces the time required to sample all relevant particle numbers uniformly. A simplistic argument is as follows. Consider an interval in N to be sampled, which we denote by ΔN. If the sampling process is approximated by a one-dimensional random walk in N (which is valid in the limit $f \to 1$), then the sampling time required to visit all states in the interval is proportional to the square of the size of the interval, i.e., $t \propto (\Delta N)^2$. If ΔN is divided in to n subintervals of width $\delta N = \Delta N/n$, then the simulation time $t \propto n \times (\delta N)^2 = (\Delta N)^2/n$. This implies that to sample a given range ΔN, the total simulation time is reduced by a factor comparable to the number of subintervals. As an illustration, GC-WLEXT simulations of CSSs in the density range $0 \leq \rho^* \leq 0.3$ at $T^* = 1.9$ and $V = 2197\sigma^3$ were run until $\ln f = 10^{-6}$. We allowed for an overlap of 10 particles between neighbouring subintervals and joined $Q(N, V, T)$ from each subinterval by scaling them such that the midpoints of the overlapping regions were aligned. By simultaneously running simulations over equal subintervals in N, the total simulation times were 9.4h, 4.7h, and 3.0h with one, two, and four subintervals, respectively, roughly conforming to a $1/n$ scaling. For a larger system with $V = 4096\sigma^3$, the total simulation time required to reach convergence within four equal subintervals was 10.7h, which is to be compared with the time of 3.0h for calculations with the same number of subintervals but with half of the volume and hence half the value of ΔN; these results are roughly in line with the suggested $(\Delta N)^2$ scaling.

4.2.3 Stockmayer fluid

The phase behaviour of strongly dipolar fluids is the subject of a long-running and somewhat controversial debate, which has been comprehensively reviewed several times [62, 63]. In fact, this topic will be examined in depth in Chapters 6 and 7. Briefly, de Gennes and Pincus suggested in 1970 that fluids of dipolar hard spheres should exhibit an entirely conventional phase diagram – with vapour, liquid, supercritical fluid, and solid phases – because the leading-order isotropic interaction obtained by a Boltzmann-weighted orientational average of the dipole-dipole interaction potential varies like $-1/r^6$, just like dispersion interactions [64]. The results of computer simulations published in the 1990s suggested otherwise. In the case of dipolar hard spheres, Caillol could find no evidence of a vapour-liquid transition [5] although more recent work suggests that this was due to the simulated isotherms being supercritical [65, 66]. Another widely studied dipolar system is the Stockmayer fluid, the interaction potential for which is

$$u(r_{ij}) = 4\epsilon \left[\left(\frac{\sigma}{r_{ij}} \right)^{12} - \left(\frac{\sigma}{r_{ij}} \right)^{6} \right] + \frac{(\boldsymbol{\mu}_i \cdot \boldsymbol{\mu}_j)}{r_{ij}^3} - \frac{3(\boldsymbol{r}_{ij} \cdot \boldsymbol{\mu}_i)(\boldsymbol{r}_{ij} \cdot \boldsymbol{\mu}_j)}{r_{ij}^5} \tag{4.6}$$

where $\boldsymbol{\mu}_i$ is the dipole moment on particle i, and the dipole strength $\mu = |\boldsymbol{\mu}_i|$ is the same for all particles. The conventional reduced units are temperature $T^* = k_B T/\epsilon$, number density $\rho^* = \rho\sigma^3$, and dipole strength $\mu^* = \sqrt{\mu^2/\epsilon\sigma^3}$. Gibbs ensemble MC (GEMC) simulations of the Stockmayer potential suggested that the vapour-liquid transition is absent from the phase diagram when $(\mu^*)^2 \geq 24.3$ [4, 67, 68]. (Note that van Leeuwen and Smit [4] actually simulated a slightly different potential, but one that can be mapped on to the Stockmayer potential [68]; therefore, we only quote equivalent results for the Stockmayer potential.) The disappearance of the vapour-liquid transition has been put down to the formation of chain-like aggregates at low temperatures, with the dipoles in the chains aligned 'nose-to-tail' [69]. The absence of the transition in some simulations is almost certainly connected with aggregation, but it may be an artifact rather than a real physical effect. The GEMC technique relies on effecting a sufficient number of particle and volume transfers between two different simulation boxes [70] but the presence of strong aggregation drastically reduces the probability of accepting a simultaneous particle deletion (from one box) and particle insertion (in the other box). In addition, the network of chain-like aggregates severely restricts volume moves. Therefore, it is possible that the disappearance of the vapour-liquid transition in GEMC simulations is actually due to the simulations failing to achieve equilibration and convergence.

Any sort of grand-canonical simulation of strongly dipolar particles is going to be hard work, because of the requirement to execute sufficient numbers of particle insertions

and deletions. Nonetheless, we managed to perform *GC*-WLEXT simulations of the Stockmayer fluid with dipole strengths $(\mu^*)^2 = 24$, 27, and 30; the phase behaviour at low dipole strengths is already well established [4, 68, 71–74]. The system volume was $V = L^3 = 1000\sigma^3$, with particle numbers in the range $0 \leq N \leq 600$. The Lennard-Jones component of the potential was cut off at $L/2$ with no long-range correction applied, while the long-range dipolar interactions were handled using Ewald sums and conducting boundary conditions [18]. *GC*-WLEXT simulations were performed covering intervals of 100 particles plus overlaps of 10 particles with neighbouring intervals in order to help splice together the different portions of $Q(N, V, T)$. For $(\mu^*)^2 = 24$, 27, and 30 we performed 3, 5, and 10 independent runs, respectively, at each temperature and averaged the results. Higher dipole strengths required more independent runs due to the difficulty of sampling (by any means) strongly aggregated fluids. We could not simulate higher values of μ^* because the underlying density of states becomes extremely rough due to the presence of system-spanning chains, artificially stabilised by the periodic boundary conditions. Note that this is a limitation of the finite-size system, and not a failure of the simulation technique *per se*.

The phase diagrams for systems with $(\mu^*)^2 = 24$, 27, and 30 are shown in Fig. 4.4; the apparent critical parameters obtained by fits of Eq. (4.4) are $\{T_c^* = 7.18, \rho_c^* = 0.188\}$, $\{T_c^* = 7.89, \rho_c^* = 0.173\}$, and $\{T_c^* = 8.50, \rho_c^* = 0.165\}$, respectively. Our results at $(\mu^*)^2 = 24$ are consistent with earlier work [4, 68, 71–73], and following Bartke and Hentschke [74], we confirm that the transition persists at higher dipole strengths, at least up to $(\mu^*)^2 = 30$. These findings show that the *GC*-WLEXT method can indeed be used with success for simulation of phase coexistence in highly complex fluids.

4.2.4 Isotropic-nematic transition in Gay-Berne mesogens

The isotropic-nematic (I-N) transition in the Gay-Berne model of liquid crystals involves a very small change in density and requires an enormous number of traditional NpT MC simulations to locate accurately [75–77]. The Gay-Berne potential is given by

$$u(\boldsymbol{r}_{ij}, \boldsymbol{u}_i, \boldsymbol{u}_j) = 4\epsilon(\boldsymbol{r}_{ij}, \boldsymbol{u}_i, \boldsymbol{u}_j) \left\{ \left[\frac{\sigma_0}{d(\boldsymbol{r}_{ij}, \boldsymbol{u}_i, \boldsymbol{u}_j)} \right]^{12} - \left[\frac{\sigma_0}{d(\boldsymbol{r}_{ij}, \boldsymbol{u}_i, \boldsymbol{u}_j)} \right]^{6} \right\} \tag{4.7}$$

where $\boldsymbol{r}_{ij}$ is the interparticle separation vector, $\boldsymbol{u}_i$ is the orientational vector along the symmetry axis of particle i, and $d(\boldsymbol{r}_{ij}, \boldsymbol{u}_i, \boldsymbol{u}_j) = |\boldsymbol{r}_{ij}| - \sigma(\boldsymbol{r}_{ij}, \boldsymbol{u}_i, \boldsymbol{u}_j) + \sigma_0$. The quantities $\epsilon(\boldsymbol{r}_{ij}, \boldsymbol{u}_i, \boldsymbol{u}_j)$ and $\sigma(\boldsymbol{r}_{ij}, \boldsymbol{u}_i, \boldsymbol{u}_j)$ are orientation dependent and proportional to the basic energy and range parameters ϵ_0 and σ_0, respectively. The full expressions are given in Ref. [75], but we note that they depend on two further parameters: κ, which defines the aspect ratio of the (roughly) ellipsoidal molecules; and κ', which sets the ratio

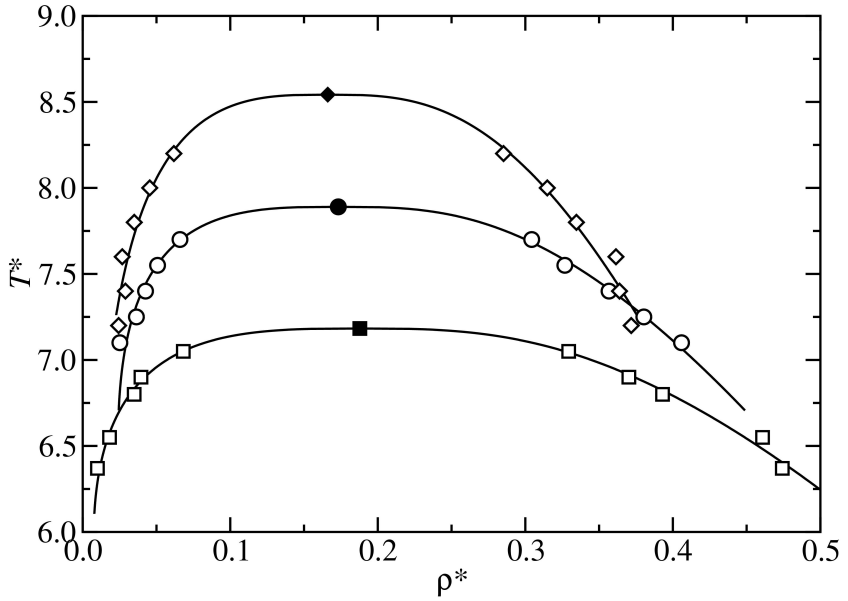

Figure 4.4: vapour-liquid coexistence envelopes for the Stockmayer fluid from *GC*-WLEXT simulations (points) and fits to the simulation points using Eq. (4.4) (lines): $(\mu^*)^2 = 24$ – squares; $(\mu^*)^2 = 27$ – circles; $(\mu^*)^2 = 30$ – diamonds. The critical points are indicated with filled symbols.

between the potential-energy wells for the side-by-side and end-to-end configurations. We focus our attention on the system with $\kappa = 3$ and $\kappa' = 5$ as studied in previous work [75–77]. Using thermodynamic integration techniques, de Miguel [76] determined the coexistence properties at a temperature $T^* = k_B T/\epsilon_0 = 1.25$ to be $P^* = P\sigma_0^3/\epsilon_0 = 5.20$, $\rho_{\mathrm{I}}^* = \rho_{\mathrm{I}}\sigma_0^3 = 0.3152$ and $\rho_{\mathrm{N}}^* = \rho_{\mathrm{N}}\sigma_0^3 = 0.3219$.

With the output from a single WL simulation, we can calculate the isothermal compressibility κ_T for a range of pressures. In a finite-size simulation, a peak in κ_T plotted as a function of P can signal a first-order transition between two phases differing in density. Statistical expectation values in the NpT ensemble can be calculated with $Q(N, V, T)$ obtained from NpT-WLEXT simulations by numerical integration, as in Eq. (4.3). The compressibility as a function of p is thus readily obtained from the fluctuation formula [18]

$$\kappa_T = -\frac{1}{V}\left(\frac{\partial V}{\partial P}\right)_{N,T} = \frac{\langle V^2\rangle - \langle V\rangle^2}{\langle V\rangle\, k_B T}. \tag{4.8}$$

In the NpT-WLEXT simulations $N = 192$ particles were used, and the potential was truncated at $r = 4\sigma_0$ with no long-range corrections applied. We did not attempt *GC*-WLEXT simulations for this model because the number of successful particle insertions/deletions is expected to be prohibitively low in the density range $0.25 \leq \rho^* \leq 0.35$ considered here. Rotations and translations were performed independently with maximum displacements chosen to give an acceptance ratio of approximately 50%.

Results for the equation of state, compressibility, and nematic order parameter S (computed as described in Ref. [78]) are shown in Fig. 4.5, along with available existing canonical molecular dynamics data for $N = 500$ particles [75, 76]. In addition to the NpT-WLEXT results, we show the results of our own standard NpT simulations with $N = 192$ particles. Using the NpT-WLEXT data, we also calculated $\langle p \rangle$ as a function of ρ (canonical ensemble average) by differentiating $F = -k_B T \ln Q(N, V, T)$ numerically, but the results were indistinguishable from those obtained by computing $\langle \rho \rangle$ as a function of p (NpT ensemble average). This is due to the fact that there is no observable 'van der Waals' loop in the canonical-ensemble equation of state, and no pronounced hysteresis in the NpT results; the absences of these features in simulations of weak I-N transitions have been noted before [78]. A clear peak in κ_T emerges at $p^* \simeq 5.25$ (corresponding to a density $\rho^* \simeq 0.32$) which coincides with the jump in the nematic order parameter. This pressure is quite close to the coexistence pressure $p^* = 5.20$ identified by de Miguel [76]. It proved impossible to resolve a bimodal density distribution $P(\rho)$ from the NpT-WLEXT results at the apparent coexistence pressure because the change in density is too small. In an attempt to improve on this we performed simulations on a slightly larger system with $N = 324$ but it was still not possible to observe a bimodal distribution; the peak in κ_T occurs at essentially the same pressure as in the $N = 192$ system. The overall agreement between standard NpT, NpT-WLEXT, and canonical molecular dynamics [75, 76] simulations is good. Therefore, the NpT-WLEXT offers a viable route to mapping out the equation of state at fixed temperature from a single simulation – even for dense fluids. A similar simulation has been reported in Ref. [52], where the athermal isotropic-cubatic phase transition of cuboidal particles constructed from hard spheres was probed using a TM based flat-histogram method. In that case, however, the transition is strongly first-order with a difference in density between isotropic and cubatic phases of approximately 10%.

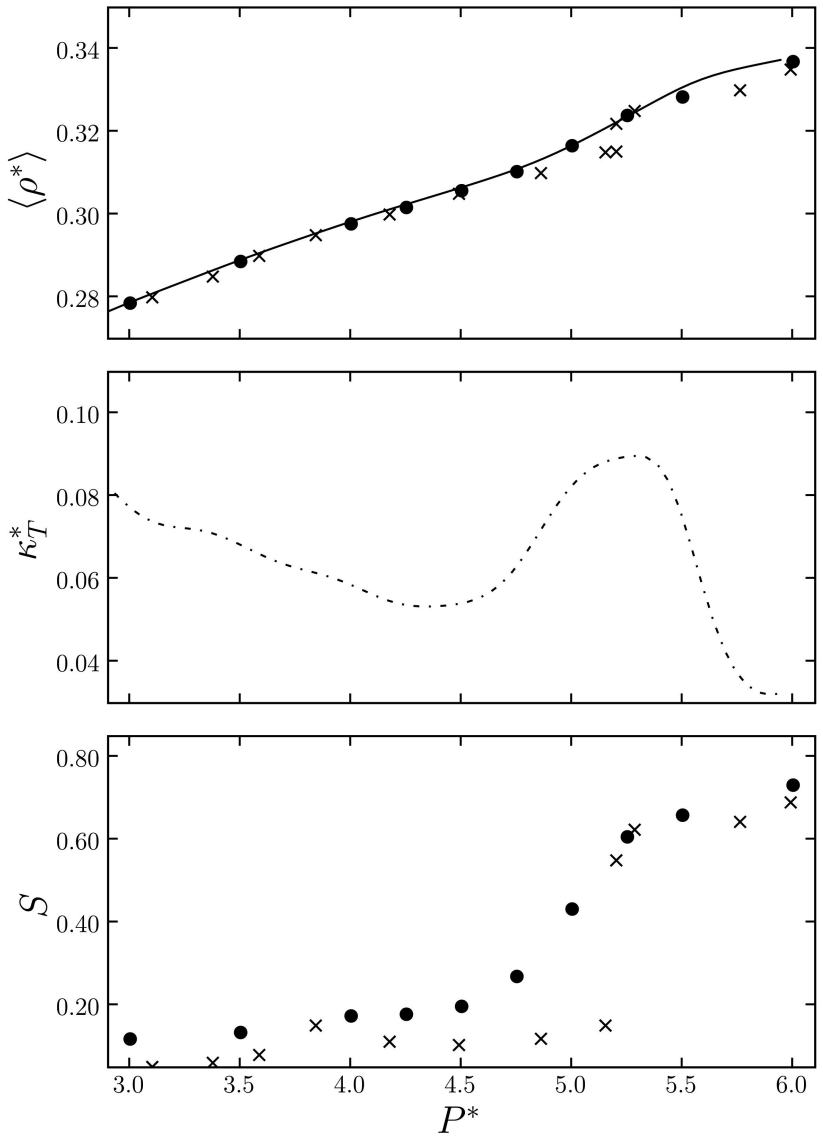

Figure 4.5: Results for Gay-Berne mesogens. (a) Equation of state from NpT-WLEXT simulations (line), standard NpT-MC simulations (circles), and canonical molecular dynamics simulations [75, 76] (crosses). (b) Isothermal compressibility $\kappa_T^* = \kappa_T \epsilon_0 / \sigma_0^3$ from NpT-WLEXT simulations. (c) Nematic order parameter S from standard NpT-MC simulations (circles) and canonical molecular dynamics simulations [75, 76] (crosses).

4.3 Discussion

In this Chapter, a robust method for determining phase coexistence has been presented. The advantage over traditional multicanonical MC techniques is that only the density range and temperature at which a transition is expected to occur is to be specified in advance. The effect of the external field, given by the external pressure in the NpT ensemble, or the chemical potential in the grand-canonical ensemble, is determined after the simulation has converged and it is thus possible to obtain number-density distributions at arbitrary values of the external field (provided a sufficient range of densities has been sampled in the first place). This also implies that the equation of state for the density range considered can be obtained from a single simulation.

The algorithms described here – GC-WLEXT and NpT-WLEXT – belong to the visited-states class of flat-histogram techniques for determining partition functions. GC-WLEXT effects changes in the number density by particle insertions and deletions at fixed volume, while NpT-WLEXT varies the volume at fixed number of particles. We have applied both algorithms to the vapour-liquid transitions in the Lennard-Jones fluid, charged soft spheres, and Stockmayer fluids with high dipole strengths.

For the Lennard-Jones fluid, we find that both algorithms reproduce existing high-quality transition-matrix data with good accuracy. At strongly subcritical temperatures, one might expect deviations between the GC-WLEXT and NpT-WLEXT results for the vapour coexistence density, because the number of particles in the GC-WLEXT simulation is very low compared to that in the NpT simulation. However, for the Lennard-Jones fluid, we find that this effect is not significant.

Surprisingly, the coexistence curves for charged soft spheres from GC-WLEXT and NpT-WLEXT simulations are consistent with one another over the entire temperature range considered, but there is a significant amount of statistical scatter. Rough estimates of the critical parameters obtained from fitting an Ising-like scaling law are $T_c^* \simeq 2.06$ and $\rho_c^* = 0.07$. The apparent critical parameters – expressed in 'ionic' reduced units – are in good accord with those for charged hard spheres (restricted primitive model) [13, 59].

The vapour-liquid coexistence curves for the Stockmayer fluid with high dipole strengths could be generated reliably using the GC-WLEXT approach. Our results – like those of Bartke and Hentschke [74] – indicate that the transition persists well above the critical dipole strength identified by van Leeuwen and Smit [4]. In fact the apparent disappearance of the transition in GEMC simulations [4, 67, 68] is more than likely associated with failures of the simulation methodology.

The natural discretisation of N renders the GC-WLEXT approach computationally more straightforward than NpT-WLEXT. Simulation times for GC-WLEXT reported here are moderate [However, still nowhere near the proclaimed time limit of a good simulation, see page (i)]. In addition, parallelisation of the algorithm is simple because the density range can be split into multiple intervals for which independent simulations are performed. The resulting numerical estimates of the canonical partition functions from each subinterval are then scaled so that they match up at the boundaries [25, 30]. Preliminary investigations of this approach showed that the total time needed to complete a simulation is reduced by a factor comparable to the number of subintervals. In the light of these results, the application of parallelised GC-WLEXT simulations to very large systems is an attractive proposition. Based on these observations, we can recommend using GC-WLEXT for locating vapour-liquid transitions.

In general, we observed that it was not possible to reduce errors in vapour and liquid coexistence densities by increasing the primary adjustable parameters in the WL scheme – the final value of the convergence factor and the flatness of the histogram of visited states. It has been noted before that the WL algorithm does not improve on the statistical error after f has reached a certain value [79]. We therefore propose that if very accurate results are required, a combination of GC-WLEXT and $GCMC$ with multicanonical biasing could be employed: the required value for the chemical potential and a good guess for the multicanonical bias is obtained from a preliminary GC-WLEXT simulation; a multicanonical $GCMC$ simulation can then be run, which also enables the use of histogram reweighting.

The isotropic-nematic transition of Gay-Berne mesogens is only feasible using NpT-WLEXT simulations because the packing fraction in the vicinity of the transition is too high to effect particle insertions and deletions. Unfortunately, the transition is so weak that a bimodal density distribution could not be obtained; this property of the isotropic-nematic transition gives rise to problems in other 'direct' simulation techniques [78]. Nonetheless, by calculating the compressibility and equation of state from a single simulation, we could locate the transition pressure. Therefore, the NpT-WLEXT technique might also find application in the simulation of strong, first-order phase transitions at high densities.

Part II – Vapour-liquid transition in dipolar fluids

Chapter 5

Introduction to the vapour-liquid transition in dipolar hard spheres

Dipolar hard spheres (DHSs) represent the simplest model of polar liquids and colloidal ferrofluids. Despite several decades of intensive theoretical and simulation work, some questions concerning the properties of dipolar fluids remain [62, 63, 80]. The existence of ferroelectric or ferromagnetic fluid phases has been discussed widely [81–86].

In simple fluids with isotropic attractive interactions of sufficient range [87] the condensation transition occurs between a low-density vapour with high potential energy and high entropy, and a high-density liquid with low potential energy and low entropy. Systems with strong dipolar interactions, however, seem to behave very differently. The Boltzmann-weighted, orientational average of the dipolar interaction potential has an isotropic, attractive, leading-order term proportional to $-1/r^6$ where r is the particle separation, and one might therefore anticipate that the condensation transition in such systems would be conventional [64]. Computer simulations show that at low temperatures, the anisotropy and long range of dipolar interactions give rise to extensive chain-like aggregation at low densities [69] and branched-network formation at high densities [88], the primary structural signature being the nose-to-tail conformation of neighbouring dipoles. It is unclear whether such association precludes any kind of fluid-fluid coexistence.

The anisotropic, dipole-dipole (DD) interaction potential reads

$$u_{\mathrm{DD}}(\boldsymbol{r}, \boldsymbol{\mu}_1, \boldsymbol{\mu}_2) = \frac{(\boldsymbol{\mu}_1 \cdot \boldsymbol{\mu}_2)}{r^3} - \frac{3(\boldsymbol{\mu}_1 \cdot \boldsymbol{r})(\boldsymbol{\mu}_2 \cdot \boldsymbol{r})}{r^5} \tag{5.1}$$

where $\boldsymbol{r}$ is the centre-centre separation vector, $r = |\boldsymbol{r}|$, and $\boldsymbol{\mu}_i$ is the dipole moment on particle i. The dipolar potential may then be supplemented with either a soft or

a hard short-range repulsion to guarantee mechanical stability, and any other relevant interactions for a specific system. DHSs are formed by combination of u_{DD} with the hard sphere (HS) potential

$$u_{\mathrm{HS}}(r) = \begin{cases} \infty & r < \sigma \\ 0 & r \geq \sigma \end{cases} \tag{5.2}$$

where σ is the particle diameter. Conventional theoretical calculations on DHSs, such as thermodynamic perturbation theory (e.g. [1]) and integral equations [2] support the existence of a vapour-liquid phase transition. Early simulation results on small systems of DHSs – but without proper treatment of the long-range dipolar interactions – qualitatively confirmed this picture [3]. Direct experimental tests are so far impossible, primarily because of the difficulty in producing monodisperse, single-domain magnetic nanoparticles with sufficiently strong dipole moments.

It came as something of a surprise in the early 1990s when more sophisticated simulation techniques indicated the absence of a vapour-liquid transition in systems of strongly interacting dipolar particles. Gibbs-ensemble Monte Carlo (MC) calculations by van Leeuwen and Smit showed that, when dipolar interactions dominate over short-range isotropic attractions proportional to $-r^{-6}$, a vapour-liquid coexistence region is apparently absent from the phase diagram. Instead, the particles form extended chain-like structures resembling a living-polymer network, stabilised by the energetically favourable nose-to-tail parallel conformation of neighbouring dipoles. [4]. The system studied by van Leeuwen and Smit can be mapped on to the Stockmayer (SM) fluid [89], for which the interaction potential is a combination of Lennard-Jones and dipole-dipole terms:

$$u_{\mathrm{SM}}(\boldsymbol{r}, \boldsymbol{\mu}_1, \boldsymbol{\mu}_2) = 4\varepsilon \left[\left(\frac{\sigma}{r}\right)^{12} - \left(\frac{\sigma}{r}\right)^{6} \right] + u_{\mathrm{DD}}(\boldsymbol{r}, \boldsymbol{\mu}_1, \boldsymbol{\mu}_2). \tag{5.3}$$

It was observed that the transition disappeared when the characteristic dipolar interaction energy μ^2/σ^3 (with $\mu = |\boldsymbol{\mu}|$) measured against the Lennard-Jones well depth ε, exceeded a critical value $\mu^2/\varepsilon\sigma^3 = 24.3$ [4, 67, 89].

In the case of DHSs, Caillol did not see any sign of phase separation in constant-pressure and Gibbs-ensemble MC simulations at reduced temperatures $k_B T\sigma^3/\mu^2 = 0.18$ and 0.222 [5]. The chain-like clustering in DHS fluids was thoroughly characterised by Weis and Levesque [69, 90].

A number of other model dipolar fluids were studied throughout the 1990s, all seemingly sharing the property that phase separation is somehow precluded by the formation of chain-like clusters. McGrother and Jackson studied hard spherocylinders with longitudinal dipoles as a function of the length (L) to breadth (D) ratio L/D [91] and found that phase separation does not occur below a critical value of $L/D > 0$ (the DHS limit

being $L/D = 0$). Szalai *et al.* studied a so-called dipolar Yukawa hard sphere (DYHS) fluid [92] with an interaction potential given by

$$u_{\mathrm{DYHS}}(\boldsymbol{r}, \boldsymbol{\mu}_1, \boldsymbol{\mu}_2) = u_{\mathrm{HS}}(r) + u_{\mathrm{DD}}(\boldsymbol{r}, \boldsymbol{\mu}_1, \boldsymbol{\mu}_2) - \varepsilon_{\mathrm{Y}} \left(\frac{\sigma}{r}\right) e^{-z(r-\sigma)} \tag{5.4}$$

where ε_{Y} is the well depth of the attractive isotropic Yukawa interaction, and $z = 1.8/\sigma$ is a decay parameter. Using the NpT+test particle insertion technique, Szalai *et al.* found that condensation exists only for $\mu^2/\varepsilon_{\mathrm{Y}}\sigma^3 \leq 9$ [92]. In the light of this collected simulation evidence, several theoretical works set out to explain why the vapour-liquid transition disappears when the propensity for chaining (in the cases above, related to the strength of the dipolar interactions) exceeded some critical level [93–96].

Recent simulation and theoretical results have reignited the controversy. In 2000, Camp *et al.* suggested that, on the basis of MC simulation results, two or more distinct isotropic fluid phases may be present in DHSs [65]. In the same year, Tlusty and Safran presented a mechanism which accommodates phase separation in strongly clustered dipolar fluids [8]; in essence, the transition is driven by the free energies of defects, these being particles at the ends of chains ('end' defects) and particles having three nearest neighbours ('Y' defects). Fig. 1.5 in the Introduction visualises these defect types. This semi-phenomenological approach has the benefit of acknowledging, at the outset, the presence of very strong positional and orientational correlations between particles, which other theoretical approaches can only hint at through series expansions, integral-equation closures, etc. In 2007, Hentschke *et al.* [97] reported phase separation in the Stockmayer fluid for dipole interaction strengths up to $\mu^2/\varepsilon\sigma^3 = 36$, well beyond the limit proposed by van Leeuwen and Smit in 1993 [4]; and Bartke and Hentschke state that a 'van der Waals loop' is visible in the equation of state for a system with $\mu^2/\varepsilon\sigma^3 = 100$ [74], which may indicate a phase transition. These results, which had been obtained from molecular dynamics simulations, were confirmed in a subsequent study by the author of this thesis (see Chapter 4.2.3). A critical comparison of all available Stockmayer-fluid results has been presented [33], and an attempt has been made to map the Stockmayer fluid on to DHSs [98]. In 2008, the author reported phase separation in the DYHS fluid for dipole interaction strengths up to $\mu^2/\varepsilon_{\mathrm{Y}}\sigma^3 = 36$ (see Chapter 7.4.1), significantly higher than the upper limit proposed by Szalai *et al.* in 1999 [92] (see Sec. 7.4.1).

Why are the new results so different from those in earlier works? One possible reason is that many of the pioneering studies employed the Gibbs-ensemble MC technique [70] which is almost certainly going to fail when there is very strong particle association in both the dilute and concentrated coexisting phases [99]; the probability of accepting simultaneous particle deletion in one box and particle insertion in the other is so low that convergence becomes practically impossible. Even single-box simulation techniques,

such as constant-pressure MC simulations, have convergence problems due to the low probability of accepting volume changes in low-density systems with almost-percolating networks of particles. In recent times, grand-canonical ensemble simulations have become the method of choice for examining condensation transitions, but these too can run in to problems due to the low probabilities of inserting or deleting particles from extended clusters.

Various strategies have been attempted for sneaking up on purely dipolar systems, starting from models which are relatively easy to simulate. In 2007, the author studied so-called charged hard dumbbells charged hard spheres fused into cation-anion pairs with centre-centre separation d; DHSs correspond to the limit $d/\sigma \to 0$, and the extrapolation of critical parameters for systems in the range $0.1 \leq d/\sigma \leq 0.25$ yielded estimates for the DHS critical temperature and critical density of $k_{\mathrm{B}}T_{\mathrm{c}}\sigma^3/\mu^2 = 0.153(1)$ and $\rho_{\mathrm{c}}\sigma^3 \simeq 0.1$, respectively. In 2008, Almarza *et al.* [100] studied mixtures of apolar and dipolar hard spheres; extrapolating vapour-liquid critical parameters to the limit of vanishing apolar-sphere concentration yielded estimates for the DHS critical parameters of $k_{\mathrm{B}}T_{\mathrm{c}}\sigma^3/\mu^2 = 0.153(3)$ and $\rho_{\mathrm{c}}\sigma^3 = 0.06(5)$, very close to those obtained by the author for the charge hard dumbbells model. However, while these results hint at the existence of vapour-liquid separation in DHS, a large-scale finite-size simulation study of DYHS by the author contradicts these findings.

In the following, results for the charged hard dumbbells are presented in Chapter 6, and for the dipolar Yukawa system in chapter 7.

Chapter 6

Vapour-liquid condensation in charged hard dumbbells

6.1 Introduction

This chapter makes an approach towards vapour-liquid coexistence in dipolar fluids by studying so-called charged hard dumbbells (CHDs) [58] with extensive MC simulations. Each CHD is made up of two oppositely charged hard spheres with diameters σ and charges $\pm q$, fused at a centre-centre distance d; see Fig. 6.1(a). When $d = \sigma$ the transition is very similar to that in the restricted primitive model (RPM) of ionic fluids [13, 101, 102]; in the RPM, oppositely charged ions associate at low temperature to form ion pairs that resemble CHDs [58, 103], and see Fig.4.1 in Chapter 4. As $d/\sigma \to 0$, and with the temperature scaled accordingly, the CHD model can be mapped on to DHSs with dipole moment $\mu = qd$. Hence, the CHD model provides a convenient bridge between 'ionic' condensation (typified by the RPM, and CHDs with $d/\sigma = 1$) and pure dipolar condensation.

6.2 Simulation details

(45:315:0.5); $\boldsymbol{d}$; $\boldsymbol{\sigma}$; Two oppositely charged hard spheres with diameters σ and The ionic interaction potential is $q_i q_j / Dr$ where $D = 4\pi\epsilon_0$. Reduced units for the CHD model are as follows: 'ionic' temperature $\tau^i = k_B T D\sigma/q^2$; 'dipolar' temperature $\tau^d = k_B T D\sigma^3/\mu^2 = \tau^i\sigma^2/d^2$; reduced density $\rho^* = \rho\sigma^3$, where $\rho = N/V$ is the number of CHDs (N) in a volume V. Grand-canonical Monte Carlo ($GCMC$) simulations were performed using a cubic simulation cell with periodic boundary conditions applied.

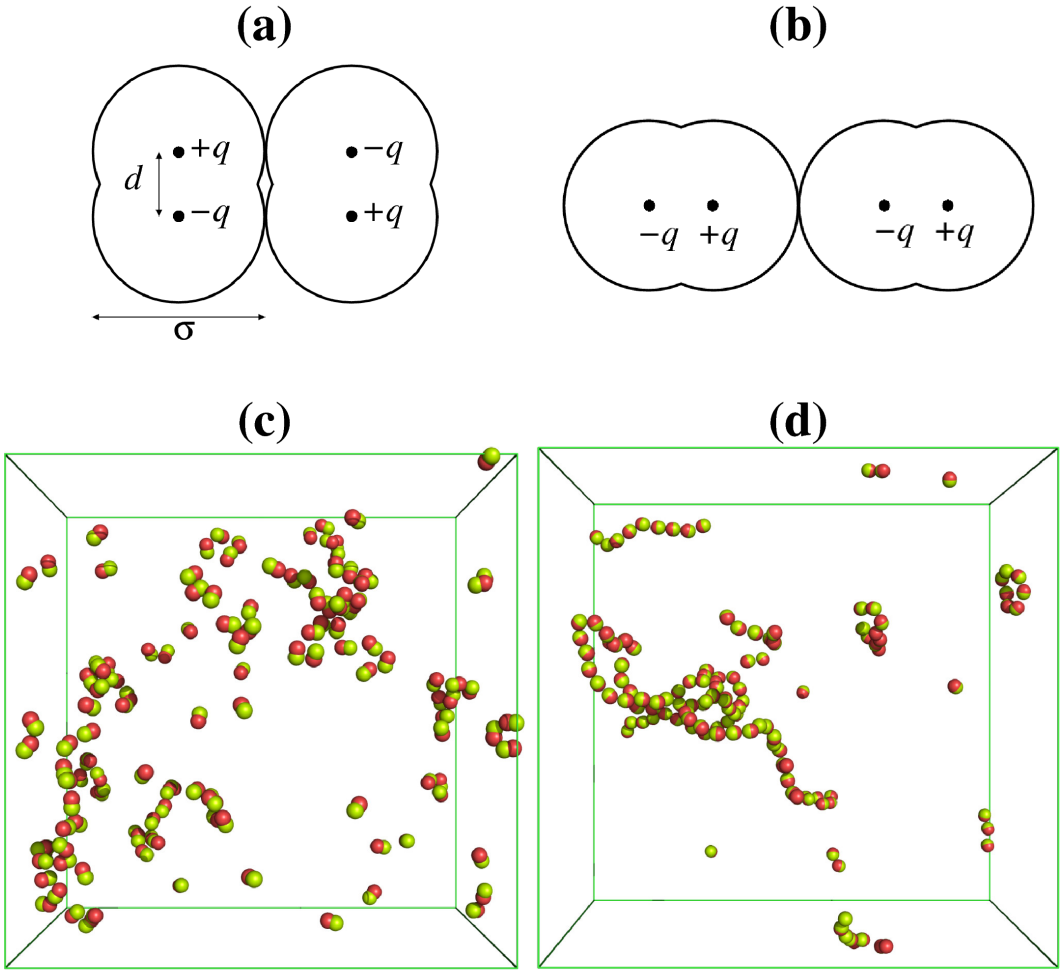

Figure 6.1: Configurations of CHDs: (a) side-by-side, antiparallel arrangement; (b) nose-to-tail, parallel arrangement; (c) vapour phase with $d/\sigma = 0.5$ at $\tau^d = 0.0777$ and $\rho^* = 0.0055$; (d) vapour phase with $d/\sigma = 0.1$ at $\tau^d = 0.126$ and $\rho^* = 0.0035$.

Coulomb interactions were evaluated using Ewald sums with conducting boundary conditions [18]. CHD translations and rotations were effected through attempted deletions and random insertions. Multicanonical preweighting as described in Chapter 2 was used to overcome the free-energy barrier separating coexisting phases; the weighting function $W(N)$ was iterated during each simulation to achieve uniform sampling across the full range of density. Simulations at each state point consisted of between 10^9 and 10^{10} insertion/deletion attempts, and the particle number and configurational energy E were recorded at intervals of 100-500 such attempts. Histogram reweighting was used to combine data obtained with different chemical potentials and temperatures to form the joint probability distribution function $P(N, E)$ from which thermodynamic functions can be

computed over the ranges of parameters sampled in the simulations. Coexisting phases were identified by equating the temperatures, chemical potentials, and pressures. The complete procedure (comprising multicanonical preweighting, histogram reweighting, and the determination of phase coexistence) was implemented as described in Ref. [53]. The lengths of the simulations (total of ~ 2 CPU years) precluded a finite-size scaling study of the critical behaviour, and so one system size ($L/\sigma = 12.5$ or 13) was adopted for each value of d/σ. Estimates of the critical parameters were obtained by fitting the coexistence densities to the equation $\rho_\pm = \rho_c + At \pm Bt^\beta$, where ρ_c is the critical density, $t = |T - T_c|/T_c$, T_c is the critical temperature, and $\beta = 0.326$ is the 3D-Ising order-parameter exponent [1].

6.3 Results

Coexistence curves in the ρ^*-τ^d plane are shown in Fig. 6.2. The results indicate that the condensation transition exists all the way down to almost purely dipolar hard particles ($d = 0.1\sigma$). Beyond this point, the simulations became intractable due to the extent of aggregation. At low densities the simulations become trapped in sharp, local energy minima corresponding to configurations of system-spanning chains. This is a finite-size effect and it does not imply that condensation disappears for $d < 0.1\sigma$. Alternative simulation methods may not improve the situation because the characteristic lengthscale in the fluid is comparable to the box length; the only cure may be to increase the box length by an order of magnitude.

Critical parameters are summarised in Table 6.1; the quoted uncertainties were taken from the fitting procedure only, and are therefore underestimates. The critical temperature and critical density at $d/\sigma = 1$ are in good agreement with earlier finite-size scaling values of $\tau_c^i = 0.04911(3)$ and $\rho_c^* = 0.0505(15)$ [102], which justifies the simulation procedure. The results are also comparable to those for the RPM [13] (also shown in Table 6.1) and a related 'tethered dimer' fluid [101]. The CHD ionic critical temperature decreases with decreasing d because of the reduction in the dipole moment, but the dipolar critical temperature remains finite.

Figure 6.3(a) shows τ_c^d and ρ_c^* as functions of d/σ. As d/σ is decreased, the critical temperature increases monotonically and shows a linear dependence for $d/\sigma < 0.3$. Fitting a straight line to the critical temperatures in the range $d/\sigma < 0.3$ yields an apparent critical temperature for DHSs ($d/\sigma \to 0$) of $\tau_c^d \simeq 0.153 \pm 0.001$. This is in surprisingly

[1] The near-critical data are not suitable for fitting the leading correction-to-scaling term $\propto t^{\beta+\Delta}$ with any confidence. Apparent critical parameters vary by a few percent if classical or fitted effective exponents are used. Ising-exponent fits are sufficient to demonstrate the existence of the transition, and the crossover between ionic and dipolar regimes.

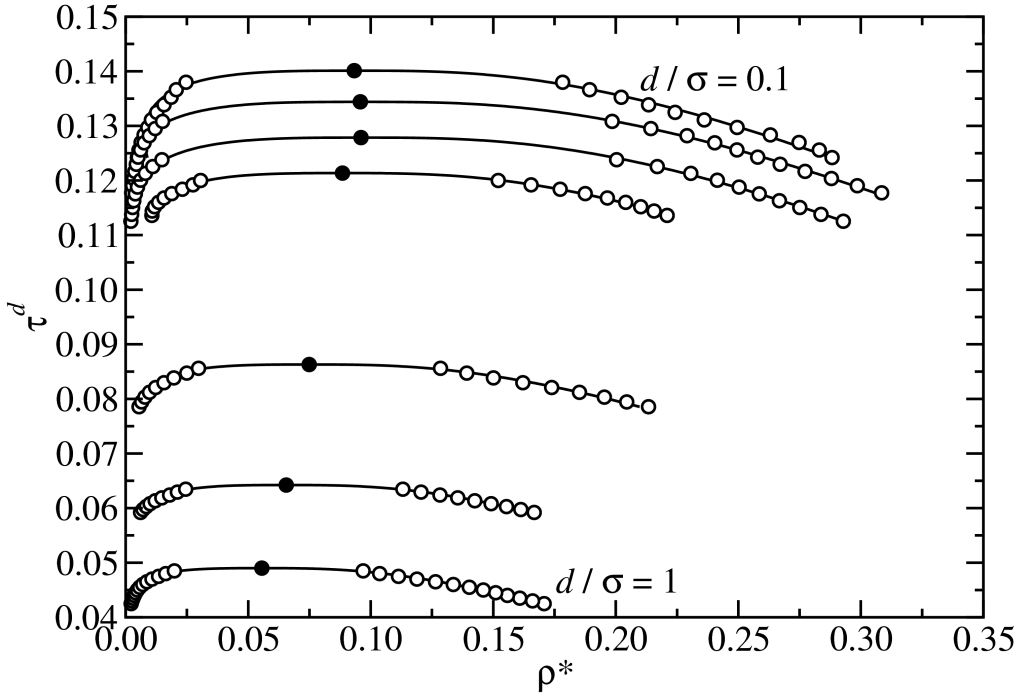

Figure 6.2: Vapour-liquid coexistence curves for CHDs with, from top to bottom, $d/\sigma = 0.1$, 0.15, 0.2, 0.25, 0.5, 0.75, and 1: (open symbols) $GCMC$ simulation results; (lines) fits; (filled symbols) fitted critical points.

d/σ	L/σ	τ_c^i	τ_c^d	ρ_c^*
1	13	0.04900(7)	0.04900(7)	0.0556(2)
0.75	13	0.03612(4)	0.06422(8)	0.0655(1)
0.5	13	0.02157(4)	0.0863(2)	0.0749(5)
0.25	13	0.007585(5)	0.12136(7)	0.0885(9)
0.2	12.5	0.005114(6)	0.1279(1)	0.0960(9)
0.15	12.5	0.003024(4)	0.1344(2)	0.0958(8)
0.1	12.5	0.001401(3)	0.1401(3)	0.0933(8)
RPM	FSS 7–12	0.05069(2)	n/a	0.0790(3)

Table 6.1: Apparent critical parameters of the CHD fluid. For comparison, the critical parameters for the RPM fluid from Ref. [13] are shown in the last line.

good agreement with the rough estimate of $\tau_c^d = 0.15$-0.16 made in Ref. [65]. In 2008, Almarza *et al.* [100] studied mixtures of apolar and dipolar hard spheres; extrapolating vapour-liquid critical parameters to the limit of vanishing apolar-sphere concentration yielded estimates for the DHS critical temperature of $k_{\mathrm{B}}T_{\mathrm{c}}\sigma^3/\mu^2 = 0.153(3)$, in excellent agreement with our results. The apparent critical densities do not vary in a well-defined

way, although these are notoriously difficult to determine accurately because of the flatness of the coexistence curves near the critical point. Nonetheless, a DHS critical density of $\rho_c^* \simeq 0.1$ seems reasonable. This value is again supported by the study of Almarza *et al.* [100] who extrapolate to $\rho_c^* = 0.06(5)$.

Even though the critical temperatures as a function of dumbbell elongation d fall on a perfect straight line *for low d and only up to the smallest value of d considered here*, is highly questionable whether these extrapolations are robust. It might seem unlikely for a new mechanism to emerge in the narrow range $0 < d/\sigma < 0.1$ and prevent the transition to occur, however, anticipating the results of Chapter 7, such a phenomenon indeed appears to exist. Nevertheless, it is instructive to study how the phase behaviour of CHDs is affected by the dumbbell elongation d as done in the following.

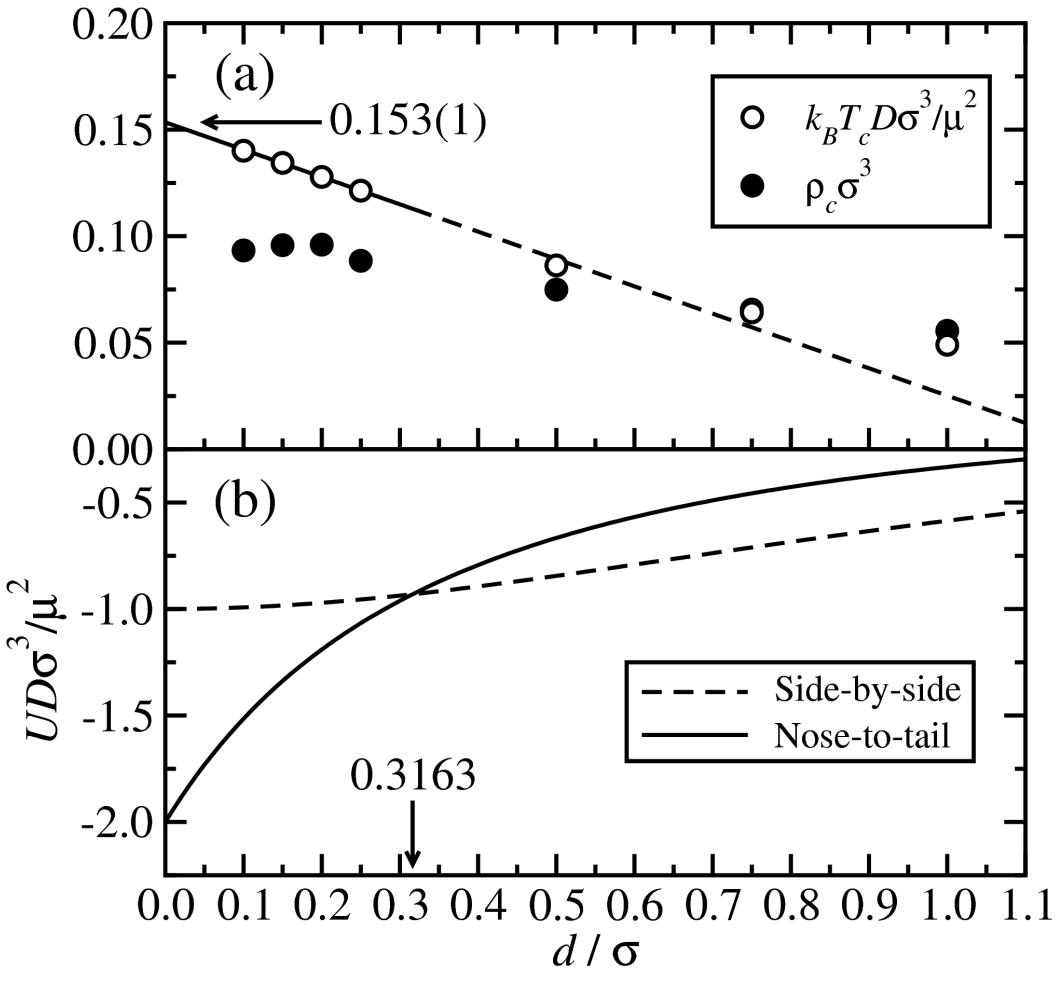

Figure 6.3: (a) Critical temperature (open symbols) and critical density (filled symbols) for CHDs as functions of d/σ. The line is a linear fit to the critical temperatures for $0.1 \leq d/\sigma < 0.3$. (b) Interaction energy of two CHDs at contact in side-by-side antiparallel (dashed line) and nose-to-tail parallel (solid line) arrangements.

The characteristics of condensation in the two regimes $d/\sigma < 0.3$ and $d/\sigma > 0.3$ are different. It is useful to first compare the energies of two CHDs at contact in the antiparallel side-by-side and parallel nose-to-tail arrangements illustrated in Figs. 6.1(a) and 6.1(b), respectively. The energies are plotted in dipolar units in Fig. 6.3(b). The nose-to-tail conformation becomes energetically favourable over the side-by-side conformation when $d/\sigma < 0.3163$. It might therefore be anticipated that when $d/\sigma \lesssim 0.3$ the condensation is 'dipolar' and the coexisting phases contain extended chain-like aggregates, and when $d/\sigma > 0.3$ the condensation is 'ionic' in the sense that the coexisting phases contain more isolated compact clusters such as those in the RPM at coexistence [103]. This is indeed the case, as evidenced by Figs. 6.1(c) and 6.1(d) which show simulation snapshots of vapour phases near coexistence at relative temperature $0.9\tau_c^d$. With $d/\sigma = 0.5$, the clusters are more compact and neighbouring particles are preferentially aligned side-by-side. With $d/\sigma = 0.1$, the vapour exhibits extensive chain-like aggregates. A similar crossover in cluster structure is apparent in fluids of dipolar hard spherocylinders and dumbbells as the hard-core aspect ratios are varied [99, 104].

The structure of the coexisting vapour and liquid phases is reflected in the correlation functions $h_{l_1 l_2 m}(r)$, as defined in the Introduction [Eqns. (1.37)-(1.39)]. Taking the unit orientation vector on molecule i to be parallel with its dipole vector, $h_{110}(r)$ discriminates between side-by-side and nose-to-tail conformations of neighbouring particles. $h_{110}(r)$ was measured in canonical MC simulations of $N = 128$ CHDs in the vapour and liquid phases near coexistence at relative temperature $0.9\tau_c^d$. For comparison, simulations of DHSs were also carried out at comparable densities, and at a temperature of $\tau^d = 0.138$, approximately 0.9 times the critical temperature determined from Fig. 6.3(a). Figures 6.4(a) and 6.4(b) show $h_{110}(r)$ in vapour and liquid phases of CHD systems with $d/\sigma = 1$ and $d/\sigma = 0.1$, and of the DHS system. To aid comparison, the abscissas are scaled by the separation of two nose-to-tail CHDs at contact. In both the vapour and liquid phases of the system with $d/\sigma = 1$, $h_{110}(r)$ is large and negative close to the side-by-side contact separation σ, reflecting antiparallel alignment of the dipoles. Correlations die off rapidly beyond that distance. By contrast, the system with $d/\sigma = 0.1$ exhibits pronounced correlations between parallel dipoles at integer values of the nose-to-tail contact separation $\sigma + d$, reflecting chaining; in the vapour phase, the negative 'blip' at $r \lesssim \sigma + d$ arises from rare instances of the side-by-side conformation. The DHS results are qualitatively similar, although the nose-to-tail correlations are more pronounced. This demonstrates that the CHD model with $d/\sigma = 0.1$ sports the characteristic structural features of the DHS fluid.

A comparison of structures can also be made in reciprocal space via the static structure factor $S(\boldsymbol{q})$ [defined in Eq. (1.36)]. Simulation results for low- and high-density phases are shown in Figs. 6.4(c) and 6.4(d), respectively. $S(q)$ in the CHD system with

$d/\sigma = 0.1$ is almost identical to that in the DHS fluid at the same density and at the same relative temperature, provided that the wavevectors are scaled by the nose-to-tail separation $(\sigma + d)$: features at $q(\sigma + d) \simeq 2\pi$ are due to near neighbours in the nose-to-tail conformation; in the vapour phases, the low-wavevector 'divergence' of $S(q)$ signals aggregation [88]. By contrast, there are clear differences between the results for the CHD system with $d/\sigma = 1$, and those for DHSs. In the liquid, the position of the first major peak in $S(q)$ ($q\sigma \simeq 4.5$) corresponds to a real-space separation of $2\pi/q \simeq 1.4\sigma$. This separation may correspond to the orientationally averaged distance of closest approach for two dumbbells, which would signal the presence of nose-to-tail and side-by-side conformations.

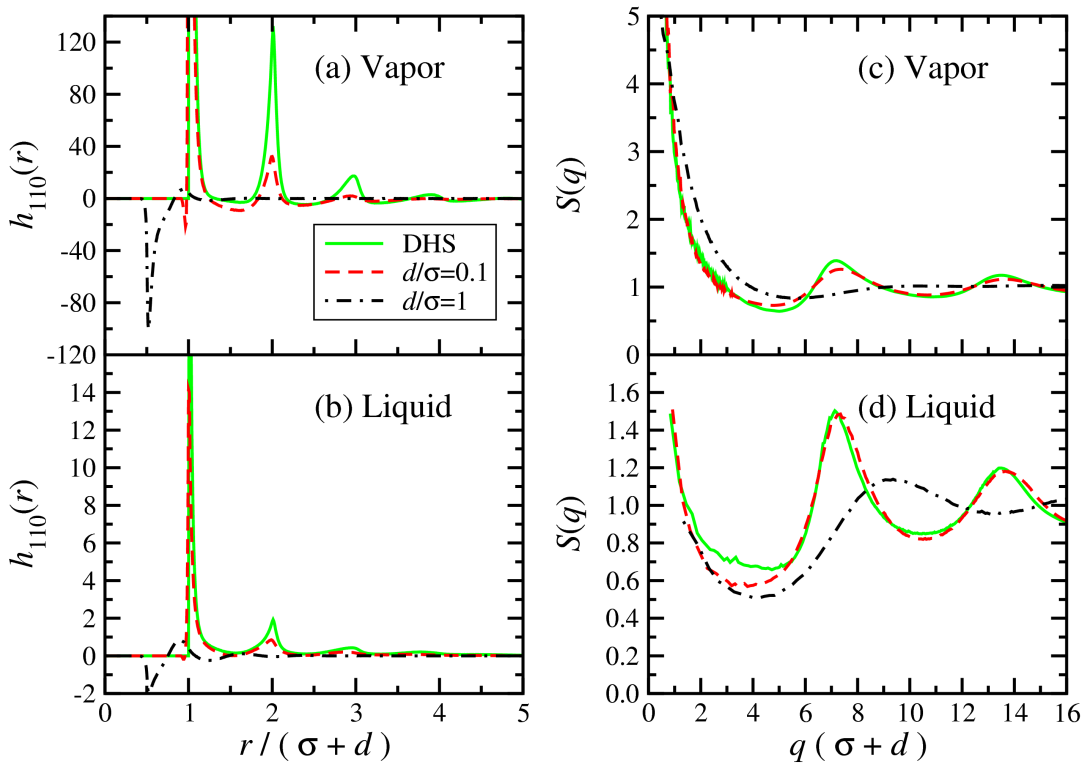

Figure 6.4: $h_{110}(r)$ and $S(q)$ in vapour and liquid phases near coexistence at relative temperature $0.9\tau_c^d$: (a) $h_{110}(r)$ in the vapour phase; (b) $h_{110}(r)$ in the liquid phase; (c) $S(q)$ in the vapour phase; (d) $S(q)$ in the liquid phase. Systems and parameters: CHDs with $d/\sigma = 1$, $\tau^d = 0.0441$, $\rho^*_{\rm vap} = 0.0040$, $\rho^*_{\rm liq} = 0.15$ (black dot-dashed lines); CHDs with $d/\sigma = 0.1$, $\tau^d = 0.126$, $\rho^*_{\rm vap} = 0.0035$, $\rho^*_{\rm liq} = 0.30$ (red dashed lines); DHSs, $\tau^d = 0.138$, $\rho^*_{\rm vap} = 0.0035$, $\rho^*_{\rm liq} = 0.30$ (green solid lines).

As stated in the Introduction, Tlusty and Safran have put forward a mechanism of dipole-driven coexistence based on not only the density difference between the coexisting phases, but also the topologies of the aggregates in the coexisting phases [8]. The low-density chain-like phase is characterised by 'end' defects, particles at the ends of chains with only one near neighbour. The high-density 'network' phase is characterised by

branching points, particles with three near neighbours. To explore this possibility, the fractions of particles with n near neighbours, x_n, have been calculated: x_1 and x_3 signal end and 'Y' defects, respectively. Two particles were assigned as near neighbours if any two spheres on different particles were within a distance 1.1σ. In the CHD system with $d/\sigma = 0.1$, the results for coexisting vapour and liquid phases at relative temperature $0.9\tau_c^d$ are $\{x_1 = 0.42,\ x_3 = 0.02\}$ and $\{x_1 = 0.17,\ x_3 = 0.39\}$, respectively. These are to be compared with results for the DHS system at the same densities and relative temperature $0.9\tau_c^d$ – $\{x_1 = 0.14,\ x_3 = 0.01\}$ in the vapour and $\{x_1 = 0.08,\ x_3 = 0.34\}$ in the liquid. Hence, the simulation results are broadly in line with the scenario proposed by Tlusty and Safran: the dilute phase is rich in 'end' defects, while the dense phase is rich in 'Y' defects.

6.4 Discussion

In summary, vapour-liquid coexistence in CHD fluids shows a crossover between 'ionic' and 'dipolar' regimes. The ionic regime is characterised by isotropic aggregation whereas the dipolar regime features long chains of CHD aligned in 'nose-to-tail' fashion. Severe sampling problems, caused by very strong chaining, were encountered for CHDs with a value of the elongation parameter $d < 0.1$. Still, the structure of the CHD fluid with $d = 0.1$ bears close similarity to that of the DHS fluid, indicating that the dumbbell model used here presents a viable approach for simulating properties of almost dipolar hard spheres with good accuracy. For small values of the dumbbell elongation parameter d, a linear relationship between the critical temperature τ_c^d (in dipolar reduced units) is observed. Extrapolation to the DHS limit yields reduced critical parameters of $\tau_c^d \simeq 0.153$ and $\rho_c^* \simeq 0.1$. Agreement is found between the structure of CHD with small d and the mechanism of phase separation in dipolar fluids proposed by Tlusty and Safran [8]. It is important to emphasise, however, that the agreement between their picture and small-d CHD structural features does not imply that the vapour-liquid transition exists in the limit $d \to 0$; it only provides an insight into what drives phase separation in nearly point dipolar fluids. These findings are therefore in agreement with the study of Yukawa dipolar hard spheres (DYHS: DHS with an attractive isotropic interaction of the Yukawa type) which will be presented in the next chapter: Phase separation can be observed if the Yukawa attraction is larger than a threshold value and the structure of coexisting vapour and liquid phases is in good agreement with Tlusty and Safran's picture. A possible explanation for the absence of a phase transition in pure DHS has been put forward by Miller *et al* [105]: These authors consider a model of charged dumbbells with soft repulsive cores and provide evidence that, for small values of d, the system suffers dynamical arrest, leading to a percolating gel phase at a temperature and density

range where the spinodal line should be located. The existence of a dynamically arrested phase could preempt phase separation from occurring on macroscopic timescales. At the same time, one might argue that the phase transition exists but can only be observed in much larger systems which exclude the possibility of a system-spanning chain, i.e. a chain which is linked with itself via the periodic boundary conditions and thus stabilised, with artificially induced percolation. Clearly, larger system sizes need to be studied in order to exclude this possibility. The next chapter attempts to gain more insight on this matter.

Chapter 7

Vapour-liquid condensation in dipolar hard spheres with attractive Yukawa interaction

7.1 Introduction

The preceding chapter investigated the model of charged hard dumbbells in order to shed light on the question whether or not there exists vapour-liquid separation in dipolar hard spheres (DHS). In that study, the dumbbell elongation d serves as an adjustable parameter which bridges the inter-particle force behaviour between ionic (large d) and dipolar (small d). The crossover behaviour of the phase transition between ionic and dipolar regimes was examined and extrapolation to the DHS limit $d \to 0$ was made, suggesting a vapour-liquid critical point located at $T_c^* \simeq 0.153$ and $\rho_c^* \simeq 0.1$ in dipolar reduced units. However, the reliability of the extrapolation is questionable due to the likely presence of strong finite-size effects. These finite-size effects arise mainly from the fact that DHS form long chains at low temperatures which can be artificially stabilised by the periodic boundary conditions if they reach a system-spanning length. A reliable study of vapour-liquid criticality in DHS thus calls for the simulation of large systems which in turn needs very efficient simulation methods. This chapter attempts to satisfy these requirements by studying so-called dipolar Yukawa hard spheres (DYHS), given by the DHS potential and an additional attractive isotropic Yukawa interaction [see Eq. (5.4)]. This pair potential is computationally cheaper to evaluate than CHD because only one site with long-range interaction has to be considered per particle, as opposed to two for CHD. At the same time, DYHS can bridge between 'normal' condensation,

mediated through isotropic interactions, which occur at large values of the isotropic interaction strength ε_{Y}, and purely dipolar interactions for $\varepsilon_{\mathrm{Y}} \to 0$.

With results for large system sizes, this chapter provides accurate grand-canonical results for phase coexistence and critical points of the DYHS fluid in the limit of vanishing Yukawa interaction strength. Phase diagrams are presented for DYHS with $0 \leq \mu^2/\varepsilon_Y\sigma^3 \leq 36$ while for even higher dipole strengths, only critical points were identified in order to keep the computational effort manageable. The problems of sampling and convergence are tackled by employing biased particle insertions and deletions, with some filtering rules to speed up the identification of unfavourable moves. As well as coexistence data being presented, some comparisons are made between the DHS and DYHS fluids in terms of thermodynamic functions and structural properties. This chapter is organised as follows: The biased sampling scheme is devised in Section 7.2. In Section 7.3 the simulation methods are presented. The results are presented in Section 7.4, and Section 7.5 contains a critical discussion of the results obtained so far. Parts of this work have been published in [106] in affiliation with Prof. G. N. Patey and Dr P. J. Camp, and in [107] in affiliation with Dr Yu. V. Kalyuzhnyi and Dr I. A. Protsykevytch, and Dr P. J. Camp.

7.2 Efficient sampling methods for dipolar hard spheres

The usual formulation of the Metropolis solution to the detailed balance condition [Eq. (1.18), see Section 1.2.1] assumes implicitly that the trial moves leading to displacement or rotation of particles, are chosen randomly from all available possibilities within the entire configurational part of phase space $\mathcal{Q}$ for which the system is defined. This sampling procedure works well for simple systems such as, e.g., a Lennard-Jones fluid at moderate densities, but for more complex models it cannot generate a large number of uncorrelated states within reasonable computer time and will fail to provide accurate statistical expectation values. The cause of this misery is that an unbiased generation of trial moves leads to a large fraction of high energy configurations with a vanishingly small acceptance rate. Therefore, much computation time is wasted with the evaluation of the energy of trial states which do not contribute towards propagating the system through phase space.

It is possible to devise biased sampling schemes which improve computational efficiency by using two different strategies:

1. Variance reduction – The trial move is chosen according to its Boltzmann weight from a subset of proposed moves. Sampling is therefore directed towards important regions of phase space which reduces the statistical error.

2. Early rejection – Trial moves are classified according to their acceptance probability and directly rejected if this probability is below a given threshold, without having to evaluate their computationally expensive full Boltzmann weight.

Both methods can only provide an increase in efficiency if they employ an approximate way of estimating the Boltzmann weight of a trial configuration which is computationally faster to calculate than the true potential used in the Metropolis acceptance criterion[1]. Both schemes can increase the simulation efficiency dramatically by orders of magnitude, thus rendering feasible problems which are otherwise prohibitive in their computational demands. For historical reasons, the name associated with the variance reduction method is the *Rosenbluth* scheme which will be henceforth used. This section will describe both the Rosenbluth scheme and the early rejection method for the generation of biased trial moves of strongly interacting dipolar particles.

7.2.1 Generation of biased trial moves

In the Rosenbluth scheme, trial moves are generated approximately in accordance with the limiting Boltzmann probability distribution of the Monte Carlo Markov chain. The Metropolis sampling algorithm Eq.(1.18) thus rarely has to reject a proposed move and the Markov chain quickly propagates through phase space. The trial move generating process can be formally introduced by decomposing the stochastic transition matrix $\underline{\boldsymbol{\Pi}}$ (Section 1.2.1) into a Hadamard product[2] of two separate matrices,

$$\underline{\boldsymbol{\Pi}} = \underline{\boldsymbol{acc}} \cdot \underline{\boldsymbol{\alpha}} \tag{7.1}$$

where $\underline{\boldsymbol{acc}}$ is a matrix of Boltzmann transition probabilities and $\underline{\boldsymbol{\alpha}}$ is a matrix describing the probabilities of what trial move to generate. Inserting this definition of $\underline{\boldsymbol{\Pi}}$ into the Metropolis solution to the detailed balance condition, Eq. (1.18), one finds the

[1] This is strictly only true for if rigid particles are simulated. In the case of flexible multi-segment particles like polymers, the variance reduction method can employ the true potential for biasing the placement of the individual segments separately and achieve a significant increase in efficiency[108].

[2] The Hadamard product is also known as the entrywise Schur product and is defined for two matrices $\underline{\boldsymbol{A}}, \underline{\boldsymbol{B}}$ of the same dimensions as $(\underline{\boldsymbol{A}} \cdot \underline{\boldsymbol{B}})_{ij} = A_{ij}B_{ij}$. It is commutative, unlike matrix multiplication.

acceptance rule

$$\begin{aligned} \Pi_{on} P_o &= \Pi_{no} P_n \\ acc_{on}\alpha_{on} P_o &= acc_{no}\alpha_{no} P_n \\ &\therefore \\ acc(o \to n) &= \min\left[1, \frac{P_n}{P_o} \cdot \frac{\alpha_{no}}{\alpha_{on}}\right] \end{aligned} \tag{7.2}$$

which will converge towards the limiting Boltzmann distribution, independent of $\underline{\boldsymbol{\alpha}}$. It is clear from the above equation, that if $\alpha_{ij} = P_j$, all proposed trial moves will be accepted. A practical implementation of the Rosenbluth sampling scheme will therefore strive to generate trial moves according to the target Boltzmann distribution. In the crudest fashion, this can be realised by generating a set of K trial candidate configurations $\mathbf{\Gamma} \in \{\mathbf{\Gamma}_1, \mathbf{\Gamma}_2, ..., \mathbf{\Gamma}_K\}$ and selecting one $\mathbf{\Gamma}_j$ from this set according to its Boltzmann weight calculated with some approximate, computationally cheap energy function $U(\mathbf{\Gamma})$.

$$\alpha_{ij} = \frac{\exp\left[-\beta U(\mathbf{\Gamma}_j)\right]}{\sum_{k=1}^{K} \exp\left[-\beta U(\mathbf{\Gamma}_k)\right]} \tag{7.3}$$

It may come somewhat as a surprise that the results obtained with a biasing scheme which employs an approximate energy function and furthermore only samples K discrete trial configurations still obey the correct limiting Boltzmann distribution. However, we can easily check the requirements for a correct Markov chain. As detailed balance is obeyed by construction in Eq. (7.2), it only needs to be verified that $\underline{\boldsymbol{acc}}$ and $\underline{\boldsymbol{\alpha}}$ are row-stochastic matrices. Due to the commutative property of the Hadamard product this can be done separately for each matrix and the following shows that $\underline{\boldsymbol{\alpha}}$ is indeed row-stochastic, regardless of the value of K:

$$\begin{aligned} \sum_{j=1}^{K} \alpha_{ij} &= \sum_{j=1}^{K} \frac{\exp\left[-\beta U(\mathbf{\Gamma}_j)\right]}{\sum_{k=1}^{K} \exp\left[-\beta U(\mathbf{\Gamma}_k)\right]} \\ &= 1 \end{aligned} \tag{7.4}$$

Given that $\underline{\boldsymbol{\alpha}}$ is row-stochastic, construction of the matrix elements acc_{on} via the detailed balance condition ensures that $\underline{\boldsymbol{acc}}$ is row-stochastic as well.

7.2.2 Early rejection scheme

The local environment of strongly interacting particles is often characterised by very narrow distributions, in terms of how neighbours are geometrically arranged. Most randomly generated Monte Carlo trial moves will therefore not be accepted as they have a low probability of being generated in accordance with the local environment.

Using the Swendsen-Wang (SW) scheme [109, 110], it is possible to classify trial moves according to an *a priori* criterion and directly reject moves with a probability depending on this criterion. For example, if it is known that almost all particles in a system have a minimum nearest neighbour interaction energy $U_{\mathrm{nn}} \leq U_{\mathrm{min}}$, then typically one would like to skip evaluation of an expensive pair potential with all particles if the computationally cheap nearest neighbour interaction energy is greater than U_{min}. Formally, the SW scheme can be introduced as transition probabilities into the detailed balance condition [111]:

$$\begin{aligned} acc_{on}\alpha_{on}^{\mathrm{SW}}P_o &= acc_{no}\alpha_{no}^{\mathrm{SW}}P_n \\ acc(o \to n) &= \min\left[1, \frac{P_n}{P_o}\cdot\frac{\alpha_{no}^{\mathrm{SW}}}{\alpha_{on}^{\mathrm{SW}}}\right] \end{aligned} \tag{7.5}$$

The factor $\alpha_{no}^{\mathrm{SW}}/\alpha_{on}^{\mathrm{SW}}$ can be taken to be a step function depending on the energy difference $\Delta\tilde{U}_{on}$ between $\mathbf{\Gamma}_o$ and $\mathbf{\Gamma}_n$, calculated with an approximate, computationally effective pair potential $\tilde{U}(\mathbf{\Gamma})$:

$$\begin{aligned} \frac{\alpha_{no}^{\mathrm{SW}}}{\alpha_{on}^{\mathrm{SW}}} &= \Theta(\Delta\tilde{U}_{on}) \\ &= \begin{cases} 1 & \text{if } \Delta\tilde{U}_{on} \leq U_{\mathrm{min}} \\ 0 & \text{reject according to some fixed probability} \end{cases} \end{aligned} \tag{7.6}$$

There is considerable freedom as to which rejection criterion to use. A straightforward way is to decide on an approximate energy function, e.g., only the real-space energy if the Ewald summation technique is used, and to run an unbiased simulation, keeping track of the average energy change of a successful MC move. A certain percentage threshold of this average energy can then be used as the *a priori* criterion for the biased simulation involving SW filtering rules.

7.2.3 Application to grand-canonical simulation of strongly dipolar fluids

Simulations in the grand-canonical ensemble rely on particle insertions and deletions, and so sampling becomes very difficult at low temperatures where practically all particles are part of a stiff polymer-like network. The orientation of each dipole is strongly influenced by the local electric field, which is dominated by contributions from its near neighbours. Any unbiased insertion algorithm that generates trial positions and orientations at random will therefore be highly ineffective because the probability of appending a new particle to an existing chain in just the right position and orientation is low.

Similarly, random deletion moves will fail in most cases because the majority of particles are part of linear chains and huge energetic penalties are associated with breaking these favourable conformations. An effective insertion/deletion algorithm must therefore meet the following requirements: for insertions, dipole orientations must be chosen in accordance with the local electric field and particles should preferably be appended to existing chains; deletions should preferably remove particles from the ends of existing chains.

Caillol has given a solution to the orientational problem [5] for the Gibbs and NVT ensembles. This solution was adapted for the grand-canonical ensemble to facilitate the simulations reported in Ref. [106]. As the interaction energy of a chosen dipole $\boldsymbol{\mu}$ with other dipoles is given by $U = -\boldsymbol{\mu} \cdot \boldsymbol{E}$, where $\boldsymbol{E}$ is the local electric field at the position of the chosen dipole, the Boltzmann factor for a given orientation relative to the direction of $\boldsymbol{E}$ is

$$\exp(\beta \boldsymbol{\mu} \cdot \boldsymbol{E}) \tag{7.7}$$

and the Boltzmann probability distribution function of enclosed angles θ between $\boldsymbol{\mu}$ and $\boldsymbol{E}$ is:

$$\begin{aligned} P(\theta) &= \frac{\exp\left[-\beta|\boldsymbol{\mu}||\boldsymbol{E}|\cos(\theta)\right]}{\int_0^\pi \exp\left[-\beta|\boldsymbol{\mu}||\boldsymbol{E}|\cos(\theta)\right]\sin(\theta)\mathrm{d}\theta} \\ &= \frac{\exp\left[\beta|\boldsymbol{\mu}||\boldsymbol{E}|\cos(\theta)\right]}{\left(e^{2\beta|\boldsymbol{\mu}||\boldsymbol{E}|}-1\right)e^{-\beta|\boldsymbol{\mu}||\boldsymbol{E}|}/(\beta|\boldsymbol{\mu}||\boldsymbol{E}|)} \end{aligned} \tag{7.8}$$

The fact that the integral which appears in the definition of $P(\theta)$ can be worked out analytically allows for the significant advantage that a trial orientation can be drawn directly from the correct distribution through inversion of the cumulative distribution function of $P(\theta)$ as discussed in Appendix A. To do this, it is sufficient to generate a random number R uniformly on $[0, 1]$ and obtain the enclosed angle from

$$\cos(\theta) = \frac{1}{\beta|\boldsymbol{\mu}|\boldsymbol{E}|} \ln\left[2R\sinh\left(\beta|\boldsymbol{\mu}||\boldsymbol{E}|\right) + \exp\left(-\beta|\boldsymbol{\mu}||\boldsymbol{E}|\right)\right]. \tag{7.9}$$

Therefore, it is not necessary to generate a set of trial orientations as discussed above for the Rosenbluth scheme. Because the direction of the electric field is dominated by the local environment, it is computationally economic and relatively accurate to estimate $\boldsymbol{E}$ using only the nearest neighbours at the position of the particle which is to be inserted/deleted. [106], using only the particles located in a central cell and its 26 immediate neighbouring cells to compute $\boldsymbol{E}$.

No highly effective biasing scheme is available to solve the the problem of appending and deleting particles from existing chains. Nonetheless, SW filter rules can be employed to

increase the simulation convergence rate by a large factor. Crucial to the SW scheme is that a quick and sufficiently accurate predictor for the acceptance of a proposed move is available. For strongly dipolar particles, a good predictor is based on the scalar product of the dipole vector and the approximate local electric field at the insertion/deletion position.

As shown in Ref. [58], it is also beneficial to attempt insertions with a higher frequency than deletions for dipolar particles in conjunction with the SW filtering scheme. This can be understood by noting that random insertions will rarely generate a configuration with a high Boltzmann weight resulting in a large fraction of early rejections. Deletions, on the other hand, take place among existing configurations which by definition are energetically favourable resulting in very few early rejections.

The Metropolis acceptance probabilities for insertion ($N \to N+1$) and deletion ($N \to N-1$) – taking in to account the SW filter, orientational biasing, and increased insertion probability – are thus given by

$$acc_{(N\to N+1)} = \min\left[1, \Theta(|\boldsymbol{\mu}||\boldsymbol{E}|\cos\theta)\frac{1-p_{\rm ins}}{p_{\rm ins}}\frac{1/2}{P(\theta)}\frac{zVe^{-\beta\Delta U}}{N+1}\right] \tag{7.10}$$

$$acc_{(N\to N-1)} = \min\left[1, \Theta(|\boldsymbol{\mu}||\boldsymbol{E}|\cos\theta)\frac{p_{\rm ins}}{1-p_{\rm ins}}\frac{P(\theta)}{1/2}\frac{Ne^{-\beta\Delta U}}{zV}\right] \tag{7.11}$$

where $\Theta(|\boldsymbol{\mu}||\boldsymbol{E}|\cos\theta)$ is the SW filtering rule, $p_{\rm ins}$ is the probability of attempting an insertion, $P(\theta)$ is the biasing probability associated with generating an orientation in accordance with the local electric field and the factors of $1/2$ result from $P(\theta)$ for the creation/destruction of particles in the ideal gas reservoir connected to the simulation box.

Comparison of the above biased sampling scheme to dipolar hard spheres with a completely unbiased *GCMC* simulation [using the Monte Carlo acceptance rule Eq. (1.25)] serves to demonstrate the correctness of the acceptance rules Eq. (7.11). Simulation convergence was monitored by calculating the density-density autocorrelation function $C(\tau) = \langle \delta\rho(\tau)\delta\rho(0)\rangle$ where $\delta\rho(\tau) = \rho(\tau) - \langle\rho\rangle$ and τ is the simulation CPU time. The decay times for $C(\tau)$ with the sampling scheme outlined here are roughly decreased by a factor of three for a small system with $V = 512\sigma^3$ whereas a larger system with $V = 1000\sigma^3$ already shows a factor of 10 in efficiency increase when compared with unbiased simulations (see Fig. 7.1). This scaling with system size reflects that the evaluation of the pair potential requires CPU time proportional to the square of the system size and that a significant fraction of 'bad' trial moves are skipped by the Swendsen-Wang filter. The results reported here used the biased sampling scheme with an enhanced insertion probability of $p_{\rm ins} = 0.95$, a SW energy cutoff of $E^*_{\rm min} = -1.25$ (in reduced units, see Sec. 7.3) and the approximate local electric field was computed by employing

a spatial cell decomposition with width 1.25σ of the simulation box, summing only over particles contained within the cell centred at the insertion/deletion position and its 26 immediate neighbouring cells.

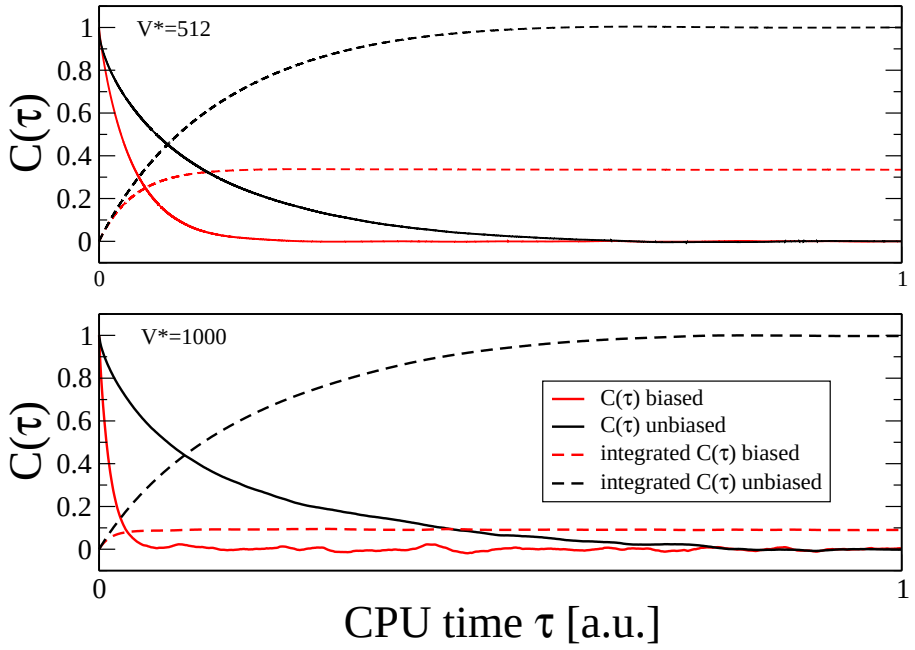

Figure 7.1: Number density time autocorrelation function $C(\tau)$ for biased and unbiased $GCMC$ simulation of dipolar hard spheres. The autocorrelation time is proportional to the long-time limit of the integral of $C(\tau)$.

7.3 Simulation details

The DYHS potential is given in Eq. (5.4). Reduced units are defined in the conventional way: reduced temperature $T^* = k_\mathrm{B}T\sigma^3/\mu^2$; reduced Yukawa energy parameter $\varepsilon_\mathrm{Y}^* = \varepsilon_\mathrm{Y}\sigma^3/\mu^2$; reduced dipolar interaction parameter $(\mu^*)^2 = \mu^2/\varepsilon_\mathrm{Y}\sigma^3 = 1/\varepsilon_\mathrm{Y}^*$; reduced number density $\rho^* = \rho\sigma^3$. With such a definition for ε_Y^*, the DHS limit corresponds to $\varepsilon_\mathrm{Y}^* = 0$.

$GCMC$ and NVT simulations of the DYHS fluid were performed in a cubic box of volume $V = L^3$, with periodic boundary conditions applied [16, 18]. The box lengths spanned the range $10 \leq L/\sigma \leq 22.5$, depending on the other system parameters. The long-range dipolar interaction was handled using the Ewald summation method with conducting boundary conditions; the screening parameter was taken to be $\alpha L = 6$,

and the reciprocal space vectors were restricted to the domain $|\boldsymbol{k}| \leq 6 \times 2\pi/L$. The calculation of real-space interactions used lookup tables with Newton-Gregory forward interpolation [18], and the trigonometric functions that appear in the reciprocal-space Ewald sum were efficiently vectorised using Intel's optimised Math Kernel Library. For the Yukawa potential, a long-range correction was applied in the normal way by assuming that $g(r) = 1$ for $r > L/2$. The phase diagrams to be presented in Section 7.4.1 were obtained with the GC-WLEXT flat histogram sampling method at fixed temperature as described in Section 2.2.3. For the determination of the critical points shown in Sec. 7.4.2, *GCMC* simulations were employed using the biased sampling scheme as detailed in Sec. 7.2. The pair correlation functions shown in Section 7.4.4 were obtained from *NVT* simulations which employed a simultaneous translation/rotation move with the displacement chosen at random and the orientation at the new position generated according to Eq. (7.8).

7.4 Results

7.4.1 Phase diagrams

Phase diagrams for the DYHS fluid with $\varepsilon_{\mathrm{Y}}^{*} = \{1/4, 1/9, 1/16, 1/25, 1/36\}$ and one system size $L^{*} = 10$ are shown in Fig. 7.2. Coexistence data were fitted with the truncated Wegner-type expansions,

$$\rho_{\pm} = \rho_c \pm (A_0 t^{\beta} + A_1 t^{\beta+\theta}) + (B_0 t^{1-\alpha} + B_1 t) + \ldots \tag{7.12}$$

where $\alpha = 0.11$, $\beta = 0.326$, and $\theta = 0.54$ are the usual Ising critical exponents [112], ρ_{+} and ρ_{-} are the liquid and vapour coexistence densities, respectively, and $t = |T - T_c|/T_c$. Fig. 7.3 compares the shape of the phase diagrams on a corresponding-states plot. A clear trend to a wider coexistence envelope towards the DHS limit is apparent, however, this might just reflect the fact that finite-size effects become more important in this limit. One finds in general that the coexistence densities are shifted inward towards the mean density as system size is increased [113].

7.4.2 Critical points

For values of the interaction parameter $\varepsilon_{\mathrm{Y}}^{*} < 1/36$, the computational effort needed to accumulate accurate statistics becomes so high that it is not practicable to obtain the critical parameters by fitting a universal scaling function to coexistence densities obtained at several temperatures. Instead, an alternative approach was taken by using the

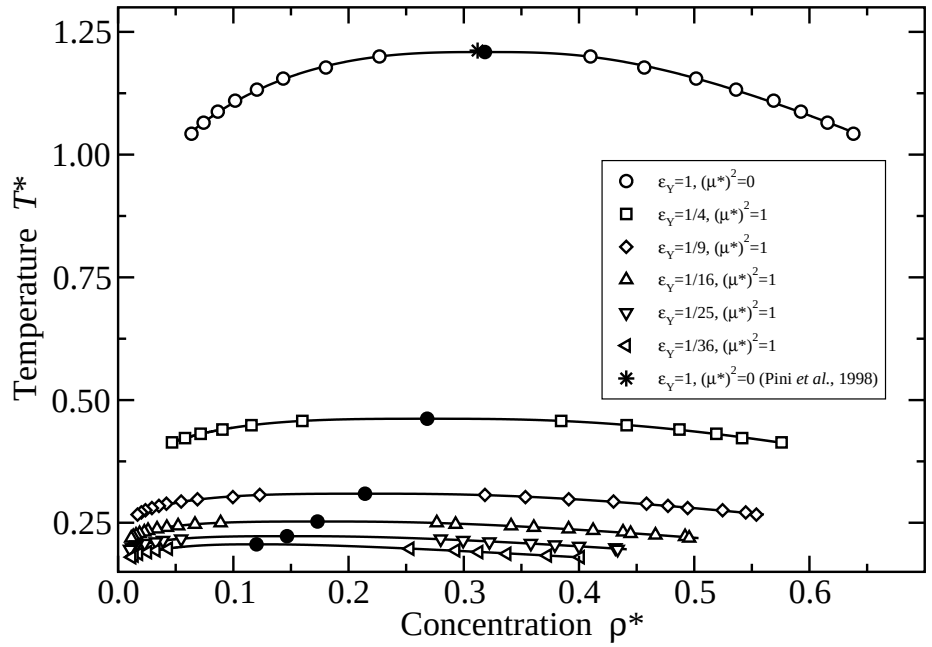

Figure 7.2: Phase diagrams for DYHS with different ε_{Y}.

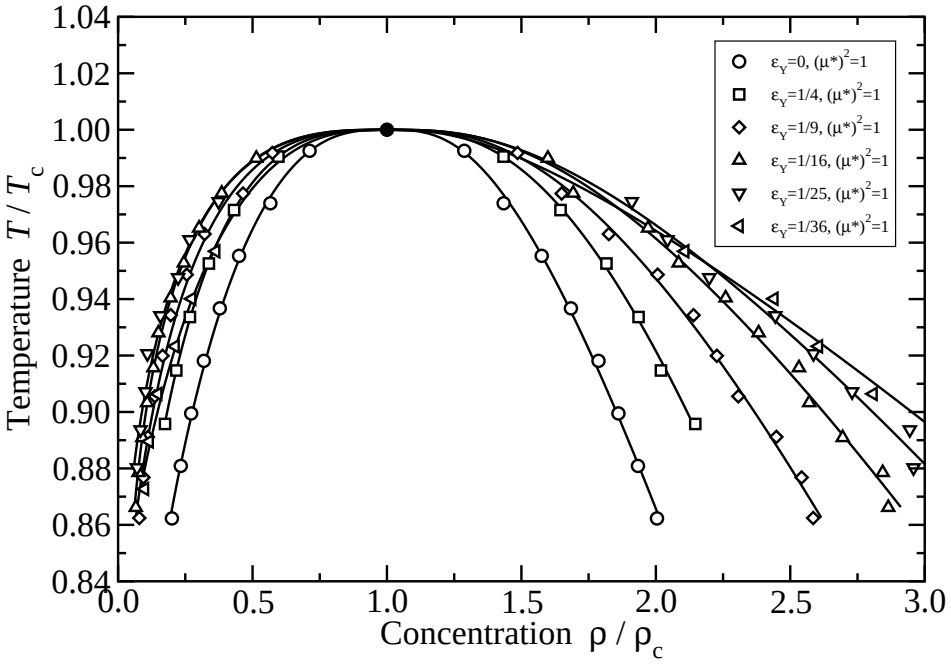

Figure 7.3: Corresponding state phase diagrams for DYHS with different ε_{Y}.

Table 7.1: Critical parameters for the DYHS fluid. The critical temperatures T_c were determined by finite-size scaling (FSS) fits to results from simulations with the box lengths L indicated; the critical densities ρ_c^* are those from simulations with the largest box lengths. For comparison, the critical parameters as obtained from fitting the truncated Wegner type expansions (see Sec. 7.4.1, Eq. (7.12) to the phase diagrams for $L^* = 10$ are also shown. Note that there are no FSS estimates for the system with $\varepsilon_{\mathrm{Y}}^* = 0.0278$. Results are also shown for the apolar Yukawa hard sphere fluid, corresponding to $(\mu^*)^2 = 0$ [107, 114]. For comparison with the Stockmayer fluid results in Section 4.2.3, the ratio of dipolar to isotropic interaction strength is also expressed in a set of units with $\varepsilon_{\mathrm{Y}}^*$ fixed at unity and the dipole moment scaled accordingly (col. 3).

$\varepsilon_{\mathrm{Y}}^*$	T_c^*	$(\mu^*)^2$	$k_{\mathrm{B}}T_c/\varepsilon_{\mathrm{Y}}$	ρ_c^*	L/σ
0.0125	0.16660(27)	80	13.328(22)	0.0907	15, 17.5, 20, 22.5
0.01875	0.186493(49)	53.3333	9.9463(26)	0.1021	15, 17.5, 20, 22.5
0.025	0.19966(12)	40	7.9862(50)	0.1143	15, 17.5, 20, 22.5
0.0278	0.2061(46)	36	7.42(17)	0.1201(39)	10 (Wegner type fit)
0.04	0.222423(95)	25	5.5606(24)	0.1392	15, 17.5, 20
0.04	0.2227(23)	25	5.567(58)	0.1465(33)	10 (Wegner type fit)
0.0625	0.251456(65)	16	4.0233(10)	0.1687	10, 15, 17.5
0.0625	0.25255((65)	16	4.041(10)	0.1730(23)	10 (Wegner type fit)
0.11111	0.30802(13)	9	2.7722(12)	0.2149	10, 15, 17.5
0.11111	0.30921(66)	9	2.7829(59)	0.2143(15)	10 (Wegner type fit)
0.25	0.46203(41)	4	1.8481(16)	0.2665	10, 15, 17.5
0.25	0.46190(54)	4	1.8476(22)	0.2682(15)	10 (Wegner type fit)
		0	1.2090(18)	0.3184(18)	10 (Wegner type fit)
		0	1.212(2)	0.312(2)	9 – 21 (Ref. [114])

mixed-field finite-size scaling method introduced by Bruce and Wilding [115]. Briefly, at the apparent finite-size critical point, the probability distribution of the ordering operator $\mathcal{M} = \rho - su$, (where $u = U/V$ is the energy density) falls on to a universal scaling curve, which was assumed to be that of the three-dimensional Ising model $p_{\mathrm{Ising}}(\mathcal{M})$ [116]. (Note that 'dipolar' criticality has been stated as belonging to a distinct universality class [15] but that the exponents, and presumably the critical ordering-operator distribution, differ only minutely from the Ising results. In any case, the matching of the bimodal distribution serves as a pragmatic means of locating a critical point [117].) *GCMC* simulations were performed at near-critical conditions where bimodal distributions of the particle number were observed. For each system, up to 100 independent simulations were performed and the joint probability distributions $p(N, U)$ were measured. The results were combined using multiple histogram reweighting [118] in order to find the temperature, chemical potential, and non-universal parameter s that provide the best fit to the universal distribution $p_{\mathrm{Ising}}(\mathcal{M})$. The apparent finite-size critical temperatures $T_c(L)$ then scale like

$$T_c(L) - T_c \propto L^{-(\theta+1)/\nu} \tag{7.13}$$

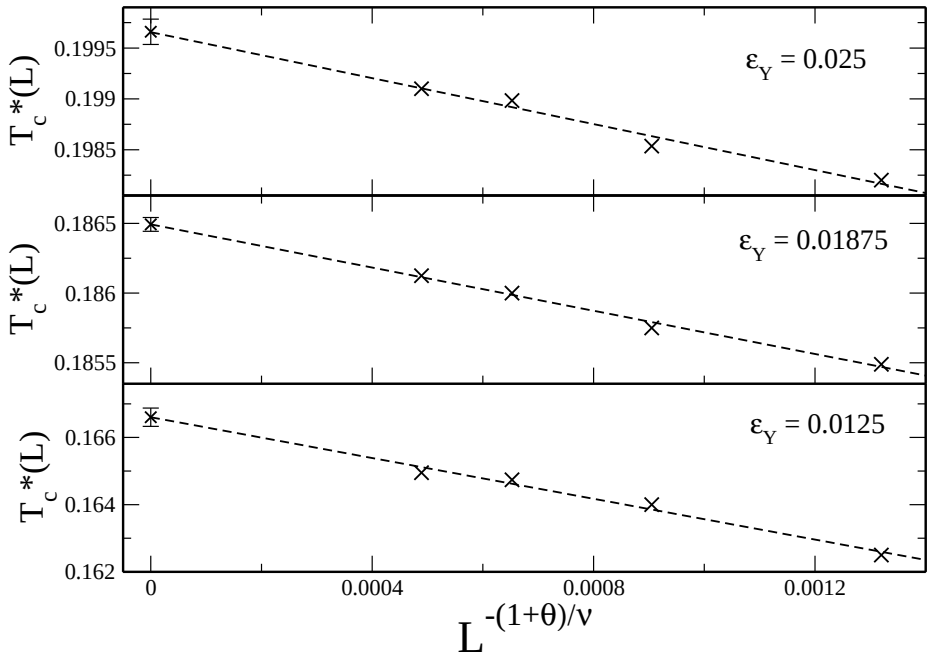

Figure 7.4: MFFSS plots for the apparent finite-size critical temperature plotted against $L^{-(1+\theta)/\nu}$ for systems with $\varepsilon_{\rm Y}^* = 0.0125$, 0.01875, and 0.025. The points are from simulations, and the lines are fits from Eq. (7.13).

where $\theta = 0.54$ and $\nu = 0.6294$ are the correction-to-scaling and correlation-length exponents, respectively, for the (assumed) three-dimensional Ising universality class. Examples of MFFSS plots are shown in Fig. 7.4 for systems with $\varepsilon_{\rm Y}^* = 0.0125$, 0.01875, and 0.025; in each case, the system sizes considered were $L/\sigma = 15$, 17.5, 20, and 22.5. The uncertainties in T_c^* quoted in Table 7.1 are associated with the fitting procedure, and not with systematic errors from any other source. The critical densities showed almost no meaningful finite-size dependence, and so the values reported in Table 7.1 are simply those for the largest systems simulated. Note that it was possible to observe a vapour-liquid critical point for dipolar interaction strengths almost two orders of magnitude greater than the Yukawa energy parameter $\varepsilon_{\rm Y}$.

Fig. 7.5 shows a plot of the dipolar critical temperatures T_c^* against $\varepsilon_{\rm Y}^*$. With smaller values of $\varepsilon_{\rm Y}^*$, T_c^* follows a sub-linear variation. It was found heuristically that the simulation data could be fitted with a simple function of the form

$$T_c^*(\varepsilon_{\rm Y}^*) = A\varepsilon_{\rm Y}^* + B + C\arctan(D\varepsilon_{\rm Y}^*). \tag{7.14}$$

There is no physical justification for this choice of function, but the combination of a simple saturation function and a linear term does fit the simulation data very well:

the fit parameters are $A = 1.0894(24)$, $B = -34.12060(24)$, $C = 21.84370(15)$, and $D = 45907(571)$. (Note, though, that the value of A represents the extrapolated value of $k_{\mathrm{B}}T_c/\varepsilon_{\mathrm{Y}}$ at $(\mu^*)^2 = 0$, and that it deviates from the actual values of approximately 1.21 given in Table 7.1.) A naïve extrapolation of the fitted function suggests that the critical temperature reaches zero at $\varepsilon_{\mathrm{Y}}^* \simeq 0.0025$, implying that there is no phase separation in the DHS limit ($\varepsilon_{\mathrm{Y}}^* = 0$). Attempts were made to find the vapour-liquid critical point in a system with $\varepsilon_{\mathrm{Y}}^* = 0.01$, for which Eq. (7.14) predicts that $T_c^* \simeq 0.155$; simulations as far down as $T^* = 0.135$ did not show any sign of phase separation.

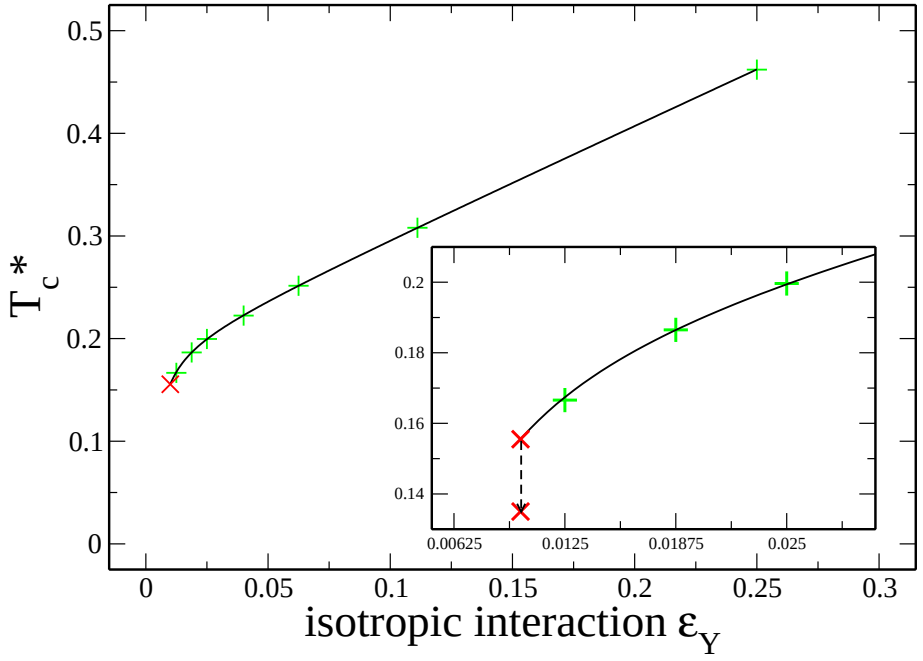

Figure 7.5: Critical temperature T_c^* against the Yukawa energy parameter $\varepsilon_{\mathrm{Y}}^*$. Pluses are the FSS data from Table 7.1. The solid line is the fit from Eq. (7.14). The crosses indicates simulation results at $\varepsilon_{\mathrm{Y}}^* = 0.01$ for which no phase separation could be observed. Inset: Enlargement of the region of highest curvature to show the quality of the fit. No phase separation could be observed in the temperature range $T^* = [0.155, 0.135]$ at $\varepsilon_{\mathrm{Y}}^* = 0.01$.

The critical density ρ_c^* against $\varepsilon_{\mathrm{Y}}^*$ is shown in Fig. 7.6. The data points for $\varepsilon_{\mathrm{Y}}^* < 0.05$ appear to fall on a straight line, and a fit to the equation $\rho_c^*(\varepsilon_{\mathrm{Y}}^*) = A + B\varepsilon_{\mathrm{Y}}^*$ yields the parameters $A = 0.0693(16)$ and $B = 1.776(60)$. A is an estimate of the critical density of DHSs, in good agreement with the results for the charged hard dumbbells, Chapter 6, and the work of Almarza *et al* [100].

A discussion of the significance of these results is postponed until Section 7.5, before which results for the thermodynamic and structural properties will be presented.

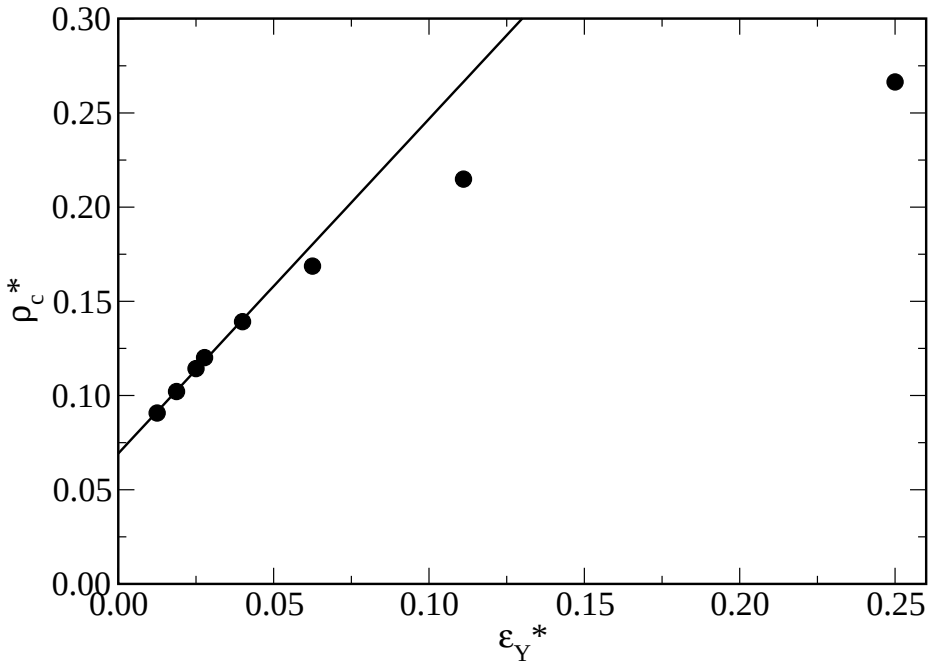

Figure 7.6: Critical density ρ_c^* against $\varepsilon_{\rm Y}^*$. The solid points are the data from Table 7.1. The solid line is a linear fit to the data for $\varepsilon_{\rm Y}^* < 0.05$.

7.4.3 Thermodynamics

It is interesting to ask how such small values of the Yukawa energy $\varepsilon_{\rm Y}$, almost two orders of magnitude smaller than the characteristic dipolar energy μ^2/σ^3, have such a strong effect on whether a vapour-liquid transition can be seen in computer simulations. To examine the role of the energy, NVT MC simulations of $N = 1024$ particles were conducted for the DHS fluid, and for a DYHS fluid with $\varepsilon_{\rm Y}^* = 0.0125$ (the smallest value for which the transition can still be observed in simulations). For the purposes of comparison, a single isotherm with $T^* = 0.15$ was considered; this is about 10% below the critical temperature for the DYHS system, and about 2% below the putative critical temperature for DHSs, $T_{c,DHS}^* \simeq 0.153$. The potential energies as functions of the reduced density ρ^* are shown in Fig. 7.7. The potential energy for DHSs levels off for densities $\rho^* \geq 0.1$, but over the range considered, the variations are only on the order of $0.1 k_{\rm B}T$ per particle. For the DYHS system, two sets of data are shown: the total energy – dipolar plus Yukawa – which drops by about $0.3 k_{\rm B}T$ per particle in the range $0.025 \leq \rho^* \leq 0.3$; and the dipolar energy only, which mirrors that of the pure DHS fluid quite closely.

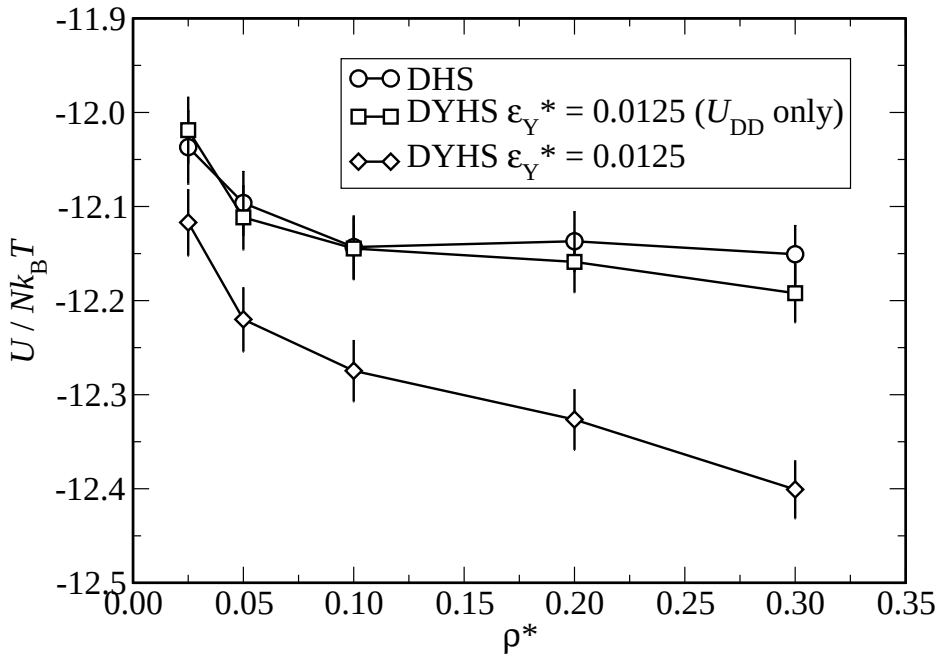

Figure 7.7: Potential energy per particle in units of $k_{\mathrm{B}}T$ as a function of the reduced density ρ^*, at a fixed temperature $T^* = 0.15$. The circles are for pure DHSs. The squares represent the *dipolar energy only* for a DYHS fluid with $\varepsilon_{\mathrm{Y}}^* = 0.0125$ (the lowest value for which phase separation is observable); the diamonds represent the *total energy* (dipolar plus Yukawa) for the same system.

It is also of interest to ask in which way the isotropic interaction part of the energy is responsible for the phase separation mechanism. For this, it is instructive to look at the Zwanzig expression for a free energy perturbation:

$$\Delta F = -k_B T \ln \left\langle \exp\left[-\beta(\mathcal{H}' - \mathcal{H}_0)\right]\right\rangle_0 \tag{7.15}$$

Here, $\mathcal{H}'$ refers to the perturbed Hamiltonian while $\mathcal{H}_0$ is the Hamiltonian corresponding to the ensemble over which the average is taken. Application of Eq. (7.15) to ensemble averages obtained from finite computer simulation amounts to a first-order perturbation theory as the free energy perturbation is only evaluated using configurations characteristic of the original Hamiltonian. Starting from an original Hamiltonian which incorporates a high enough value of ε_{Y} such that phase separation is observed, one would expect the Zwanzig expression to predict vanishing phase separation as ε_{Y} is reduced *if only the energetic contribution of the isotropic interaction energy is responsible for phase separation.* Fig. 7.8 shows number density probability distributions $P(N)$ for a system simulated using a Hamiltonian $\mathcal{H}_0$ with $\varepsilon_{\mathrm{Y}}^* = 0.04$ and perturbed $\mathcal{H}'$ with $\varepsilon_{\mathrm{Y}}^* = [0, 0.08]$. It is obvious that the changes due to different ε_{Y} only have very minor effects which

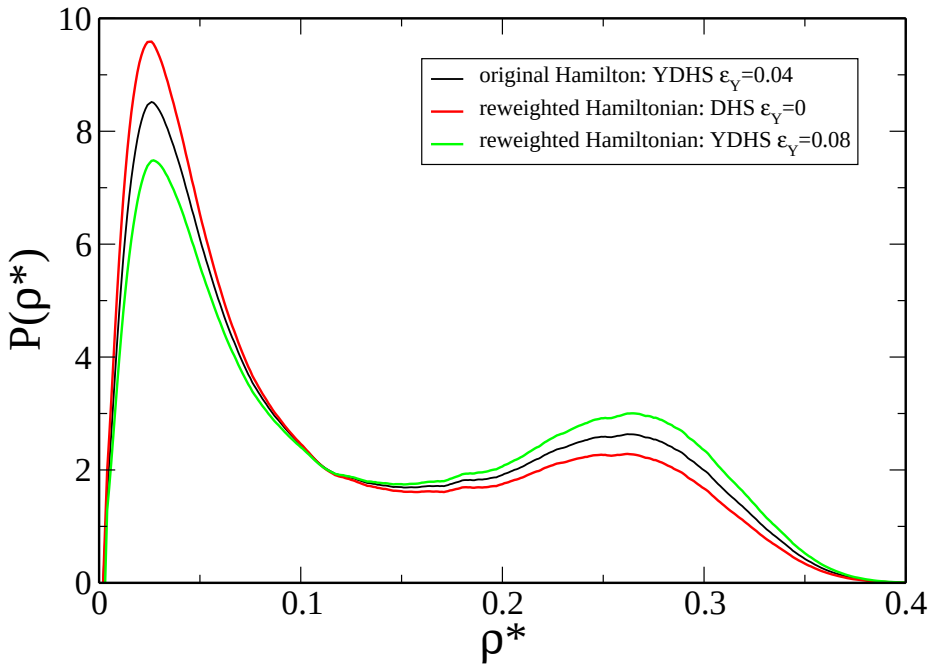

Figure 7.8: Reweighted number density probability distributions: Distributions for $\varepsilon_{\mathrm{Y}}^{*} = 0$ and $\varepsilon_{\mathrm{Y}}^{*} = 0.08$ were obtained by histogram reweighting of the original distribution. The simulation was conducted at $T^{*} = 0.22$, $\mu^{*} = -1.17553$, $\varepsilon_{\mathrm{Y}}^{*} = 0.04$ using a box with $V* = 1000$.

allows to unambiguously conclude that the role of the isotropic interaction energy is to induce structural changes which lead to phase separation.

In the classical picture of vapour-liquid phase separation, the vapour phase is of high energy, high enthalpy, and high entropy, while the liquid phase is of low energy, low enthalpy, and low entropy. The temperature-driven transition at fixed pressure is therefore dictated by balances of enthalpy and entropy. The pressure at low temperature is anomalously low (a consequence of strong clustering) and so the addition of the PV term to the energy is not going to change the picture very much; a further variation of 0.1-0.2$k_{\mathrm{B}}T$ per particle over the density range considered is all that is to be expected [65]. It is clear that the classical picture does not apply to DHSs, and it is questionable whether it is relevant for the DYHS system either. Alternative scenarios include the defect-driven mechanism proposed by Tlusty and Safran [8]. The relevant structural properties of the DHS and DYHS fluids will be discussed next.

7.4.4 Pair correlation functions

Fig. 7.9 shows the projections of the molecular pair correlation function on to rotational invariants [20, 84], determined from canonical MC simulations with $N = 1024$ particles. Two systems are considered, the DHS fluid and the DYHS fluid with $\varepsilon_{\mathrm{Y}}^{*} = 0.0125$, at reduced densities of $\rho^{*} = 0.025$ and 0.3 and at the same dipolar temperature $T^{*} = 0.15$ (as in Section 7.4.3). In order to bring the results for dilute and concentrated phases on to the same scale, the functions $h_{l_1 l_2 m}(r)$ are multiplied by ρ^{*}. Fig. 7.9(a) shows the total pair correlation function $h_{000}(r) = h_{000}(r) - 1$. The essential point is that for a given density, the results for the DHS and DYHS fluids are almost identical, the only noticeable difference being that the peaks are slightly higher and the troughs are slightly shallower in the DYHS fluid than in the DHS fluid; presumably this can be put down to the additional isotropic attraction. For the most part, all of the remaining projections shown in Fig. 7.9(b)-(d) exhibit similar features. $h_{112}(r)$ shows a more pronounced deviation between the DHS and DYHS results at high concentration. This projection mirrors the dipolar interaction potential, and the DYHS system seems to possess longer-range correlations of this type. This explains the slightly lower dipolar energy for the DYHS system shown in Fig. 7.7. As expected, the functions $h_{110}(r)$ and $h_{220}(r)$ rapidly decay to zero meaning that there is no ferroelectric or nematic ordering at these low densities.

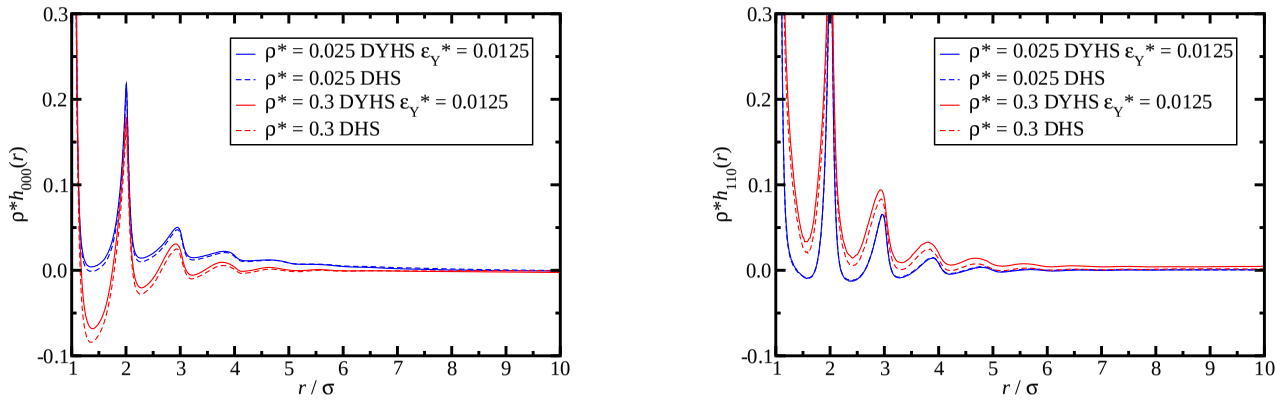

(a) $\rho^* h_{000}(r)$ (b) $\rho^* h_{110}(r)$

(c) $\rho^* h_{112}(r)$ (d) $\rho^* h_{220}(r)$

Figure 7.9: Total correlation functions $h_{l_1 l_2 m}(r)$ [20, 84] for the DHS fluid and the DYHS fluid with $\varepsilon_{\mathrm{Y}}^* = 0.0125$ at a reduced temperature of $T^* = 0.15$ and reduced densities of $\rho^* = 0.025$ and 0.3, representative of the vapour and liquid phases, respectively. The correlation functions are multiplied by the reduced densities in order to bring the results for low and high densities on to the same scale.

Table 7.2: Mean cluster sizes $\bar{n}$ for the DHS fluid and the DYHS fluid with $\varepsilon_{\mathrm{Y}}^{*} = 0.0125$, at a dipolar temperature $T^{*} = 0.15$ and at various reduced densities ρ^{*}. Results are given for different energy cutoffs u_c.

		$\rho^{*} = 0.025$	$\rho^{*} = 0.05$	$\rho^{*} = 0.1$	$\rho^{*} = 0.2$	$\rho^{*} = 0.3$
System	$u_c\sigma^3/\mu^2$	$\bar{n}$	$\bar{n}$	$\bar{n}$	$\bar{n}$	$\bar{n}$
DHS	-1.0	27.20	29.01	29.74	28.89	28.44
DYHS	-1.0	27.02	28.82	29.85	29.53	29.66
DHS	-1.1	19.09	19.20	18.30	15.59	13.40
DYHS	-1.1	18.80	18.73	17.85	15.19	13.29
DHS	-1.2	13.24	13.01	12.17	10.02	8.38
DYHS	-1.2	13.07	12.65	11.73	9.66	8.18
DHS	-1.3	9.06	8.85	8.28	6.88	5.76
DYHS	-1.3	8.97	8.62	7.98	6.62	5.62
DHS	-1.4	6.12	5.99	5.66	4.82	4.12
DYHS	-1.4	6.08	5.86	5.49	4.66	4.03
DHS	-1.5	4.11	4.03	3.85	3.39	2.98
DYHS	-1.5	4.08	3.96	3.76	3.29	2.93

7.4.5 Clustering

The characteristic structural feature of dipolar fluids at low temperatures is the presence of chains and networks. The impact of such clustering on experimentally accessible scattering functions in colloidal ferrofluids is well known [88, 90, 98]. Weis and co-workers have provided in-depth analyses of cluster distributions [69, 119]. Tlusty and Safran have described the structure theoretically in terms of 'end' and 'Y' defects [8]. The most simple measure of clustering is the mean cluster size $\bar{n}$. Again, the comparison made here is between the DHS fluid and the DYHS fluid with $\varepsilon_{\mathrm{Y}}^{*} = 0.0125$, at a fixed temperature of $T^{*} = 0.15$. Table 7.2 shows results for $\bar{n}$ determined in NVT MC simulations of $N = 1024$ particles at various reduced densities in the range $0.025 \leq \rho^{*} \leq 0.3$. Two particles were considered to be bonded if the dipolar interaction energy between them was less than some cutoff u_c. Using this energy criterion, the system of N particles was partitioned in to a set of disjoint clusters, and the mean cluster size $\bar{n}$ was computed. The choice of u_c is somewhat arbitrary, so results for several values of u_c in the range $-1.5\mu^2/\sigma^3 \leq u_c \leq -\mu^2/\sigma^3$ are shown in Table 7.2. The essential point is that, in terms of the mean cluster size, the DHS fluid shows a slightly higher degree of clustering than the DYHS fluid, but only to the extent of a few percent. A reasonable explanation could be that the isotropic Yukawa interaction increases the possibility of excursions from the ideal nose-to-tail parallel conformation of neighbouring dipoles, resulting in dipolar interaction energies that do not satisfy the clustering criterion. In any case, the deviations are tiny.

To shed more light on the cluster structure, coordination-number histograms have been

constructed, this time using a distance cut-off criterion of $r_c = 1.1\sigma$. To simplify the analysis, and to make contact with the defect-based theory of Tlusty and Safran [8], each particle has been placed in to one of three categories: 'free end', which contains particles with either 0 or 1 nearest neighbour within a distance r_c; 'ideal chain', which contain those particles with 2 nearest neighbours and thus belong to chains; and 'branch', which contain those particles with 3 or more nearest neighbours. Histograms have been computed in NVT MC simulations of the DHS fluid, and DYHS fluids with $\varepsilon^*_{\mathrm{Y}} = 0.0125$ and $\varepsilon^*_{\mathrm{Y}} = 0.025$, at a temperature $T^* = 0.15$ and at densities in the range $0.025 \leq \rho^* \leq 0.3$; the results are shown in Fig. 7.10. In all cases, with increasing density the proportions of particles in the 'free end' and 'ideal chain' categories decrease, while the proportion of 'branch' particles increases. This is broadly in line with the defect-based theory of Tlusty and Safran [8]. At all densities, increasing the Yukawa interaction parameter disfavours 'free ends' and 'ideal chains', but favours 'branches'. This is easily explained by the decreasing net anisotropy of the interactions with increasing $\varepsilon^*_{\mathrm{Y}}$.

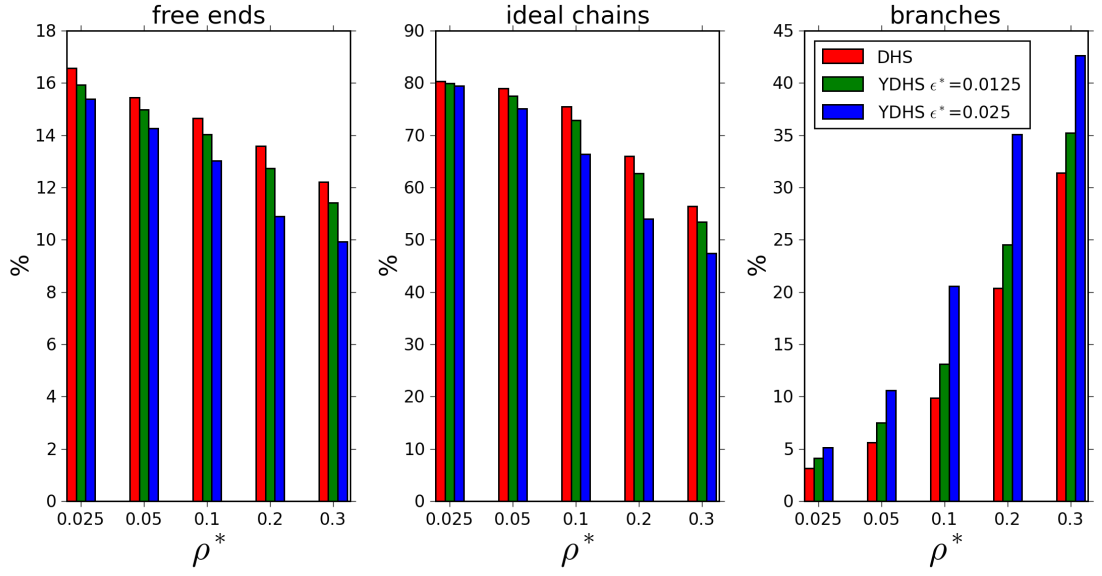

Figure 7.10: Coordination-number histograms for the DHS fluid (red, left-hand bar), and DYHS fluids with $\varepsilon^*_{\mathrm{Y}} = 0.0125$ (green, central bar) and $\varepsilon^*_{\mathrm{Y}} = 0.025$ (blue, right-hand bar), at a temperature $T^* = 0.15$ and at densities in the range $0.025 \leq \rho^* \leq 0.3$. The particles are divided in to three categories: 'free end', which contains particles with either 0 or 1 nearest neighbour; 'ideal chain', which contain those particles with 2 nearest neighbours and thus belong to chains; and 'branch', which contain those particles with 3 or more nearest neighbours.

7.5 Discussion

In this chapter, phase coexistence data from large-scale grand-canonical simulations of dipolar hard spheres (DHSs) interacting with an additional isotropic attractive Yukawa potential, termed dipolar Yukawa hard spheres (DYHSs) are presented. In contrast to prior work a biased particle insertion/deletion Monte Carlo algorithm was employed which has facilitated the study of DYHS model in the vicinity of the limit of vanishing isotropic interactions. Critical parameters are presented for systems with Yukawa interaction strengths down to $\varepsilon_{\mathrm{Y}}^{*} = 0.0125$, meaning a well depth almost two orders of magnitude smaller than the characteristic dipolar interaction parameter μ^2/σ^3. Simulations closer to the DHS limit fail to indicate phase separation but for intermediate and large values of the isotropic interaction parameter, a linear variation of T_c^* with $\varepsilon_{\mathrm{Y}}^{*}$ is observed.

However, in the low-$\varepsilon_{\mathrm{Y}}^{*}$ regime the linear relationship is violated with T_c^* decreasing quickly as $\varepsilon_{\mathrm{Y}}^{*}$ is lowered. These findings suggests that the transition disappears before the DHS limit is reached. To gain insight on the differences between the DYHS fluid and the DHS fluid, the configurational energy, pair correlation functions, and cluster statistics have been examined as functions of temperature along a low-temperature isotherm (below the putative critical temperatures). An analysis of the configurational energy shows that even at the highest density considered, the difference between the DYHS and DHS systems is only of order $0.1k_{\mathrm{B}}T$ per particle. Projections of the molecular pair correlation function on to rotational invariants are qualitatively similar in the two systems, with only small relative variations in the peaks and troughs. The mean cluster sizes within the two systems differ by only a few percent. The coordination-number histograms for both types of fluid are qualitatively similar, showing decreasing proportions of particles with 0/1 and 2 nearest neighbours as the density is increased, while the proportions of particles with 3 or more nearest neighbours increases. Increasing the Yukawa interaction parameter disfavours particles having 0/1 and 2 neighbours, but favours particles having 3 or more neighbours.

Frustratingly, there are no clear differences between DYHS which marginally show phase separation and DHS in the various quantities measured so far. Therefore, the conclusions are necessarily speculative. With this caveat, two alternative scenarios are proposed which will hopefully help focus future studies.

Scenario 1: Phase separation does not exist in the DHS fluid. This is the most obvious conclusion suggested by the simulation results; however, many people have fallen in to this trap before. If this is the correct scenario, then some subtle physics has yet to be uncovered which would explain the apparently different phase behaviour between the

DHS and DYHS systems, and the abrupt disappearance of the phase transition when the isotropic interactions are reduced below a critical level. One possible explanation is as follows. In the theory put forward by Tlusty and Safran, vapour-liquid phase separation is considered a demixing transition between 'end' and 'Y' defects, each type of defect making its own contribution to the total free energy of the fluid [8]. Phase separation is predicted for particular ranges of the energetic costs per defect, with the critical temperature and density being dictated only by the values of these energetic parameters. If the theory is correct then the defect energies in the DYHS fluid must be within the necessary ranges for phase separation to occur. Specifically, the energetic cost of an 'end' defect ε_1 and the energetic cost of a 'Y' defect ε_3 must satisfy the relationship $\varepsilon_1 > 3\varepsilon_3$; see Eq. (3) of reference [8]. It is possible that with the bare dipolar interaction potential, the defect energies are outside of the ranges necessary for phase separation. This would explain the sudden disappearance of the transition as the DHS limit is approached, and is less dramatic than other scenarios such as the existence of a preemptive freezing transition [87], gel formation [120], or a shrinking region of stability of the vapour phase as in some patchy colloids [121].

Scenario 2: Phase separation cannot be observed in finite-size systems accessible at present. If phase separation exists in dipolar fluids, and if the mechanism is of the kind proposed by Tlusty and Safran [8], then perhaps the fundamental problem facing simulations is one of finite size. As the isotropic energy parameter in the DYHS system is reduced, the net anisotropy of the interactions increases, leading to a 'stiffer' network and fewer branching points. Perhaps the simulation cell cuts off structures on longer lengthscales, affecting the free energies of the defects, and particularly the 'Y' defects? This kind of effect might perturb the relevant free energies of 'ends' and 'Ys' to a sufficient extent to preclude phase separation. This is not an easy problem to overcome. It is going to be some time before such accurate calculations can be performed on systems with linear dimensions at least one order of magnitude larger than at present, in order to confirm or deny this scenario. It should be noted, that this scenario is not supported by the finite-size analysis carried out in Section 7.4.2. Naïvely, one would expect an anomalous free energy dependence on the system size to affect e.g., the scaling law Eq. (7.13). However, absolutely no anomalous system-size effects in the analyses of the critical points could be observed. Still, one needs to be cautious as it is not straightforward to foresee how such finite-size effects would couple to the critical temperature dependence.

Chapter 8

Conclusion

Two different topics in computer simulation of phase separation were investigated in this work: (i) Application and development of flat histogram sampling methods and (ii) the phenomenon of phase transition in dipolar fluids.

* * *

In Part I, a unifying framework is devised to derive Monte Carlo sampling schemes based on the Wang-Landau (WL) algorithm which facilitates flat histogram sampling. The framework yields uniform sampling rules for thermodynamic states given either by the mechanically extensive variables (WLEXT scheme) appearing in the Hamiltonian or, equivalently, uniformly sample the thermodynamic fields which are conjugate to these mechanical variables (CFRW scheme). The methods are evaluated in Chapters 3 and 4 by simulating a classical lattice Hubbard model, and vapour-liquid transitions in the Lennard-Jones fluid, charged soft spheres, and Stockmayer fluids with high dipole strengths.

The advantage of the WLEXT scheme is that ensemble averages can be calculated at any thermodynamic state point by simple reweighting. The CFRW scheme on the other hand seems to converge faster but is limited by the chosen discretisation width of the thermodynamic fields to be sampled. The WLEXT scheme asymptotically reaches a level of uncertainty which does not decrease if the simulation is continued. In comparison, the CFRW scheme employs normal Boltzmann MC sampling for each state point with statistical errors inversely proportional to the square-root of the run length.

For both algorithms considered, it is possible to sample multiple variables in a single simulation. However, for the WLEXT scheme we have found that in practice this is only possible for small systems and it is much more efficient to concentrate the sampling

effort on a single variable to be uniformly sampled, and to run multiple simulations. The CFRW scheme appears to suffer not as much from this drawback but, as noted beforehand, produces less information because it is limited to a certain range and discretisation of thermodynamic field variables. On the other hand, there are many cases where only a certain range of e.g. temperatures is of interest so that CFRW allows one to focus on the relevant range whereas normal WL sampling will need to sample all energies the system can attain because it cannot be determined

One particularly effective sampling scheme is given by uniform sampling of particle numbers in the grand-canonical ensemble at fixed temperature. This method is found to work well even when applied to the Stockmayer fluid at high dipole strengths, an example of a complex fluid which is difficult to sample using conventional Monte Carlo algorithms.

* * *

Part II examines the question whether a vapour-liquid phase transition exists in systems of particles with purely dipolar interactions, a topic which has been the subject of a longstanding debate. Monte Carlo simulation results for two different ways of tackling this issue are presented. One approach examines the phase behaviour of fluids of charged hard dumbbells (CHD), each made up of two oppositely charged hard spheres with diameters σ and separation d. In the limit $d/\sigma \to 0$, and with the temperature scaled accordingly, this system corresponds to dipolar hard spheres (DHS) while for larger values of d ionic interactions are dominant. The crossover between ionic and dipolar regimes was examined and a linear variation of the critical temperature T_c^* in dipolar reduced units as a function of d is observed, giving rise to an extrapolated $T_{c,\mathrm{DHS}}^* \simeq 0.15$.

The second approach focuses on the dipolar Yukawa hard sphere (DYHS) fluid, which is given by a dipolar hard sphere and an attractive isotropic interaction ϵ_Y of the Yukawa tail form. In this case, the DHS limit is obtained for $\epsilon_\mathrm{Y} \to 0$. It is found that T_c^* depends linearly on the isotropic interaction strength ϵ_Y over a wide range, coinciding with the results for the CHD model and extrapolating to a similar value of $T_{c,\mathrm{DHS}}^*$. However, with the use of specially adapted biased Monte Carlo techniques which are highly efficient, it is shown that the linear variation of T_c^* is violated for very small values of the Yukawa interaction strength, almost two orders of magnitude smaller than the characteristic dipolar interaction energy. It is found that phase separation is not observable below a critical value of the Yukawa energy parameter, even though in thermodynamic and structural terms, the DYHS and DHS systems are very similar. It is suggested that either some very subtle physics distinguishes the DYHS and DHS systems, or the observation of a phase transition in DHSs is precluded by finite-size effects. At present, there is no

clear indication of how to discriminate between these two scenarios, or of alternative scenarios. Despite several decades of theoretical and simulation work, the question of whether a vapour-liquid phase transition exists in systems of particles with purely dipolar interactions still does not seem to have been settled definitively.

Appendix A

Transformation of probability distributions

The following[1] describes how to transform a probability distribution function (PDF) $f(x)$ for the occurrence of a sample x into an equivalent PDF $g(y)$ for the event $y = y(x)$.

We require the transformation $y = y(x)$ to be unique such that there is an unambiguous mapping between x and y. This necessitates $y(x)$ to be a monotonous function of x since any other behaviour implies the existence of multiple valued correspondences $y = y(x)$. A physical requirement is that the transformation must conserve probability. We therefore have in the monotonic increasing case:

$$\begin{aligned} f(x)\mathrm{d}x &= \mathrm{prob}(x \leq x' \leq x + \mathrm{d}x) \\ g(y)\mathrm{d}y &= \mathrm{prob}(y \leq y' \leq y + \mathrm{d}y) \end{aligned}$$

Physical equality of the differential probabilities yields:

$$\begin{aligned} f(x)\mathrm{d}x &= g(y)\mathrm{d}y \\ g(y) &= \frac{f(x)}{\mathrm{d}y/\mathrm{d}x} \end{aligned}$$

If the transformation is monotonously decreasing, implying $\mathrm{d}y/\mathrm{d}x < 0$, we obtain:

$$g(y) = \frac{f(x)}{-\mathrm{d}y/\mathrm{d}x}$$

[1] This section is essentially derived from the "Computational Science Education Project", http://www.phy.ornl.gov/csep/mc/mc.html with contributions from N. Drakos. Here, only the essential background is stated to lay out the basis for Metropolis importance sampling.

This leads to the final transformation rule, as both PDF's $g(y)$ and $g(x)$ are necessarily positive:

$$g(y) = \frac{f(x)}{|\mathrm{d}y/\mathrm{d}x|}$$

A useful transformation is the special case where $g(y)$ draws samples y according to *cumulative distribution function* (CDF) of $f(x)$. Consider the following manipulation

$$\begin{aligned} y(x) &= F(x) = \int_{-\infty}^{x} f(x')\mathrm{d}x' \\ \frac{\mathrm{d}y(x)}{\mathrm{d}x} &= f(x) \\ &\therefore \\ g(y) &= \frac{f(x)}{|\mathrm{d}y/\mathrm{d}x|} = 1; y \in [0,1] \end{aligned}$$

which allow us to rewrite an integral according to some PDF $f(x)$,

$$\langle a \rangle = \int_{x_0}^{x_1} a(x) f(x) \mathrm{d}x$$

to a simpler integral

$$\langle a \rangle = \int_{0}^{1} a\left[x(y)\right] \mathrm{d}y.$$

In the context of Monte Carlo sample-mean integration with K discrete samples x_i obtained at random and uniformly on the interal $[x_0, x_1]$, we have thus

$$\begin{aligned} \langle a \rangle &= \frac{(x_1 - x_0)}{K} \sum_{i=1}^{K} a(x_i) f(x_i) \\ &= \frac{1}{K} \sum_{i=1}^{K} a\left[x(y_i)\right]. \end{aligned}$$

where the samples $x(y_i)$ are obtained by generating a uniform number $y_i \in [0,1]$ and then inverting the CDF $y(x)$ to find x_i. The above results can now be applied to derive the Monte Carlo importance sampling scheme as applied to integrals of an observable $a(\mathbf{\Gamma})$ according to the Boltzmann distribution $f(\mathbf{\Gamma})$ over phase space coordinates $\mathbf{\Gamma} \in (\mathcal{P}, \mathcal{Q})$:

$$\langle a \rangle = \int_{(\mathcal{P},\mathcal{Q})} a(\mathbf{\Gamma}) f(\mathbf{\Gamma}) \mathrm{d}\mathbf{\Gamma}.$$

Sampling $\mathbf{\Gamma}_i$ according to the inverse CDF of $f(\mathbf{\Gamma})$, phase-space averages therefore become simple arithmetic averages:

$$\langle a \rangle \approx \frac{1}{K} \sum_{i=1}^{K} a\left[\mathbf{\Gamma}_i\right].$$

Bibliography

[1] G. S. Rushbrooke, G. Stell, and J. S. Høye, *Theory of polar liquids. 1. Dipolar hard spheres*, Mol. Phys. **26**, 1199 (1973).

[2] M. S. Wertheim, *Exact solution of the mean spherical model for fluids of hard spheres with permanent electric dipole moments*, J. Chem. Phys. **55**, 4291 (1971).

[3] K. C. Ng, J. P. Valleau, G. M. Torrie, and G. N. Patey, *Liquid-vapor coexistence of dipolar hard-spheres*, Mol. Phys. **38**, 781 (1979).

[4] M. E. van Leeuwen and B. Smit, *What makes a polar liquid a liquid?*, Phys. Rev. Lett. **71**, 3991 (1993).

[5] J.-M. Caillol, *Search of the gas-liquid transition of dipolar hard spheres*, J. Chem. Phys. **98**, 9835 (1993).

[6] R. Rosensweig, *'Negative viscosity' in a magnetic fluid*, Science **271**, 614 (1996).

[7] T. Halsey, *Electrorheological fluids*, Science **258**, 761 (1992).

[8] T. Tlusty and S. A. Safran, *Defect-induced phase separation in dipolar fluids*, Science **290**, 1328 (2000).

[9] J. D. van der Waals, *Over de Continuiteit van den Gas en Vloeistoftoestand* (Leiden, 1873).

[10] L. Onsager, *Crystal Statistics. I. A two-dimensional model with an order-disorder transition*, Phys. Rev. **65**, 117 (1944).

[11] K. G. Wilson, *Renormalization group and critical phenomena. I. Renormalization group and the Kadanoff scaling picture*, Phys. Rev. B **4**, 3174 (1971).

[12] K. G. Wilson and M. E. Fisher, *Critical exponents in 3.99 dimensions*, Phys. Rev. Lett. **28**, 240 (1972).

[13] E. Luijten, M. E. Fisher, and A. Z. Panagiotopoulos, *Universality class of criticality in the restricted primitive model electrolyte*, Phys. Rev. Lett. **88**, 185701 (2002).

[14] Y. Levin, *Criticality in strongly correlated fluids*, J. Phys.: Condens. Matter **14**, 2303 (2002).

[15] A. Aharony and M. E. Fisher, *Critical behavior of magnets with dipolar interactions. I. Renormalization group near four dimensions*, Phys. Rev. B **8**, 3323 (1973).

[16] D. Frenkel and B. Smit, *Understanding Molecular Simulation: From Algorithms to Applications* (Academic Press, San Diego, 2001), 2nd ed.

[17] N. Metropolis and S. Ulam, *The Monte Carlo method*, J. Am. Stat. Assoc. **44**, 335 (1949).

[18] M. P. Allen and D. J. Tildesley, *Computer simulation of liquids* (Clarendon Press, Oxford, 1987).

[19] G. H. Fredrickson, V. Ganesan, and F. Drolet, *Field-theoretic computer simulation methods for polymers and complex fluids*, Macromolecules **35**, 16 (2002).

[20] J.-P. Hansen and I. R. McDonald, *Theory of simple liquids* (Academic Press, London, 1986).

[21] E. Lomba, M. Lombardero, and J. L. F. Abascal, *New aspects in the simulation and behaviour of polar molecular fluids*, Mol. Phys. **68**, 1067 (1989).

[22] G. M. Torrie and J. P. Valleau, *Nonphysical sampling distributions in Monte Carlo free-energy estimation: Umbrella sampling*, J. Comp. Phys. **23**, 187 (1977).

[23] B. Berg and T. Neuhaus, *Multicanonical ensemble: A new approach to simulate first-order phase transitions*, Phys. Rev. Lett. **68**, 9 (1992).

[24] A. M. Ferrenberg and R. H. Swendsen, *Optimised Monte Carlo data analysis*, Phys. Rev. Lett. **63**, 1195 (1989).

[25] F. Wang and D. P. Landau, *Efficient, multiple-range random walk algorithm to calculate the density of states*, Phys. Rev. Lett. **86**, 2050 (2001).

[26] C. Zhou and R. N. Bhatt, *Understanding and improving the Wang-Landau algorithm*, Phys. Rev. E **72**, 025701 (2005).

[27] H. Lee, Y. Okabe, and D. P. Landau, *Convergence and refinement of the Wang-Landau algorithm*, Comput. Phys. Commun. **175**, 36 (2006).

[28] J. Lee, *New Monte Carlo algorithm: Entropic sampling*, Phys. Rev. Lett. **71**, 211 (1993).

[29] D. P. Landau and F. Wang, *Determining the density of states for classical statistical models by a flat-histogram random walk*, Comput. Phys. Commun. **147**, 674 (2002).

[30] M. S. Shell, P. G. Debenedetti, and A. Z. Panagiotopoulos, *Generalization of the Wang-Landau method for off-lattice simulations*, Phys. Rev. E **66**, 056703 (2002).

[31] C. Zhou, T. Schulthess, S. Torbrugge, and D. P. Landau, *Wang-Landau algorithm for continuous models and joint density of states*, Phys. Rev. Lett. **96**, 120201 (2006).

[32] S. Alder and S. Trebst and A. K. Hartmann and M. Troyer, *Dynamics of the Wang-Landau algorithm and complexity of rare events for the three-dimensional bimodal Ising spin glass*, J. Stat. Mech.: Theory and Experiment **2004**, 07008 (2004).

[33] G. Ganzenmüller and P. J. Camp, *Applications of Wang-Landau sampling to determine phase equilibria in complex fluids*, J. Chem. Phys. **127**, 154504 (2007).

[34] D. J. Earl and M. W. Deem, *Parallel tempering: Theory, applications, and new perspectives*, Phys. Chem. Chem. Phys **7**, 3910 (2005).

[35] R. H. Swendsen and J.-S. Wang, *Replica Monte Carlo simulation of spin-glasses*, Phys. Rev. Lett. **57**, 2607 (1986).

[36] C. Geyer, in *Computing Science and Statistics: Proceedings of the 23rd Symposium on the interface* (American Statistical Association, New-York, 1991), p. 156.

[37] A. P. Lyubartsev, A. A. Martsinovski, S. V. Shevkunov, and P. N. Vorontsov-Velyaminov, *New approach to Monte Carlo calculation of the free energy: Method of expanded ensembles*, J. Chem. Phys. **96**, 1776 (1992).

[38] G. Ganzenmüller and G. Pawlowski, *Flat histogram Monte Carlo sampling for mechanical variables and conjugate thermodynamic fields with example applications to strongly correlated electronic systems*, Phys. Rev. E **78**, 036703 (2008).

[39] R. Micnas, S. Robaszkiewicz, and K. A. Chao, *Multicritical behavior of the extended Hubbard model in the zero-bandwidth limit*, Phys. Rev. B **29**, 2784 (1984).

[40] R. Micnas, J. Ranninger, and S. Robaszkiewicz, *Superconductivity in narrow-band systems with local nonretarded attractive interactions*, Rev. Mod. Phys. **62**, 113 (1990).

[41] R. A. Bari, *Effects of short-range interactions on electron-charge ordering and lattice distortions in the localized state*, Phys. Rev. B **3**, 2662 (1971).

[42] T. Misawa, Y. Yamaji, and M. Imada, *Tricritical behavior in charge-order system*, J. Phys. Soc. Jpn. **75**, 064705 (2006).

[43] A. Avella and F. Mancini, *Exact solution of the one-dimensional spin-3/2 Ising model in magnetic field*, Eur. Phys. J. B **50**, 527 (2006).

[44] G. Pawłowski, *Charge orderings in the atomic limit of the extended Hubbard model*, Eur. Phys. J. B **53**, 471 (2006).

[45] I. D. Lawrie and S. Sarbach, in C. Domb and J. L. Lebowitz, eds., *Phase Transitions and critical phenomena* (Academic Press, London, 1984), vol. 9.

[46] N. B. Wilding and P. Nielaba, *Tricritical universality in a two-dimensional spin fluid*, Phys. Rev. E **53**, 926 (1996).

[47] K. Binder, *Finite size scaling analysis of ising model block distribution functions*, Z. Phys. B. **43**, 119 (1981).

[48] Y. Deng and H. W. J. Blöte, *Constrained tricritical Blume-Capel model in three dimensions*, Phys. Rev. E **70**, 046111 (2004).

[49] D. P. Landau and K. Binder, *A guide to Monte Carlo simulations in statistical physics* (Cambridge University Press, Cambridge, 2000).

[50] D. P. Landau and R. H. Swendsen, *Tricritical universality in two dimensions*, Phys. Rev. Lett. **46**, 1437 (1981).

[51] D. P. Landau, S.-H. Tsai, and M. Exler, *A new approach to Monte Carlo simulations in statistical physics: Wang-Landau sampling*, Am. J. Phys. **72**, 1294 (2004).

[52] I. D. Gospodinov and F. A. Escobedo, *Multicanonical schemes for mapping out free-energy landscapes of single-component and multicomponent systems*, J. Chem. Phys. **122**, 164103 (2005).

[53] A. Z. Panagiotopoulos, *Monte Carlo methods for phase equilibria of fluids*, J. Phys.: Condens. Matter **12**, R25 (2000).

[54] J. R. Errington, *Direct calculation of liquid-vapor phase equilibria from transition matrix Monte Carlo simulation*, J. Chem. Phys. **118**, 9915 (2003).

[55] J. R. Errington, *Benchmark results for Lennard-Jones fluid. 3. SAT-TMMC: Liquid-vapor coexistence properties* (2003), `http://www.cstl.nist.gov/srs/LJ_PURE/sattmmc.htm`.

[56] A. M. Ferrenberg and D. P. Landau, *Critical behavior of the three-dimensional Ising model: A high-resolution Monte Carlo study*, Phys. Rev. B **44**, 5081 (1991).

[57] J. M. Caillol, *A Monte Carlo study of the dielectric constant of the restricted primitive model of electrolytes on the vapour branch of the coexistence line*, J. Chem. Phys. **102**, 5471 (1995).

[58] J. C. Shelley and G. N. Patey, *A comparison of liquid-vapour coexistence in charged hard sphere and charged hard dumbbell fluids*, J. Chem. Phys. **103**, 8299 (1995).

[59] J.-M. Caillol, D. Levesque, and J.-J. Weis, *Critical behavior of the restricted primitive model revisited*, J. Chem. Phys. **116**, 10794 (2002).

[60] G. Orkoulas and A. Z. Panagiotopoulos, *Free energy and phase equilibria for the restricted primitive model of ionic fluids from Monte Carlo simulations*, J. Chem. Phys. **101**, 1452 (1994).

[61] J. Anwar, D. Frenkel, and M. G. Noro, *Calculation of the melting point of NaCl by molecular simulation*, J. Chem. Phys. **118**, 728 (2003).

[62] P. I. C. Teixeira, J. M. Tavares, and M. M. Telo da Gama, *The effect of dipolar forces on the structure and thermodynamics of classical fluids*, J. Phys.: Condens. Matter **12**, R411 (2000).

[63] C. Holm and J.-J. Weis, *The structure of ferrofluids: A status report*, Curr. Opin. Colloid Interface Sci. **10**, 133 (2005).

[64] P. G. de Gennes and P. A. Pincus, *Pair correlations in a ferromagnetic colloid*, Phys. Kondens. Materie **11**, 189 (1970).

[65] P. J. Camp, J. C. Shelley, and G. N. Patey, *Isotropic fluid phases of dipolar hard spheres*, Phys. Rev. Lett. **84**, 115 (2000).

[66] G. Ganzenmüller and P. J. Camp, *Vapor-liquid coexistence in fluids of charged hard dumbbells*, J. Chem. Phys. **126**, 191104 (2007).

[67] M. J. Stevens and G. S. Grest, *Coexistence in dipolar fluids in a field*, Phys. Rev. Lett. **72**, 3686 (1994).

[68] M. J. Stevens and G. S. Grest, *"phase coexistence of a stockmayer fluid in an applied field"*, Phys. Rev. E **51**, 5976 (1995).

[69] J. J. Weis and D. Levesque, *Chain formation in low density dipolar hard spheres: a Monte Carlo study*, Phys. Rev. Lett. **71**, 2729 (1993).

[70] A. Z. Panagiotopoulos, *Direct determination of phase coexistence properties of fluids by Monte Carlo simulation in a new ensemble* , Mol. Phys. **61**, 813 (1987).

[71] B. Smit and D. Frenkel, *Calculation of the chemical potential in the Gibbs ensemble*, Mol. Phys. **68**, 951 (1989).

[72] M. E. van Leeuwen, B. Smit, and E. M. Hendriks, *Vapour-liquid equilibria of Stockmayer fluids. Computer simulations and perturbation theory*, Mol. Phys. **78**, 271 (1993).

[73] M. E. van Leeuwen, *Deviation from corresponding-states behaviour for polar fluids*, Mol. Phys. **82**, 383 (1994).

[74] J. Bartke and R. Hentschke, *Phase behavior of the Stockmayer fluid via molecular dynamics simulation*, Phys. Rev. E **75**, 061503 (2007).

[75] E. de Miguel, *System-size effects at the isotropic-nematic transition from computer simulation*, Phys. Rev. E **47**, 3334 (1993).

[76] E. de Miguel, *Reexamining the phase diagram of the Gay-Berne fluid*, Mol. Phys. **100**, 2449 (2002).

[77] E. de Miguel and C. Vega, *The global phase diagram of the Gay-Berne model*, J. Chem. Phys. **117**, 6313 (2002).

[78] P. J. Camp, C. P. Mason, M. P. Allen, A. A. Khare, and D. A. Kofke, *The isotropic-nematic phase transition in uniaxial hard ellipsoid fluids: Coexistence data and the approach to the Onsager limit*, J. Chem. Phys. **105**, 2837 (1996).

[79] M. S. Shell, P. G. Debenedetti, and A. Z. Panagiotopoulos, *An improved Monte Carlo method for direct calculation of the density of states*, J. Chem. Phys. **119**, 94061 (2003).

[80] B. Huke and M. Lücke, *Magnetic properties of colloidal suspensions of interacting magnetic particles*, Rep. Prog. Phys. **67**, 1731 (2004).

[81] H. Mamiya, I. Nakatani, and T. Furubayashi, *Phase transitions of Iron-Nitride magnetic fluids*, Phys. Rev. Lett. **84**, 6106 (2000).

[82] D. P. Shelton, *Are dipolar liquids ferroelectric?*, J. Chem. Phys. **123**, 084502 (2005).

[83] D. Wei and G. N. Patey, *Orientational order in simple dipolar liquids: Computer simulation of a ferroelectric nematic phase*, Phys. Rev. Lett. **68**, 2043 (1992).

[84] J. J. Weis and D. Levesque, *Ferroelectric phases of dipolar hard spheres*, Phys. Rev. E **48**, 3728 (1993).

[85] J.-J. Weis and D. Levesque, *Simple dipolar fluids as generic models for soft matter*, Adv. Polym. Sci. **185**, 163 (2005).

[86] M. A. Pounds and P. A. Madden, *"are dipolar liquids ferroelectric? simulation studies"*, J. Chem. Phys. **126**, 104506 (2007).

[87] M. H. J. Hagen and D. Frenkel, *Determination of phase diagrams for the hard-core attractive Yukawa system*, J. Chem. Phys. **101**, 4093 (1994).

[88] P. J. Camp and G. N. Patey, *Structure and scattering in colloidal ferrofluids*, Phys. Rev. E **62**, 5403 (2000).

[89] M. J. Stevens and G. S. Grest, *Structure of soft-sphere dipolar fluids*, Phys. Rev. E **51**, 5962 (1995).

[90] D. Levesque and J. J. Weis, *Orientational and structural order in strongly interacting dipolar hard spheres*, Phys. Rev. E **49**, 5131 (1994).

[91] S. C. McGrother, D. C. Williamson, and G. Jackson, *A re-examination of the phase diagram of hard spherocylinders*, J. Chem. Phys. **104**, 6755 (1996).

[92] I. Szalai, D. Henderson, D. Boda, and K.-Y. Chan, *Thermodynamics and structural properties of the dipolar Yukawa fluid*, J. Chem. Phys. **111**, 337 (1999).

[93] R. P. Sear, *Low-density fluid phase of dipolar hard spheres*, Phys. Rev. Lett. **76**, 2310 (1996).

[94] R. van Roij, *Theory of chain association versus liquid condensation*, Phys. Rev. Lett. **76**, 3348 (1996).

[95] J. M. Tavares, M. M. Telo da Gama, and M. A. Osipov, *Criticality of dipolar fluids: liquid-vapour condensation versus phase separation in systems of living polymers*, Phys. Rev. E **56**, R6252 (1997).

[96] Y. Levin, *What happened to the gas-liquid transition in the system of dipolar hard spheres?*, Phys. Rev. Lett. **83**, 1159 (1999).

[97] R. Hentschke, J. Bartke, and F. Pesth, *Equilibrium polymerization and gas-liquid critical behavior in the Stockmayer fluid*, Phys. Rev. E **75**, 011506 (2007).

[98] A. O. Ivanov, S. S. Kantorovich, and P. J. Camp, *Comment on "Equilibrium polymerization and gas-liquid critical behaviour in the Stockmayer fluid"*, Phys. Rev. E **77**, 013501 (2008).

[99] J. C. Shelley, G. N. Patey, D. Levesque, and J. J. Weis, *Liquid-vapor coexistence in fluids of dipolar hard dumbbells and spherocylinders*, Phys. Rev. E **59**, 3065 (1999).

[100] N. G. Almarza, E. Lomba, C. Martín, and A. Gallardo, *Demixing in binary mixtures of apolar and dipolar hard spheres*, J. Chem. Phys. **129**, 234504 (2008).

[101] J. M. Romero-Enrique, L. F. Rull, and A. Z. Panagiotopoulos, *Dipolar origin of the gas-liquid coexistence of the hard-core 1:1 electrolyte model*, Phys. Rev. E **66**, 041204 (2002).

[102] C. D. Daub, G. N. Patey, and P. J. Camp, *Liquid-vapor criticality in a fluid of charged hard dumbbells*, J. Chem. Phys. **119**, 7952 (2003).

[103] J.-M. Caillol and J.-J. Weis, *Free energy and cluster structure in the coexistence region of the restricted primitive model*, J. Chem. Phys. **102**, 7610 (1995).

[104] S. C. McGrother and G. Jackson, *Island of vapor-liquid coexistence in dipolar hard-core systems*, Phys. Rev. Lett. **76**, 4183 (1996).

[105] M. A. Miller, R. Blaak, C. N. Lumb, and J.-P. Hansen, *Dynamical arrest in low density dipolar colloidal gels*, J. Chem. Phys. **130**, 114507 (2009).

[106] G. Ganzenmüller, G. N. Patey, and P. J. Camp, Molec. Phys. pp. in press, accepted manuscript (2009).

[107] Yu. V. Kalyuzhnyi, I. A. Protsykevytch, G. Ganzenmüller, and P. J. Camp, *Liquid-vapour coexistence in the dipolar Yukawa hard-sphere fluid*, Europhys. Lett. **84**, 26001 (2008).

[108] M.N. Rosenbluth and A.W. Rosenbluth, *Monte Carlo simulations of the average extension of molecular chains*, J. Chem. Phys **23**, 356 (1955).

[109] R. H. Swendsen and J. S. Wang, *"nonuniversal critical dynamics in monte carlo simulations"*, Phys. Rev. Lett. **58**, 86 (1987).

[110] D. Frenkel, in M. P. Allen and D. J. Tildesley, eds., *Computer Simulation in chemical physics* (Kluwer Academic, Dordrecht, 1992), vol. NATO ASI Series C Vol. 397, p. 93.

[111] J. C. Shelley and G. N. Patey, *A configuration bias Monte Carlo method for water*, J. Chem. Phys. **102**, 7656 (1995).

[112] R. Guida and J. Zinn-Justin, *Critical exponents of the n-vector model*, J. Phys. A: Math. Gen. **31**, 8103 (1998).

[113] Y. C. Kim, M. E. Fisher, and E. Luijten, *Precise simulation of near-critical fluid coexistence*, Phys. Rev. Lett. **91**, 065701 (2003).

[114] D. Pini, G. Stell, and N. B. Wilding, *A liquid-state theory that remains successful in the critical region*, Mol. Phys. **95**, 483 (1998).

[115] A. D. Bruce and N. B. Wilding, *Computational strategies for mapping equilibrium phase diagrams*, Adv. Chem. Phys. **127**, 1 (2003).

[116] M. M. Tsypin and H. W. J. Blöte, *Probability distribution of the order parameter for the three-dimensional Ising-model universality class: A high-precision Monte Carlo study*, Phys. Rev. E **62**, 73 (2000).

[117] P. J. Camp and G. N. Patey, *Coexistence and criticality of fluids with long-range potentials*, J. Chem. Phys. **114**, 399 (2001).

[118] A. M. Ferrenberg and R. H. Swendsen, *New Monte Carlo technique for studying phase transitions*, Phys. Rev. Lett. **61**, 2635 (1988).

[119] J. M. Tavares, J. J. Weis, and M. M. Telo da Gama, *Strongly dipolar fluids at low densities compared to living polymers*, Phys. Rev. E **59**, 4388 (1999).

[120] R. Blaak, M. Miller, and J.-P. Hansen, *Reversible gelation and dynamical arrest of dipolar colloids*, Europhys. Lett. **78**, 26002 (2007).

[121] E. Bianchi, J. Largo, P. Tartaglia, E. Zaccarelli, and F. Sciortino, *Phase diagram of patchy colloids: Towards empty liquids*, Phys. Rev. Lett. **97**, 168301 (2006).